

Optimum Material Distributions for Minimizing Stresses in a Rotating Functionally Graded Material Circular Disk

by

Sazedur Rahman

Submitted in partial fulfillment of the requirements for the degree of
MASTER OF SCIENCE IN MECHANICAL ENGINEERING



Department of Mechanical Engineering

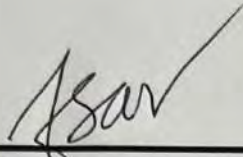
BANGLADESH UNIVERSITY OF ENGINEERING AND TECHNOLOGY

Dhaka 1000, Bangladesh.

July 2022

The thesis titled “**Optimum Material Distributions for Minimizing Stresses in a Rotating Functionally Graded Material Circular Disk**” submitted by **Sazedur Rahman**, Student No.: **1018102001**, Session: **October 2018**, has been accepted as satisfactory in partial fulfillment of the requirement for the degree of **Master of Science in Mechanical Engineering** on **25 July 2022**.

BOARD OF EXAMINERS



Dr. Md. Afsar Ali

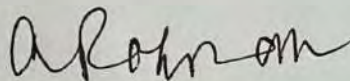
Chairman

Professor

Department of Mechanical Engineering

Bangladesh University of Engineering and Technology

Dhaka-1000, Bangladesh



Dr. Muhammad Ashiqur Rahman

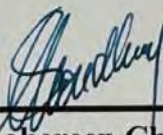
Member
(Ex- officio)

Professor and Head

Department of Mechanical Engineering

Bangladesh University of Engineering and Technology

Dhaka-1000, Bangladesh



Dr. Shahereen Chowdhury

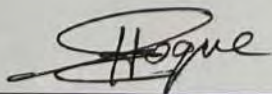
Member

Assistant Professor

Department of Mechanical Engineering

Bangladesh University of Engineering and Technology

Dhaka-1000, Bangladesh



Dr. Md. Enamul Hoque

Member
(External)

Professor

Department of Biomedical Engineering

Military Institute of Science and Technology

Dhaka-1216, Bangladesh

CANDIDATE'S DECLARATION

It is hereby declared that this thesis or any part of it has not been submitted elsewhere for the award of any degree or diploma.



Sazedur Rahman

Dedicated to my beloved parents and family.

Dedicated to my beloved parents and family

Table of Contents	Page No.
List of Figures	vii
List of Tables.....	xiii
List of Symbols	xiv
Acknowledgements	xv
Abstract	xvi
CHAPTER ONE: INTRODUCTION.....	1
1.1 Background	1
1.2 Fabrication Processes of FGMs.....	6
1.3 Statement of the Problem	10
1.4 Objectives	12
1.5 Motivation of the Present Work	13
CHAPTER TWO: LITERATURE REVIEW	16
2.1 Different FGM Bodies.....	16
2.2 FGM Disks	17
2.3 Optimization Models for FGM.....	19
CHAPTER THREE: THEORY	22
3.1 Effective Properties of FGM	22
3.2 Discretization Scheme	24
3.3 Temperature Distribution of the FGM Disk.....	25
3.4 Thermoelastic Formulation	27
CHAPTER FOUR: NUMERICAL FORMULATION	31
4.1 Finite Element Formulation.....	31

4.1.1	Variational Methods.....	31
4.1.2	Ritz Method.....	33
4.1.3	Finite Element Formulation of the Present Work	34
4.2	Optimization Model	40
4.2.1	Inverse Method.....	40
4.2.1.1	Differential Evolution.....	41
4.2.1.2	Optimization Model for Minimum Stress.....	43
4.2.1.3	Optimization Model for Prescribed Stress.....	43
4.2.2	Direct Method	48
CHAPTER FIVE: RESULTS AND DISCUSSION.....		50
5.1	Validation of the Finite Element Model.....	52
5.1.1	Comparison with Timoshenko and Goodier	52
5.1.2	Comparison with Sadd	53
5.1.3	Comparison with Madan <i>et al.</i>	54
5.2	Validation of the Optimization Model	56
5.3	Evaluation of Optimum Material Distribution Corresponding to Minimum Stress	61
5.3.1	Boundary Condition: Case I.....	61
5.3.2	Boundary Condition: Case II	75
5.4	Evaluation of Optimum Material Distribution Corresponding to Prescribed Stress	92
5.4.1	Boundary Condition: Case I.....	92
5.4.2	Boundary Condition: Case II	101
CHAPTER SIX: CONCLUSIONS AND RECOMMENDATIONS ...		111
6.1	Conclusions	111
6.2	Recommendations	112
REFERENCES.....		113

List of Figures

Fig. No	Title	Page No.
Fig. 1.1:	Schematic illustration of (a) functionally graded composite and (b) typical laminated composite [9]. -----	2
Fig. 1.2:	(a) Continuous and (b) Stepwise distribution [21]. -----	3
Fig. 1.3:	Variety of applications of Functionally Graded Materials [24]. -----	4
Fig. 1.4:	(a) Schematic depiction of graded microstructure and (b) porosity gradient FGM [25]. -----	5
Fig. 1.5:	FGMs fabrication techniques [28]. -----	6
Fig. 1.6:	Schematic illustration of Thermal Spray Method. -----	7
Fig. 1.7:	Schematic diagram of fabricating FGM by LMD [33]. -----	8
Fig. 1.8:	Steps involved in powder metallurgy to produce FGM. -----	9
Fig. 1.9:	Analytical model of the FGM disk. -----	10
Fig. 3.1:	Discretization of the FGM Disk.-----	24
Fig. 4.1:	Boundary values for an area where a differential equation is valid.-----	31
Fig. 4.2:	Representation of a domain.-----	32
Fig. 4.3:	Flow diagram of initialization, mutation, recombination and selection steps of the differential evolution algorithm. -----	42
Fig. 4.4:	Flow diagram of the Differential Evolution algorithm. -----	42
Fig. 4.5:	Flowchart for optimization model to realize the minimum stress throughout the FGM disk.-----	46
Fig. 4.6:	Flowchart for optimization model to realize the prescribed stress profile across the FGM disk.-----	48
Fig. 4.7:	Flowchart for direct problem to determine von Mises, radial and circumferential stresses, and radial displacement throughout the FGM disk. -----	49
Fig. 5.1:	Comparison of (a) radial stress and (b) circumferential stress with Timoshenko and Goodier [69] in a homogeneous circular disk under rotation only.-----	53
Fig. 5.2:	Comparison of radial and circumferential stress with Sadd [70] in a homogeneous circular plate under thermal load only. -----	54

Fig. 5.3:	Comparison of radial, circumferential, and von Mises stresses in a rotating FGM circular disk corresponding to (a) $b/a = 10$ and (b) $b/a = 5$ with Madan <i>et al.</i> [71].	-55
Fig. 5.4:	Comparison of material distribution in a rotating FGM circular disk corresponding to $b/a = 5$ with Madan <i>et al.</i> [71].	57
Fig. 5.5:	Comparison of von Mises stress in a rotating FGM circular disk corresponding to $b/a = 5$ with Madan <i>et al.</i> [71].	57
Fig. 5.6:	The influence of element size on the parameter F .	60
Fig. 5.7:	Effect of outer surface temperature on optimum material distribution of an FGM disk under Boundary Condition I.	61
Fig. 5.8:	Effect of outer surface temperature on the minimum von Mises stress corresponding to optimum material distribution of an FGM disk under Boundary Condition I.	62
Fig. 5.9:	Effect of outer surface temperature on the radial stress corresponding to minimum von Mises stress and optimum material distribution of an FGM disk under Boundary Condition I.	63
Fig. 5.10:	Effect of outer surface temperature on the circumferential stress corresponding to minimum von Mises stress and optimum material distribution of an FGM disk under Boundary Condition I.	63
Fig. 5.11:	Effect of inner surface temperature on optimum material distribution of an FGM disk under Boundary Condition I.	65
Fig. 5.12:	Effect of 0°C inner surface temperature on the minimum von Mises stress corresponding to optimum material distribution of an FGM disk under Boundary Condition I.	66
Fig. 5.13:	Effect of inner surface temperature on the minimum von Mises stress corresponding to optimum material distribution of an FGM disk under Boundary Condition I.	67
Fig. 5.14:	Effect of inner surface temperature on the radial stress corresponding to minimum von Mises stress and optimum material distribution of an FGM disk under Boundary Condition I.	67
Fig. 5.15:	Effect of inner surface temperature on the circumferential stress corresponding to minimum von Mises stress and optimum material distribution of an FGM disk under Boundary Condition I.	68
Fig. 5.16:	Effect of angular speed on optimum material distribution of an FGM disk under Boundary Condition I.	69

Fig. 5.17: Effect of angular speed on the minimum von Mises stress corresponding to optimum material distribution of an FGM disk under Boundary Condition I. -----70

Fig. 5.18: Effect of angular speed on the radial stress corresponding to minimum von Mises stress and optimum material distribution of an FGM disk under Boundary Condition I. -----71

Fig. 5.19: Effect of angular speed on the circumferential stress corresponding to minimum von Mises stress and optimum material distribution of an FGM disk under Boundary Condition I. -----71

Fig. 5.20: Effect of aspect ratio of disk on optimum material distribution of an FGM disk under Boundary Condition I. -----72

Fig. 5.21: Effect of aspect ratio on the minimum von Mises stress corresponding to optimum material distribution of an FGM disk under Boundary Condition I. -----73

Fig. 5.22: Effect of aspect ratio on the radial stress corresponding to minimum von Mises stress and optimum material distribution of an FGM disk under Boundary Condition I. -----74

Fig. 5.23: Effect of aspect ratio on the circumferential stress corresponding to minimum von Mises stress and optimum material distribution of an FGM disk under Boundary Condition I. -----74

Fig. 5.24: Effect of outer surface temperature on optimum material distribution of an FGM disk under Boundary Condition II. -----75

Fig. 5.25: Effect of outer surface temperature on the minimum von Mises stress corresponding to optimum material distribution of an FGM disk under Boundary Condition II. ----76

Fig. 5.26: Effect of outer surface temperature on the radial stress corresponding to minimum von Mises stress and optimum material distribution of an FGM disk under Boundary Condition II. -----77

Fig. 5.27: Effect of outer surface temperature on the circumferential stress corresponding to minimum von Mises stress and optimum material distribution of an FGM disk under Boundary Condition II.-----77

Fig. 5.28: Effect of outer surface temperature on the radial displacement corresponding to minimum von Mises stress and optimum material distribution of an FGM disk under Boundary Condition II.-----78

Fig. 5.29: Effect of inner surface temperature on optimum material distribution of an FGM disk under Boundary Condition II. -----79

Fig. 5.30: Effect of 0°C inner surface temperature on the minimum von Mises stress corresponding to optimum material distribution of an FGM disk under Boundary Condition II. -----80

Fig. 5.31: Effect of inner surface temperature on the minimum von Mises stress corresponding to optimum material distribution of an FGM disk under Boundary Condition II.----81

Fig. 5.32: Effect of inner surface temperature on the radial stress corresponding to minimum von Mises stress and optimum material distribution of an FGM disk under Boundary Condition II. -----81

Fig. 5.33: Effect of inner surface temperature on the circumferential stress corresponding to minimum von Mises stress and optimum material distribution of an FGM disk under Boundary Condition II.-----82

Fig. 5.34: Effect of inner surface temperature on the radial displacement corresponding to minimum von Mises stress and optimum material distribution of an FGM disk under Boundary Condition II.-----83

Fig. 5.35: Effect of angular speed on optimum material distribution of an FGM disk under Boundary Condition II.-----84

Fig. 5.36: Effect of angular speed on the minimum von Mises stress corresponding to optimum material distribution of an FGM disk under Boundary Condition II. -----85

Fig. 5.37: Effect of angular speed on the radial stress corresponding to minimum von Mises stress and optimum material distribution of an FGM disk under Boundary Condition II. -----86

Fig. 5.38: Effect of angular speed on the circumferential stress corresponding to minimum von Mises stress and optimum material distribution of an FGM disk under Boundary Condition II. -----86

Fig. 5.39: Effect of angular speed on the radial displacement corresponding to minimum von Mises stress and optimum material distribution of an FGM disk under Boundary Condition II. -----87

Fig. 5.40: Effect of aspect ratio on optimum material distribution of an FGM disk under Boundary Condition II.-----88

Fig. 5.41: Effect of aspect ratio on the minimum von Mises stress corresponding to optimum material distribution of an FGM disk under Boundary Condition II. -----89

Fig. 5.42: Effect of aspect ratio on the radial stress corresponding to minimum von Mises stress and optimum material distribution of an FGM disk under Boundary Condition II. -----90

Fig. 5.43: Effect of aspect ratio on the circumferential stress corresponding to minimum von Mises stress and optimum material distribution of an FGM disk under Boundary Condition II. -----90

Fig. 5.44: Effect of aspect ratio on the radial displacement corresponding to minimum von Mises stress and optimum material distribution of an FGM disk under Boundary Condition II. -----91

Fig. 5.45: Prescribed stress profile with a decreasing nature in an FGM disk corresponds to $b/a = 2.5$ under Boundary Condition I. -----93

Fig. 5.46: Optimum material distribution in an FGM disk corresponding to the prescribed stress field of **Fig. 5.45**. -----93

Fig. 5.47: Prescribed stress profile with an increasing nature in an FGM disk corresponds to $b/a = 2.5$ under Boundary Condition I. -----94

Fig. 5.48: Optimum material distribution in an FGM disk corresponding to the prescribed stress field of **Fig. 5.47**. -----95

Fig. 5.49: Prescribed stress profile (Constant) in an FGM disk corresponds to $b/a = 2.5$ under Boundary Condition I.-----96

Fig. 5.50: Optimum material distribution in an FGM disk corresponding to the prescribed stress field of **Fig. 5.49**. -----96

Fig. 5.51: Prescribed stress profile with a decreasing nature in an FGM disk corresponds to $b/a = 5$ under Boundary Condition I. -----97

Fig. 5.52: Optimum material distribution in an FGM disk corresponding to the prescribed stress field of **Fig. 5.51**. -----98

Fig. 5.53: Prescribed stress profile with an increasing nature in an FGM disk corresponds to $b/a = 5$ under Boundary Condition I.-----99

Fig. 5.54: Optimum material distribution in an FGM disk corresponding to the prescribed stress field of **Fig. 5.53**. -----99

Fig. 5.55: Prescribed stress profile (Constant) in an FGM disk corresponds to $b/a = 5$ under Boundary Condition I.----- 100

Fig. 5.56: Optimum material distribution in an FGM disk corresponding to the prescribed stress field of **Fig. 5.55**. ----- 101

Fig. 5.57: Prescribed stress profile with a decreasing nature in an FGM disk corresponds to $b/a = 2.5$ under Boundary Condition II. ----- 102

Fig. 5.58: Optimum material distribution in an FGM disk corresponding to the prescribed stress field of **Fig. 5.57**. ----- 103

Fig. 5.59: Prescribed stress profile with an increasing nature in an FGM disk corresponds to $b/a = 2.5$ under Boundary Condition II. ----- 104

Fig. 5.60: Optimum material distribution in an FGM disk corresponding to the prescribed stress field of **Fig. 5.59**. ----- 104

Fig. 5.61: Prescribed stress profile (Constant) in an FGM disk corresponds to $b/a = 2.5$ under Boundary Condition II.----- 105

Fig. 5.62: Optimum material distribution in an FGM disk corresponding to the prescribed stress field of **Fig. 5.61**. ----- 106

Fig. 5.63: Prescribed stress profile with a decreasing nature in an FGM disk corresponds to $b/a = 5$ under Boundary Condition II. ----- 107

Fig. 5.64: Optimum material distribution in an FGM disk corresponding to the prescribed stress field of **Fig. 5.63**. ----- 107

Fig. 5.65: Prescribed stress profile with an increasing nature in an FGM disk corresponds to $b/a = 5$ under Boundary Condition II.----- 108

Fig. 5.66: Optimum material distribution in an FGM disk corresponding to the prescribed stress field of **Fig. 5.65**. ----- 109

Fig. 5.67: Prescribed stress profile (Constant) in an FGM disk corresponds to $b/a = 5$ under Boundary Condition II.----- 110

Fig. 5.68: Optimum material distribution in an FGM disk corresponding to the prescribed stress field of **Fig. 5.67**. ----- 110

List of Tables

Table No.	Title	Page No.
Table 1.1:	Types of material constituents involved in the fabrication of FGM -----	3
Table 5.1:	Mechanical and thermal properties of Al and Al ₂ O ₃ -----	50

List of Symbols

A, B	Constituent materials of FGM
V_A	Volume fraction of constituent A
a	Inner radius of the FGM disk
b	Outer radius of the FGM disk
ω	Angular speed of the FGM disk
N	Revolutions per minute
ν	Poisson's ratio
G	Shear modulus
K	Bulk modulus
E	Young's modulus
α	Coefficient of thermal expansion
ρ	Density
k	Thermal conductivity
T	Temperature distribution
T_1	Temperature at the inner surface of the FGM disk
T_2	Temperature at the outer surface of the FGM disk
e_r	Radial component of elastic strain
e_θ	Circumferential component of elastic strain
ε_r	Radial component of total strain
ε_θ	Circumferential component of total strain
ε^*	Thermal eigenstrain
u_r	Radial displacement
$\tau_{r\theta}$	Shear stress
σ_r	Radial stress
σ_θ	Circumferential stress
σ_{von}	von Mises stress
σ^p	Prescribed stress
c_j	Unknown parameter
Ω	Domain
$\partial\Omega$	Boundary
φ_i, φ_j	Approximate or shape functions
w	Trial function
$f_{obj}(V_A^i)$	Objective function
ϵ	Prescribed small quantity for objective function
n	Number of nodes or variables
m	Number of populations for Differential Evolution

Acknowledgements

First of all, I would like to express my gratitude to the Almighty Allah, the Most Merciful and the most Beneficent, for providing me with the caliber and ability to successfully complete this thesis work. All praise be to the Almighty Allah.

The author would like to extend his most sincere gratitude and thanks to his supervisor, Dr. Md. Afsar Ali, Professor of Mechanical Engineering Department at Bangladesh University of Engineering and Technology (BUET), Dhaka, for his thoughtful and kind supervision, consistent guidance, encouragement, unflagging support, and patience throughout this research work. Without his correct direction, it would have been almost impossible to complete this research. The author will remain grateful to his esteemed supervisor for the invaluable instructions and supports that he has provided.

The author would also like to take this opportunity to offer his sincere appreciation to his beloved parents, wife, and siblings for their cooperation and moral support during the research. It was not very easy to continue the research during the tough period of the COVID-19 pandemic when the whole globe was trying to conquer it. The author was able to complete the research work successfully because of the endless encouragement and assistance that he received from his highly respected supervisor and his parents.

Abstract

Functionally graded materials (FGMs) are an advanced type of composite material having varying material distribution from one to another surface, for which these FGMs become nonhomogeneous in the case of both material characteristics and microstructures. The present study considers a thin circular rotating disk of functionally graded material with a concentric circular hole. The disk is subjected to a thermal load and an inertial force due to the rotation of the disk. The analysis is carried out under plane stress condition. Material properties of the FGM disk are assumed to vary along the radial direction only. In this study, an optimization model is developed for evaluating optimum material distributions in a rotating FGM circular disk corresponding to minimum/prescribed stresses. Further, a mathematical model of direct problem is also developed to calculate stresses and displacements induced in the FGM disk corresponding to a prescribed material distribution. Based on two-dimensional thermoelasticity theories, the problem is formulated in terms of a second-order differential equation. Since a close-form solution of the differential equation is not possible, a standard finite element approach is adopted for the solution of the optimization and direct problems. The models developed in the present study are validated by comparing the results with those available in literature. To demonstrate the developed models, numerical results are obtained for an FGM disk consisting of Al and Al_2O_3 . From the numerical results of direct problem, it is found that the stresses are greatly influenced by material distribution. The results of optimization model ensure that an FGM disk can be designed with optimum material distribution realizing the minimum/prescribed stress profile in the disk. It is also revealed that the stress profile, temperature field, angular speed, and radial thickness of the disk all have significant effects on optimum material distribution of the FGM disk.

CHAPTER 1

INTRODUCTION

1.1 Background

The daily advancement of materials improves material qualities, limiting the usage of accessible materials such as pure metals, alloys, and traditional composites, which cannot be regulated to reach the required properties for many applications [1,2]. Due to the limitations of using standard homogeneous materials such as pure metals, ceramics, alloys, and conventional composites, it was required to design new materials with opposing properties and a graded structure to fulfill the demands of industrial development applications [3 – 7]. Functionally graded materials (FGMs) exhibit multi-functional features due to progressive changes in their composition or structure, making them ideal for engineering applications needing contradictory properties in a single component [8,9]. Thus, FGMs can be utilized to produce novel properties and/or functionalities that are impossible to obtain with traditional homogeneous materials, as well as a variety of additional industrial uses [10].

Functionally graded materials (FGM) are advanced composite materials that differ from traditional composite materials in that the transition zone, which is a sharp visible interface in laminated composites, is replaced by a graduated interface that changes gradually from one material to the next, preventing the common debonding failure that is associated with traditional composite materials [11]. In the early 1980s, the FGM was introduced in Japan with the objective of lowering thermal stresses within the traditional laminated composites designed for rocket engines [12 – 15]. Japan's researchers were confronted with a challenge: they needed any sort of material for the fuselage exterior and engine components that could tolerate a large temperature difference in order to build space planes that could take off like planes. In the atmosphere, cruise at Mach 5 to 25 while being subjected to intense frictional heating from the wind. As a result, the body of the rocket needed to be made of a substance that could sustain a difference in temperature of around 1000 K between the interior and exterior of the spacecraft. Traditional composite materials and

Chapter 1: Introduction

laminated composites were both used to endure working conditions; however, none was successful. Because of the mismatch in the characteristics of the two materials, the failure frequently happened at the same location where the two materials were linked together. This composite material was subjected to thermal stress, which resulted in a thermal mismatch, and led to the separation of the two components due to their distinct expansion properties, resulting in the composite material's failure. The project's Japanese researchers concluded that the problem might be remedied by eliminating the abrupt contact between the two components that make up the composite material. Nevertheless, the formation of FGM is accomplished by substituting the sharp contact with a gradient interface that combines both components [16]. As a result of the fact that FGMs are a form of novel composite material that undergoes a progressive structure or compositional change in relation to location, the sharp interface is replaced by the gradient interface [17,18]. Thus, FGM was initially suggested in Japan for these excellent thermal, mechanical, and tribological properties in the 1980s for a space aircraft project.

Figs. 1.1 (a) and Fig. 1.1 (b) illustrate the schematic diagrams of the functionally graded material and the standard laminated composite material, respectively.

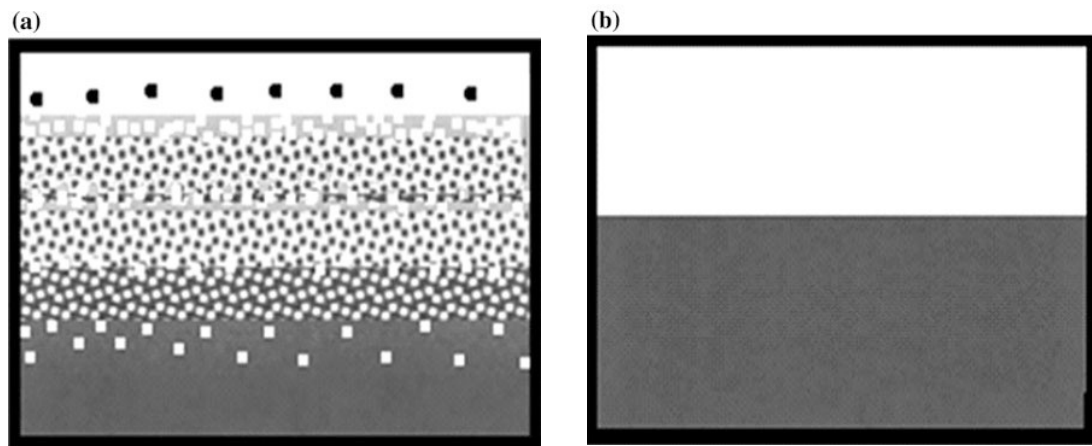


Fig. 1.1: Schematic illustration of (a) functionally graded composite and (b) typical laminated composite [9].

An FGM's structural unit is called a material ingredient or an element [19 – 20]. In addition, it is the basis for producing an FGM, which encompasses different characteristics of its physical condition, chemical composition, as well as

Chapter 1: Introduction

geometrical arrangement, and the name “material component” best reflects the complete notion [21]. The material constituents that can be utilized to fabricate FGMs are listed in Table 1.1.

Two distinct material characteristics might gradually vary from one another or in an abrupt manner, such as stepwise gradation, as shown in Fig. 1.2 (a) and Fig. 1.2 (b), respectively.

Table 1.1: Types of material constituents involved in the fabrication of FGM

Physical	dipole moment, ionic state, magnetic moment bandgap, barrier, electronic state, potential well, crystalline state
Biological	cell, complex macromolecule, tissue, organelle
Geometrical	fiber, granule, platelet rod, sheet pore, orientation, needle, texture
Chemical	metal, ceramic, polymer, organic, inorganic

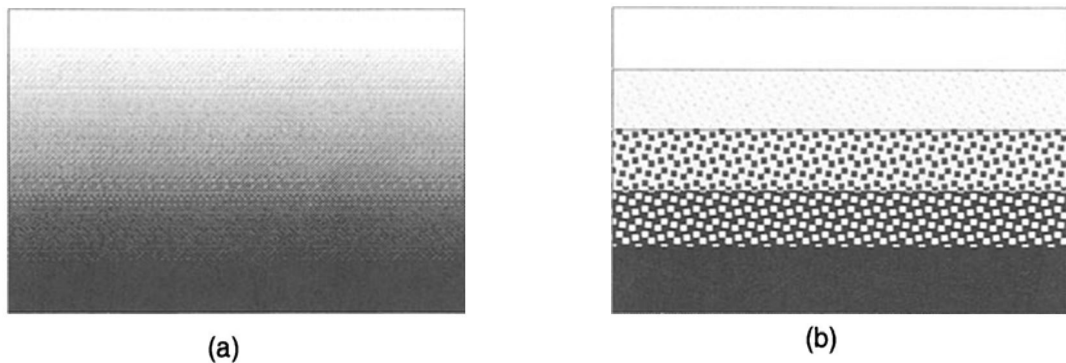


Fig. 1.2: (a) Continuous and (b) Stepwise distribution [21].

Despite the fact that the FGM was originally developed for providing a thermal barrier to the materials involved in fusion reactors and aircraft structural applications, its applications have since been expanded to include other areas, such as harsh wear-resistant environments [22,23]. Moreover, FGMs are being utilized in a variety of sectors right now, and they have a lot of promise for future uses [24]. The functionally graded materials’ application ranges are depicted in Fig. 1.3.

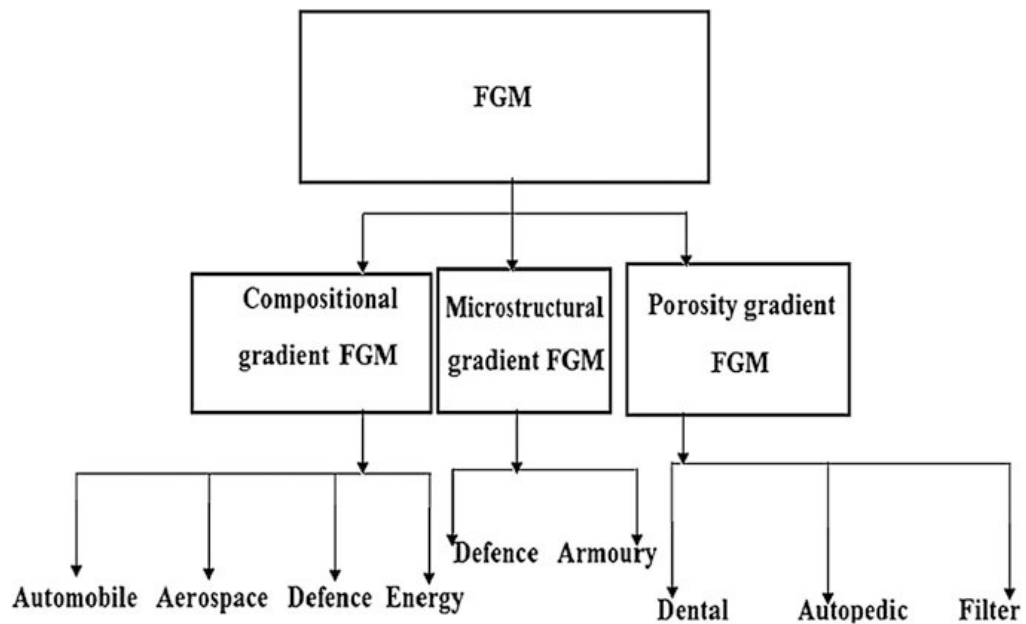


Fig. 1.3: Variety of applications of Functionally Graded Materials [24].

Gradients of composition FGM is a sort of functionally graded material in which the chemical composition of a substance that may exist as either a single or a multi-phase structure gradually changes according to its geographical location. However, composition in an FGM of single-phase is uncommon, but materials having a multiphase chemical composition are the most widely designed and utilized functionally graded materials [25,26]. Furthermore, the cylinder's outermost portion would cool more slowly in the microstructural gradient FGM shown in Fig. 1.4 (a), which would facilitate the creation of an even more balanced microstructure and generate a substantially equiaxed microstructure, both of which are ideal for usage in turbine applications, cams or ring gear, case-hardened steel, bearings or shafts, and also in the defence and armoury applications [24,27]. Lastly, the porosity gradient FGM is a type where the porosity of the material changes in response to changes in the bulk material's spatial location, as shown in Fig. 1.4 (b).

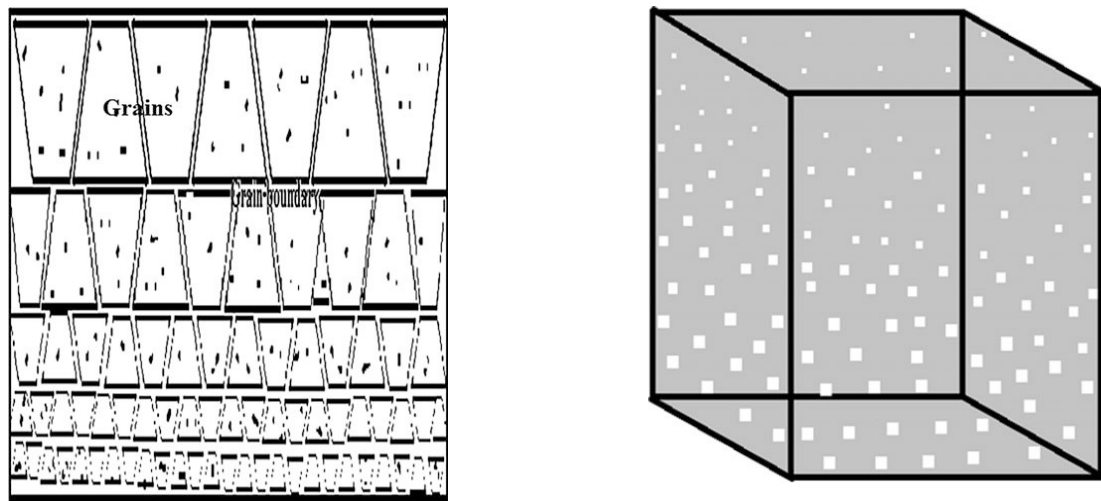


Fig. 1.4: (a) Schematic depiction of graded microstructure and (b) porosity gradient FGM [25].

Despite the fact that the first use of FGM was in Japanese spacecraft, this technology currently has a wide range of applications, some of which are described below,

Automobile: Engine cylinder liners, diesel engine pistons, combustion chambers, flywheels, shock absorbers, leaf springs, driveshafts, racing car brakes, etc.

Aerospace: The space shuttle, turbine wheels (operating above 40,000 rpm), rocket nozzle, solar panels, spacecraft truss structure, nosecones and the leading edge of missiles, camera housing, heat exchange panels, reflectors, etc.

Defence: The capacity to suppress fracture development is one of the essential properties of functionally graded materials. This feature makes it valuable in defense applications, such as armor plates and bullet-proof vests, as a penetration-resistant material.

Energy: Energy conversion devices take advantage of FGM. In addition to this, they serve as a barrier to thermal stress and are applied as a coating for protection on the blades of gas turbines.

Medicine: Living tissues, such as bones and teeth, are functionally graded materials found in nature. To replace these tissues, a suitable material that fulfills the original

Chapter 1: Introduction

bio-function tissue is required. Functionally graded material is the best choice for this job. For tooth and bone replacement, FGM offers a wide variety of applications in dentistry and orthopedics.

Commercial and Industrial: Cutting tool inserts, drilling motor shafts, fuel tanks, firefighting air bottles, pressure vessels, helmets, laptop cases, musical instruments, MRI scanner cryogenic tubes, X-ray tables, eyeglass frames, wind turbine blades, etc.

1.2 Fabrication Processes of FGMs

The production of an FGM was difficult and expensive in the beginning. Various researchers have created a variety of manufacturing processes in recent years, some of which are now employed in mass production in the industry. Fig. 1.5 demonstrates some of the most typical FGM fabrication processes.

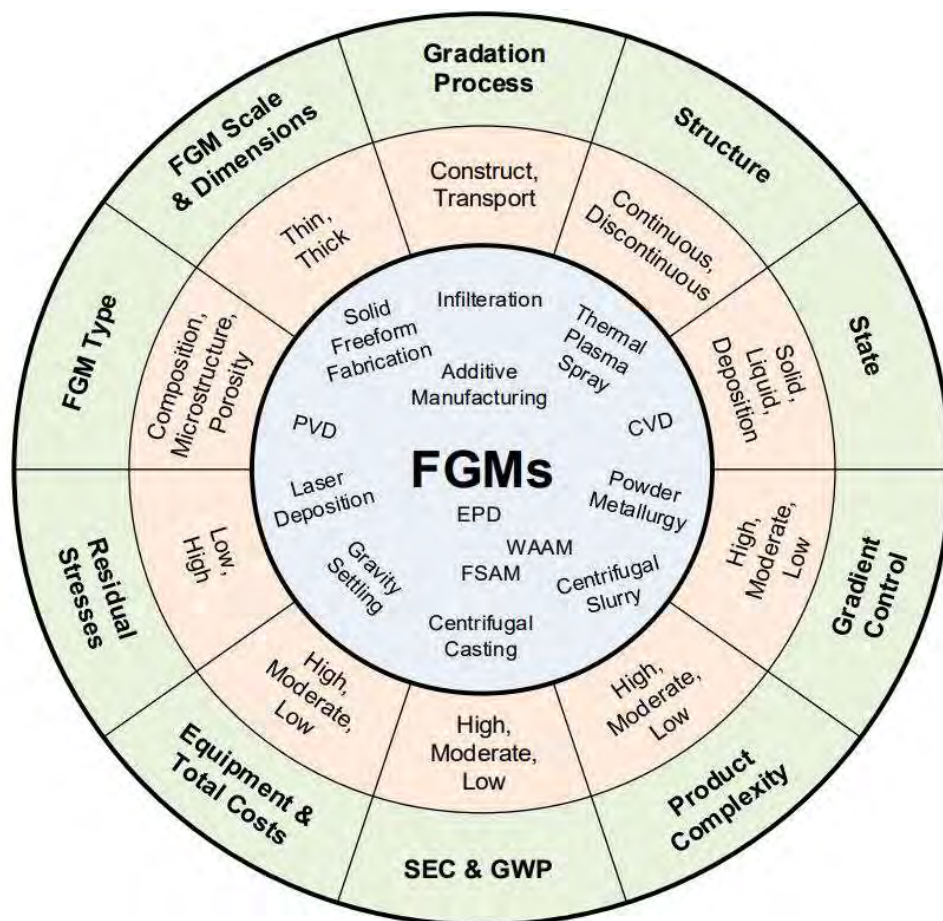


Fig. 1.5: FGMs fabrication techniques [28].

Chapter 1: Introduction

Thermal spray is one of the most promising approaches for creating coating of FGM with materials having a high melting point and precise material distribution control among the various coating technologies discussed above. Fig. 1.6 illustrates the fundamental characteristics of a thermal spray approach. The coating's unprocessed components are melted, which is accomplished with the help of the heat source. Then by processing with gases followed by spraying on the base material, the molten or liquid substances are pressured until they solidify to form a solid layer. [29].

Thermal spraying involves introducing feedstock (such as wire, rods, or powder) with a heat sources like combustion plasma, laser beams or arcs. The electrically conductive wire is used as a feedstock in arc spray techniques, whereas powder or wire is used in combustion techniques. Plasma or laser beam spraying is done using powders. The particles melt as they travel and collide with the substrate, flattening, rapidly solidifying, and depositing by consecutive impingement. The use of thermal spraying is most often utilized in the production of protective coatings made of metal, ceramic, or polymer; however, this technique may also be utilized to produce bulk ceramics [30 – 32]. When constructing FGMs by thermal spraying, their comparatively large porosity should be taken into mind.

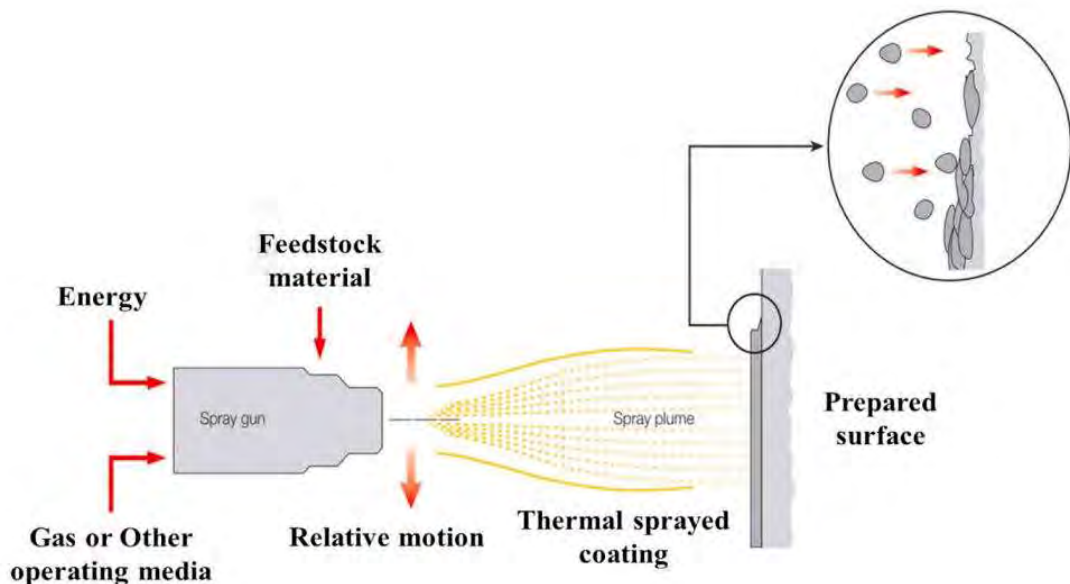


Fig. 1.6: Schematic illustration of Thermal Spray Method.

Chapter 1: Introduction

Nonetheless, another efficient method for fabricating bespoke material compositions using premixed powders is laser metal deposition (LMD). The deposited material should have a comparable or identical composition to the powder combination that was delivered. To guarantee a correct composition, the regulation of mixing should be examined. A single nozzle may provide powders of several materials that have been premixed. In the presence of a flow of argon gas, pre-mixed powders, however, can induce particle separation and a considerable divergence from the predicted composition due to differences in material density, powder size, and powder shape. Fig. 1.7 exemplifies this point. The as-deposited part's true composition may differ from the initial particle A/B ratio [33]. Powders manufactured from various materials can be given separately by several nozzles in addition to premixed powders [34]. Distinct powders in different hoppers allow for greater composition control and prevent segregation [35].

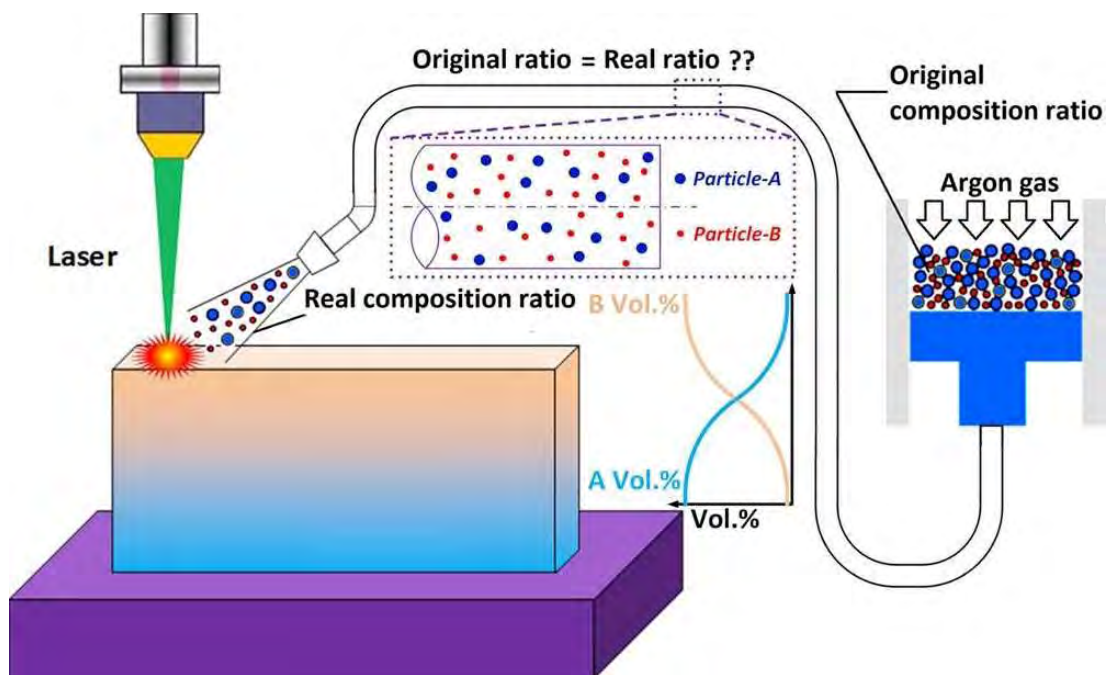


Fig. 1.7: Schematic diagram of fabricating FGM by LMD [33].

Chapter 1: Introduction

In spite of being one of the oldest approaches to manufacturing components, powder metallurgy is being used in the production of FGMs in recent days [10] and is currently one of the most often used methods in this sector [36] due to its numerous advantages. Additionally, it is one of the most important solid-state procedures for the production of bulk FGMs that have continuous gradient features [37,38]. Mixing, stacking, pressing, and sintering are the four fundamental processes in this approach for producing FGMs, as shown in Fig. 1.8 [39].

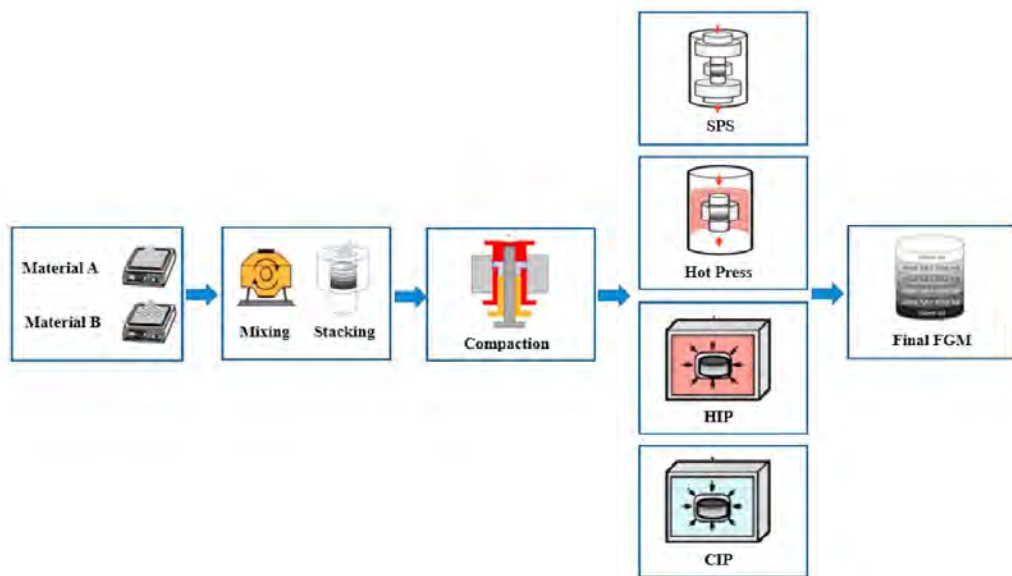


Fig. 1.8: Steps involved in powder metallurgy to produce FGM.

1.3 Statement of the Problem

In the present study, a disk made of functionally graded material (FGM) is analyzed, and the problem's analytical model is presented in Fig. 1.9. The outer radius of the disk is b , and there is a concentric hole with a radius of a . Moreover, the disk rotates at an angular velocity specified by the equation $\omega = 2\pi N/60$, where N is the number of revolutions per minute (rpm). The FGM disk is assumed to be made up of two materials, A and B , whose volume fractions are represented by V_A and V_B , respectively.

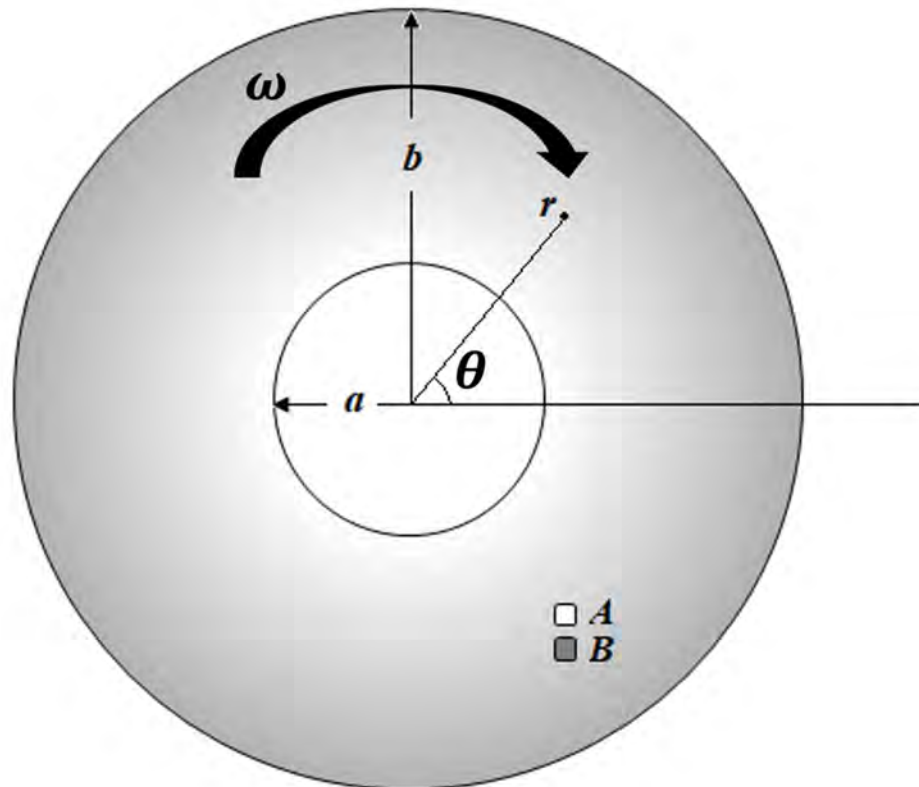


Fig. 1.9: Analytical model of the FGM disk.

Chapter 1: Introduction

The material distribution of the FGM disk is assumed to change from the inner to the outer surface only. For instance, the inner surface of the disk is made up of 100% A , while the outer surface is made up of 100% B , thus V_A decreasing from 1 to 0, as demonstrated in Fig. 1.9. The current work is developed an optimization model to compute the optimum material distribution for the FGM disk based on the minimum or prescribed stress. Therefore, it is not mandatory that the inner and outer surfaces be entirely comprised of A and B , respectively, and the variation in volume fraction may also be nonlinear. The mathematical model of the inverse problem determines the material distribution profile in the FGM disk corresponding to the minimum/prescribed stress.

Fig. 1.9 depicts a polar coordinate system $r - \theta$ with its origin at the center of the hole in the disk. Therefore, all of the properties of the FGM disk are functions of r only. As a result, along the radial distance r , all properties of the disk vary continually from the inner to outer surfaces. Hence the current model is simplified to an axisymmetric problem. Nonetheless, the properties of the FGM disk at a point are considered to be the same in all directions at that point. Thus, the FGM disk has been considered isotropic. In addition, due to the disk's modest constant thickness, the study is performed under plane stress conditions.

1.4 Objectives

The present work focuses on the inverse problem of evaluating optimum material distributions in a rotating circular FGM disk subjected to a thermal load and an inertia force due to rotation of the disk for the minimization of stresses. The specific aims of the present work are,

- i. To develop a mathematical model of inverse problem for evaluating optimum material distributions corresponding to minimum/prescribed stresses in rotating circular FGM disks under thermal and inertia loads.
- ii. To validate the mathematical model by applying it to simplified problems of three references available in the literature.
- iii. To apply the model for evaluating optimum material distributions corresponding to minimum stresses.
- iv. To apply the model for evaluating material distributions corresponding to a prescribed stress distribution.
- v. To analyze the effects of temperature field, angular speed, and aspect ratio of the disk on material distributions and corresponding stress fields.

1.5 Motivation of the Present Work

The excellent benefits of FGMs over traditional monolithic and composite materials encouraged researchers to investigate the practical and prospective uses of FGM beams, plates, cylinders, disks, shells, and pipes as structural components. Chakraborty *et al.* [40] developed a novel beam element to investigate the thermoelastic behavior of functionally graded beam structures, taking into account both exponential and power-law variations in material property distribution to investigate various stress variations. Likewise, Kiani *et al.* [41] hypothesized that material nonhomogeneous properties vary uniformly over the beam thickness when analyzing the buckling analysis of functionally graded material (FGM) beams with surface-bonded piezoelectric layers that are exposed to both heat loading and constant voltage. For evaluating displacement and stress fields, Ben-Oumrane *et al.* [42] studied an elastic, rectangular, and simply supported sigmoid functionally graded material (S-FGM) beam of substantial thickness that was exposed to evenly distributed transverse loads. Şimşek [43] evaluated the buckling of beams with various boundary conditions using two-dimensional functionally graded materials, with the assumption that the material characteristics of the beam fluctuate in both the axial and thickness directions according to the power-law form. In addition, under various forms of thermal stress, Kiani and Eslami [44] looked into the buckling of functionally graded material beams, assuming that the mechanical and thermal nonhomogeneous properties of the beam vary gradually by the distribution of power-law over only the thickness of the beam. Stresses were analyzed by Jabbari *et al.* [45 – 47] in a thick hollow cylinder comprised of functionally graded material, in which material characteristics change throughout the radius according to a power-law distribution. Furthermore, power-law material distribution was also used by Shao [48] to investigate the temperature, displacements, and thermal/mechanical stresses in a functionally graded circular hollow cylinder. Abbas [49] considered temperature-dependent material properties defined by power-law distribution to compute the thermal stresses in a thick-walled FGM cylinder, whereas the computational method of Awaji and Sivakumar [50] assessed the temperature and stress distribution with temperature-independent material properties.

Chapter 1: Introduction

FGM beams, plates, and cylinders were used to determine thermoelastic properties such as stress, strain, and displacement along with buckling of the FGM beam, where researchers adopted an assumed or prescribed material distribution according to power-law function, as is clear from the preceding literature survey. Nevertheless, specific power-law variations, such as exponential and sigmoid functions, were sometimes used to vary the material properties throughout the FGM.

To investigate stresses and displacements, Bayat *et al.* [51] characterized material properties based on the shape of the power-law distribution in axisymmetric spinning disks formed of functionally graded material with varying thickness. Durodola and Attia [52] likewise utilized numerous variations of prescribed distribution of material properties to predict stresses and displacements in functionally graded rotating disks. In addition, for investigating the distribution of stresses and displacement, Zenkour [53] exploited functionally graded material (FGM) solid disks with properties that change exponentially in the radial direction. Nikbakht *et al.* [54] presented research on FG beams, plates, and shells, as well as different structures such as tubes, implants, revolving disks, sports instruments, and so on, where the FGM's prescribed thermo-mechanical characteristics were expressed using various functions: power-law, piece-wise cubic interpolation function, B-Spline Basis Function, exponential function, Mori-Tanaka Scheme, etc.

It is obvious from the aforementioned literature that FGM beams, plates, cylinders, disks, shells, and pipes were investigated for thermo-mechanical characteristics corresponding to the prescribed exponential or power function or other relevant variation of material distributions. Thus, the properties of two distinct materials in FGM change progressively from one to the other in accordance with an assumed profile in each instance. However, while minimum or prescribed thermo-mechanical characteristics are required in an FGM for any specific application, it is nearly impossible to predict the desired thermo-mechanical characteristics based on an assumed variation of material distribution because no exponential function, power function, sigmoid function, or even other relevant function can reveal all types of variations of material distribution required to ensure the desired characteristics. In

Chapter 1: Introduction

addition, a circular cutter or grinding disk fabricated from FGMs with a minimum stress profile can have superior efficacy and endurance, and in some cases, a desired stress field may be required in these cutters or grinding disks for a specific purpose. Because FGM disks are comparable to cutters and grinding disks, and their stress profile substantially influences their durability and efficiency, comprehending the minimum/prescribed stress profile in FGM disks may be a very significant concern for designers. As a result, the minimum/prescribed stress profile in FGM disks is more tangible and essential to estimate than other stress profiles in FGM disks. Moreover, in real-world applications, the cutters and grinding disks are always subjected to thermal load. Because of the preceding reasons, the author was motivated to consider the problem of stress minimization in a rotating circular FGM disk subjected to a thermal load and an inertia force due to disk rotation by evaluating optimum material distribution. This can be achieved by developing an inverse problem that predicts the optimum material distributions corresponding to the minimum/prescribed stress.

CHAPTER 2

LITERATURE REVIEW

In the literature, a number of works to determine the thermo-mechanical and thermoelastic properties of functionally graded material (FGM) cylinders, plates, shells, pipes, and disks have been presented in which the material characteristics are considered to vary according to an exponential function or power functions.

2.1 Different FGM Bodies

A power-law distribution was considered by Reddy and Chin [55] to alter the volume percentage of a ceramic and metal when studying the dynamic thermoelastic response of functionally graded cylinders and plates exposed to thermal stress. Chi and Chung [56,57] utilized a rectangular, simply supported, functionally graded material (FGM) plate of medium thickness subjected to transverse loading with young's moduli varying continuously throughout the thickness direction according to the volume fraction of constituents defined by power-law as well as sigmoid, or exponential function, in order to determine developed stress, strain, and displacement. Tutuncu [58] obtained the results for stresses and displacements in functionally graded cylindrical vessels subjected to internal pressure alone, where the material was considered to have an exponentially changing elastic modulus throughout the thickness. To carry out the thermo-mechanical study, Shao and Ma [59] also used an exponential material distribution of functionally graded hollow circular cylinders subjected to mechanical loads and a linearly rising boundary temperature. To explore the effect of material characteristics, shell geometry, and thermomechanical loading on the stress field, Woo and Meguid [60] used shallow shells built of functionally graded materials (FGMs) under transverse mechanical loads and a temperature field. Woo and Meguid [60] also adopted a prescribed distribution of material properties of the functionally graded shells, which were expected to change continuously along the thickness of the shell, according to a power-law distribution of the volume fraction of the components, just like the

Chapter 2: Literature Review

previous investigations. In order to predict the critical mechanical buckling stresses of the FGM cylindrical shells encased in elastic media, a similar distribution of material properties was considered by Bagherizadeh *et al.* [61]. Arshad *et al.* [62] calculated natural frequencies for a circular cylindrical shell made of functionally graded material (FGM) with simply supported edge conditions, using algebraic polynomial, exponential, and trigonometric volume fraction laws to specify the material characteristics. Considering temperature variations for different distributions of material properties, Dai *et al.* [63] studied several critical flow velocities of axially functionally graded material (FGM) pipe conveying fluid. Variations in properties of materials were developed throughout the pipe using a power-law distribution of the volume fraction of the components, as well as exponential and sigmoid functions [64]. In addition, the effect of the volume fraction exponent, fluid velocity, internal pressure, and internal damping on the stability of FGM pipes transporting fluid was explored by Deng *et al.* [64,65].

2.2 FGM Disks

Kordkheili and Naghdabadi [66] measured stress, strain, and displacement in a rotating Functionally Graded hollow disk subjected to thermal loading, in which the thermomechanical characteristics of the FGM disk's constituent components were represented by power-law variation. For the stress analysis, Hosseini *et al.* [67] employed a revolving nano-disk consisting of functionally graded materials with nonlinearly variable thickness, assuming the same material variation as Kordkheili and Naghdabadi [66]. Tutuncu and Temel [68] also used the same power-law variation to compute corresponding stresses and displacements for functionally graded hollow cylinders, disks, and spheres under uniform internal pressure. Timoshenko and Goodier [69] carried out a thermoelastic analysis of a rotating homogeneous disk without any thermal load. A hollow disk subjected to thermal load was considered by Sadd [70] to determine developed stresses in the disk. Madan *et al.* [71] assumed linear variation of material distribution profile in the rotating FGM disk subjected to inertial force only due to its rotation in order to calculate the stresses, strains, and displacement for different radial thicknesses of the FGM disk.

Chapter 2: Literature Review

Afsar and Go [72] investigated the influence of the temperature distribution profile, radial thickness of the disk, angular speed of the disk, and the difference in temperature between the inner and outer surfaces on the thermoelastic field in the disk using a rotating FGM disk with an exponential variation of material properties. A similar analysis was carried out by Go *et al.* [73]. Comparable findings were obtained by Arnab *et al.* [74]; however, the study used both power functions and exponential variation to predict the mechanical and thermal characteristics of the FGM disk. On the contrary, Afsar *et al.* [75] used an FGM disk with a coating on the outer surface for a thermoelastic study of the same type by employing exponential material variation. Further research on the elastic field of a functionally graded rotating disk is found in [76–80], which took into account power-law [76 – 79] and exponential [80] change of material properties. In addition, Madan *et al.* [81,82] implemented the power-law variation for the material parameters to compute stress variation in order to achieve correct limit angular speeds. Likewise, utilizing power-law variation, Bakhshi *et al.* [83] estimated the radial displacement, radial stress, and hoop stress of an FGM disk that was supposed to be under axisymmetric thermal shock given to its inner surface in order to examine thermoelastic behavior.

Damircheli and Azadi [84] and Madan and Bhowmick [85, 86] used FGM disks with varying thicknesses to conduct thermal and mechanical stress analyses, assuming that the material characteristics vary using a power-law variation [84,85], exponential function [85], sigmoid function [85], and trigonometric function [86] to establish prescribed material distribution. Also, a thermoelastic study of functionally graded non-uniform rotating disks exposed to nonuniform temperature change utilizing the same power-law variation was carried out by Tutuncu and Temel [87]. Farimani and Mohadeszadeh [88] analyzed the thermoelastic bending characteristics of a solid rotating plate having roller supports on the external edge. Moleiro *et al.* [89] analyzed FGM plates under thermo-mechanical loadings to minimize stress, deformation, and mass. The material properties of both FGM plates were specified using a power-law distribution of metal-ceramic volume fractions. To analyze the thermo-mechanical features of plastic limit speed in functionally graded material

Chapter 2: Literature Review

discs, Farimani and Toussi [90] used the same variation for material characteristics as well as thickness.

The above literature reveals that prescribed material distribution was considered for determining thermo-mechanical properties and elastic field of all considered rotating FGM disks, assuming material properties to vary according to an exponential function, power functions, sigmoid function, and so on. Although it is usual in applied mechanics research to deal with FGMs by assuming that their material characteristics vary according to various functions, several studies focused on designing optimization models incorporating inverse problems to optimize various FGM parameters. In the following part of the literature survey, some inverse problems for optimizing different parameters of FGM will be addressed.

2.3 Optimization Models for FGM

The thermomechanical behavior of FGMs in advanced materials is highly impacted by the spatial distribution of the volume fraction. Therefore, for a particular requirement and loading situation, determining the volume fraction distribution becomes an important aspect of the FGM design. Cho and Ha [91] optimized the volume fraction of a simply supported FGM beam and an axisymmetric FGM cylinder to reduce steady-state thermal stresses. However, instead of computing the temperatures based on the determined distribution of material properties, in this inverse study, the temperatures within the beam and cylinder were assumed to fall uniformly, fulfilling boundary conditions. Despite the fact that Ootao *et al.* [92] devised an optimization problem for reducing thermal stress distribution in an FGM hollow circular cylinder, the model was unable to anticipate all types of material distribution since it only included the optimization of the power index of the power-law variation for material distribution. In addition, Khatir *et al.* [93] proposed an optimization model employing an Artificial Neural Network to examine damage detection, localization, and quantification in Functionally Graded Material (FGM) plate structures using a power-law distribution of the plate constituents' volume fractions. However, Yasinsky and Tokova [94] analyzed the temperature and

Chapter 2: Literature Review

thermal stress distribution in the cylinder by solving an inverse thermoelasticity problem that involved just five different types of thermophysical and mechanical characteristics of the material. Similarly, Cárdenas-García *et al.* [95] analyzed an FGM infinite plate with a hole, assuming that material characteristics change according to a gradation function, and evaluated the gradation function coefficients for known thermal load and material behavior to predict the properties. Liu *et al.* [96] provided a computational inverse approach for characterization of the material properties of functionally graded materials utilizing the plate's surface displacement response. With an initial prediction of up to 40% off from genuine values, this method might predict the material characteristics of an FGM. Nonetheless, in actuality, this form of prediction is unfeasible. Furthermore, inverse problems were also considered in order to determine optimum material distributions for prescribed apparent fracture toughness of FGM bodies of different geometries [97 – 99].

The preceding literature reveals that rotating FGM disks with or without a concentric hole were considered for the analysis of thermo-mechanical characteristics corresponding to prescribed exponential or power function or other relevant variations of material distributions. The prescribed material distributions may not be suitable to realize desired thermo-mechanical characteristics required for a specific application. Furthermore, neither of the aforementioned researchers devised an optimization model for the inverse problem to anticipate the material distribution of the FGM disk corresponding to the minimum/prescribed stresses. Although various researchers constructed optimization models for FGM beams, cylinders, and plates, these models failed to predict all types of material distribution in such FGMs. Thus, only a limited number of material distributions can be predicted using these models. In addition, it is impossible to precisely predict material distribution for desired thermo-mechanical properties using these models since they can only predict limited distributions, and the prediction must contain significant errors. Therefore, the present work availed the unique opportunity to develop this optimization model. To achieve this goal, the present study focuses on inverse methods to be employed for obtaining a desired characteristic in FGM disks by evaluating an optimum material distribution. Finally, the thermoelastic properties of FGMs were determined in the

Chapter 2: Literature Review

majority of the research in the above literature review by considering an assumed temperature profile; however, these assumed temperature distributions might not be realized in practice for the corresponding material distribution. Thus, in this study, the temperature profile of the FGM disk is determined. In other words, the temperatures between the FGM disk's inner and outer surfaces are calculated.

CHAPTER 3

THEORY

3.1 Effective Properties of FGM

An adequate and efficient mixing rule model is required to compute the effective properties of FGM. The microstructure of FGMs changes with the volume fractions of the constituents, and a dispersive phase on one side of FGMs transitions to a matrix phase on the other side; therefore, the mixture rule formulated for conventional composites cannot be used for FGMs. Furthermore, on one side of FGMs, a dispersive phase converts into a matrix phase on the other. Thus, when formulating a mixing rule for FGMs, additional care must be taken. As a result, the models proposed by Wakashima and Tsukamoto [100] and Nan *et al.* [101] are used in this work to compute the effective characteristics of the FGM disk since they appear to be more accurate over a wider range of constituent volume fractions. The mixture rule can be summarized as follows for an FGM whose constituents are A and B ,

$$K = V_A K_A + V_B K_B + V_A V_B \frac{(K_A - K_B) \left(\frac{1}{K_A} - \frac{1}{K_B} \right)}{\frac{V_A}{K_A} + \frac{V_B}{K_B} + \frac{4G_A}{3K_A K_B}} \quad (3.1)$$

$$G = V_A G_A + V_B G_B + V_A V_B \frac{(G_A - G_B) \left(\frac{1}{G_A} - \frac{1}{G_B} \right)}{\frac{V_A}{G_A} + \frac{V_B}{G_B} + \frac{9K_A + 8G_A}{6G_A(K_A + 2G_A)}} \quad (3.2)$$

where V is the volume fraction, K is the bulk modulus, and G is the shear modulus. The properties of the constituent materials A and B are denoted by the subscripts A and B of a variable, whilst the properties of the FGM formed of the materials A and B are represented by the non-subscripted variables.

Chapter 3: Theory

Moreover, the shear modulus of elasticity and the bulk modulus of constituents A and B may be obtained using the formulae below.

$$K_i = \frac{E_i}{3(1 - 2\nu)} \quad (3.3)$$

$$G_i = \frac{E_i}{2(1 + \nu)} \quad (3.4)$$

where

$$i = A, B$$

Once the bulk modulus and shear modulus of the FGM are known, the following relationships may be used to readily calculate other FGM properties.

$$E = \frac{9KG}{(3K + G)} \quad (3.5)$$

$$\alpha = V_A \alpha_A \frac{K_A(3K + 4G)}{K(3K_A + 4G)} + V_B \alpha_B \frac{K_B(3K + 4G)}{K(3K_B + 4G)} \quad (3.6)$$

E is the Young's Modulus, and α is the coefficient of thermal expansion of FGM. However, as a material's density is independent of its shear and bulk modulus, the Reuss Model [102] would be used to compute density variation. Likewise, the Reuss Model [102] may also be used to calculate the thermal conductivity of the FGM disk. Thermal conductivity, k , and density, ρ are given by,

$$k = \frac{k_A k_B}{V_A k_B + V_B k_A} \quad (3.7)$$

$$\rho = \frac{\rho_A \rho_B}{V_A \rho_B + V_B \rho_A} \quad (3.8)$$

3.2 Discretization Scheme

The domain of the FGM disk is divided radially into N number of elements of equal size in accordance with a standard finite element discretization scheme. The discretized FGM disk is illustrated in Fig. 3.1, where for the i^{th} element $i = 1, 2, \dots, N$. The inner and outer radii of the i^{th} element are r_i and r_{i+1} , respectively, where $i = 1, 2, \dots, N$. Similarly, for the N^{th} element, the inner and outer radii of the FGM disk are r_N and r_{N+1} , respectively. Therefore, r_1 and r_{N+1} can be defined as the inner and outer radii of the FGM disk, a and b , respectively.

In Section 4.1.3, an elaborate discussion of the finite element discretization approach as well as the finite element formulation of the FGM disk for the current study is mentioned.

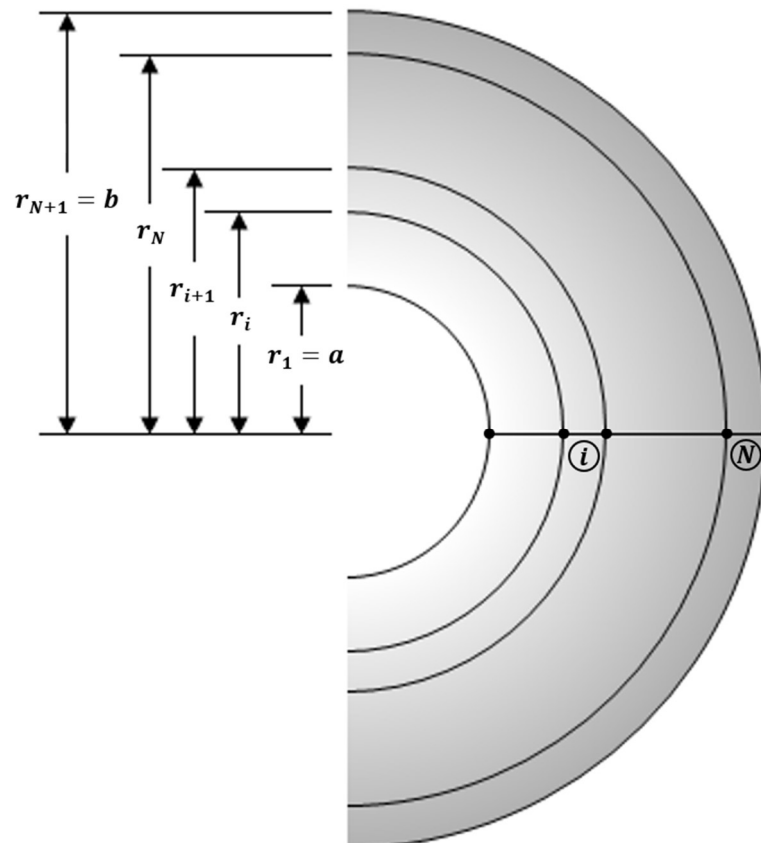


Fig. 3.1: Discretization of the FGM Disk.

3.3 Temperature Distribution of the FGM Disk

The present work looks at steady-state heat conduction in the absence of an internal heat source. As a result, conduction heat transfer is reduced to

$$\frac{1}{r} \frac{d}{dr} \left[r k \frac{dT}{dr} \right] = 0 \quad (3.9)$$

Here, it should be mentioned that the thermal conductivity k is a function of r only. T is the temperature distribution which is also function of r only. The heat conduction equation mentioned above satisfies the following boundary conditions,

$$T(a) = T_1 \quad (3.10)$$

$$T(b) = T_2 \quad (3.11)$$

The assumption that material of the FGM is isotropic makes it fairly simple to solve this equation utilizing the aforementioned boundary conditions. The thermal conductivity at the i^{th} point is denoted by the k_i . Using local radius variables r_i , we can express the temperature distribution as follows [103]:

$$T(r_j) = T_1 + C(T_2 - T_1) \left(\sum_{i=2}^s \frac{\ln \left(\frac{r_i}{r_{i-1}} \right)}{k_i} + \frac{\ln \left(\frac{r_j}{r_s} \right)}{k_s} \right) \quad (3.12)$$

where

$$j = 2, \dots, N$$

$$C = \frac{1}{\sum_{i=2}^{N+1} \frac{\ln \left(\frac{r_i}{r_{i-1}} \right)}{k_i}} \quad (3.13)$$

$$a = r_1 < r_2 < \dots < r_{N+1} = b \quad (3.14)$$

$$r_s < r \leq r_{s+1} ; s = 1, \dots, N \quad (3.15)$$

$T(r_j)$ denotes the temperature at any point r_j . In addition, using the formulae for the effective characteristics of FGM, the thermal conductivity k at any nodal point may be calculated based on the volume fraction at that point. Therefore, the boundary conditions decide the temperatures at the inner and outer surfaces of the FGM disk, and the temperatures between the inner and outer surfaces are computed utilizing *Eqs. (3.7) and (3.10) to (3.15)*.

It's worth mentioning that *Eqs. (3.10) to (3.15)* may be used for both homogeneous and FG materials. In the instance of homogeneous material, a constant value of k will be used; however, in the case of FGM, a variation of k corresponding to the material distribution will be used.

3.4 Thermoelastic Formulation

Eigenstrains are nonelastic or free expansion strains that emerge in a body for a variety of reasons, including phase transition, precipitation, thermal expansion owing to temperature change, and so on [104]. Thus, in order to acquire the subsequent consequences, the incompatibility of these eigenstrains causes stresses that must be taken into consideration along with other loadings. In the present work, the eigenstrain is correlated to the thermal expansion of the FGM disk as the temperature changes. Moreover, because the FGM disk's material is considered to be isotropic, the thermal eigenstrain at a given point is the same in all directions, as given by

$$\varepsilon^* = \alpha(r)T(r) \quad (3.16)$$

Here, $T(r)$ denotes the temperature change at any point r . The elastic and eigen strains are added to get the overall strain. As a result, the total strain components are as follows:

$$\varepsilon_r = e_r + \varepsilon^* \quad (3.17)$$

$$\varepsilon_\theta = e_\theta + \varepsilon^* \quad (3.18)$$

where, ε_r and ε_θ are the radial and circumferential components of total strain, respectively, whereas e_r and e_θ are the radial and circumferential components of elastic strain. Furthermore, due to the symmetric deformation of the disk, the shear strain component does not come into consideration. Hooke's law describes the relationship between elastic strains and stresses for plane stress condition [105,106].

Therefore,

$$\varepsilon_r = \frac{1}{E}(\sigma_r - \nu\sigma_\theta) + \varepsilon^* \quad (3.19)$$

$$\varepsilon_\theta = \frac{1}{E}(\sigma_\theta - \nu\sigma_r) + \varepsilon^* \quad (3.20)$$

Chapter 3: Theory

Here, the radial and circumferential stress components are σ_r and σ_θ , respectively. Now, the two-dimensional equilibrium equations in polar coordinate may be expressed by taking the inertia force owing to the rotation of the disk as the only body force [107].

$$\frac{d\sigma_r}{dr} + \frac{1}{r} \frac{d\tau_{r\theta}}{d\theta} + \frac{\sigma_r - \sigma_\theta}{r} + \rho\omega^2 r = 0 \quad (3.21)$$

$$\frac{d\tau_{r\theta}}{dr} + \frac{1}{r} \frac{d\sigma_\theta}{d\theta} + \frac{2\tau_{r\theta}}{r} = 0 \quad (3.22)$$

The FGM disk is an axisymmetric disk, as previously stated. As a result of the symmetry, $\tau_{r\theta}$ disappears and σ_r, σ_θ are independent of θ . Thus, *Eq. (3.22)* is automatically satisfied, and *Eq. (3.21)* is simplified to

$$\begin{aligned} \frac{d\sigma_r}{dr} + \frac{\sigma_r - \sigma_\theta}{r} + \rho\omega^2 r &= 0 \\ \Rightarrow \frac{d}{dr}(r\sigma_r) - \sigma_\theta + \rho\omega^2 r^2 &= 0 \end{aligned} \quad (3.23)$$

Assuming,

$$r\sigma_r = F \quad (3.24)$$

Thus, *Eq. (3.23)* becomes,

$$\begin{aligned} \frac{dF}{dr} - \sigma_\theta + \rho\omega^2 r^2 &= 0 \\ \Rightarrow \sigma_\theta &= \frac{dF}{dr} + \rho\omega^2 r^2 \end{aligned} \quad (3.25)$$

Substituting Eq. (3.24) and Eq. (3.25) into Eqs. (3.19) and (3.20),

$$\varepsilon_r = \frac{1}{E} \left(\frac{F}{r} - \nu \frac{dF}{dr} \right) - \frac{\nu \rho}{E} \omega^2 r^2 + \varepsilon^* \quad (3.26)$$

$$\varepsilon_\theta = \frac{1}{E} \left(\frac{dF}{dr} - \frac{\nu F}{r} \right) + \frac{\rho \omega^2 r^2}{E} + \varepsilon^* \quad (3.27)$$

The strain–displacement relations are studied for the axisymmetric issue to satisfy the compatibility criterion between the strain components [106].

$$\varepsilon_r = \frac{du_r}{dr} \quad (3.28)$$

$$\varepsilon_\theta = \frac{u_r}{r} \quad (3.29)$$

From Eqs. (3.28) and (3.29),

$$\varepsilon_r = \frac{d}{dr} (\varepsilon_\theta r) \quad (3.30)$$

Substituting Eqs. (3.26) and (3.27) into Eq. (3.30),

$$\begin{aligned} \frac{d^2 F}{dr^2} + \left(\frac{1}{r} - \frac{dE}{dr} \frac{1}{E} \right) \frac{dF}{dr} + \frac{1}{r} \left(\nu \frac{dE}{dr} \frac{1}{E} - \frac{1}{r} \right) F \\ = \rho \omega^2 r \left(\frac{dE}{dr} \frac{1}{E} r - \frac{d\rho}{dr} \frac{1}{\rho} r - \nu - 3 \right) - E \alpha \left(\frac{d\alpha}{dr} \frac{1}{\alpha} T + \frac{dT}{dr} \right) \end{aligned} \quad (3.31)$$

Eq. (3.31) is the governing second-order differential equation. Once Eq. (3.31) is solved for F , the components of stress can readily be obtained from Eqs. (3.24) and (3.25). In addition, one also can easily obtain the components of strain and

Chapter 3: Theory

displacement from *Eqs. (3.26) to (3.29)*, respectively. The objective of present work is to evaluate the minimum/prescribed stress in the FGM disk. Moreover, in this study, *Eqs. (3.24) and (3.25)* may be used to calculate radial and circumferential stress, respectively.

If the minimum radial or circumferential stress is estimated individually, it will be intangible and ineffectual since the yielding or failure of the material is reliant on the value of the von Mises stress. The following equation [108] may be used to compute the von Mises stress.

$$\sigma' = \sqrt{\frac{1}{2}[(\sigma_z - \sigma_r)^2 + (\sigma_z - \sigma_\theta)^2 + (\sigma_\theta - \sigma_r)^2]} \quad (3.32)$$

Here, σ' , σ_r , σ_θ , and σ_z are von Mises stress, radial stress, circumferential or hoop stress, and axial stress, respectively. For plane stress problem, $\sigma_z = 0$. Therefore, *Eq. (3.32)* becomes,

$$\sigma' = \sqrt{\sigma_r^2 - \sigma_r\sigma_\theta + \sigma_\theta^2} \quad (3.33)$$

The equivalent von Mises stress may be easily calculated using *Eq. (3.33)* once the radial and circumferential stresses have been determined.

CHAPTER 4

NUMERICAL FORMULATION

The numerical formulation of the present study consists of two parts: the first is finite element formulation, and the second is the development of an optimization model. In order to predict the material distribution in the FGM disk for which the minimum/prescribed stress is produced, the finite element model is integrated into the optimization model to solve the inverse problem.

4.1 Finite Element Formulation

4.1.1 Variational Methods

The Ritz and weighted-residual methods are variational methods that seek an approximate solution to a differential equation in the form of a linear combination of acceptable approximation functions φ_j and parameters need to be discretized

$$c_j: \sum c_j \varphi_j$$

If the parameters c_j are unknown, the Ritz approach employs the weak form, whereas the weighted-residual technique employs the weighted-integral form. The Ritz approach, which is used in order to find a solution to the governing differential Eq. (3.31) of the current study, is the major emphasis of the finite element formulation.

Assuming the differential equation,

$$A(u) = f \tag{4.1}$$

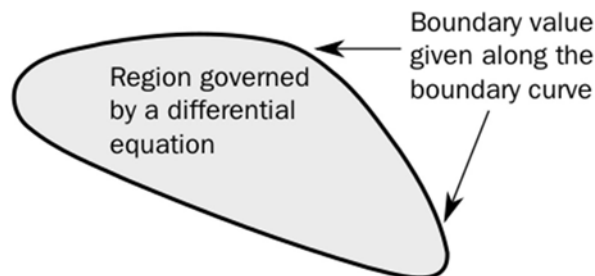


Fig. 4.1: Boundary values for an area where a differential equation is valid.

Chapter 4: Numerical Formulation

In the domain Ω with a boundary $\partial\Omega$, as illustrated in Fig. 4.2, the boundary is considered to be divided into two parts, $\partial\Omega_1$ and $\partial\Omega_2$. The boundary conditions on these two segments of boundary $\partial\Omega_1$ and $\partial\Omega_2$ are thought of as,

1. $B_1(u) = g$; on $\partial\Omega_1$ and
2. $B_2(u) = h$; on $\partial\Omega_2$.

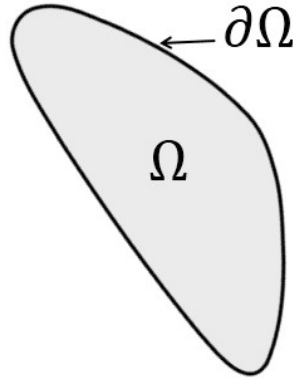


Fig. 4.2: Representation of a domain.

The dependent variable is u , the linear or nonlinear differential operator is A , the provided function in the domain is f , the boundary operators associated with the operator A are B_1 and B_2 , and the given functions on parts $\partial\Omega_1$ and $\partial\Omega_2$ of the boundary, Ω are g and h . Homogeneous differential equations are those in which $f = 0$. A homogeneous boundary condition, on the other hand, is one in which the right-hand side (for example, g or h) is zero.

Three main phases are involved in converting a differential equation with boundary conditions, such as Eq. (4.1), into variational (weak) form. These are:

1. Integrate across the provided domain of the problem by multiplying the given differential equation by an appropriate test function, w .

$$\int_{\Omega} w[A(u) - f]dx = 0 \quad (4.2)$$

The function w must be sufficiently differentiable and fulfill the essential boundary conditions in their homogeneous form. Natural boundary terms are expressed clearly in terms of u , whereas essential boundary terms have the same form as conditions

Chapter 4: Numerical Formulation

expressed in terms of the “arbitrary” function w . For instance, essential boundary conditions include $u(0) = d$ and natural boundary conditions include $A(u)(l) = m$.

2. Apply partial integration to *Eq. (4.2)* to transfer differentiation of u to w , with the partial integration’s goal being to weaken the constraints on u . In addition, the essential and natural boundary conditions can be recognized in this step.
3. Boundary terms will appear in the expressions created in the previous step, which may now be reduced using the provided boundary conditions. The desired variational form will then be the final expression.

$$B(w, u) = l(w) \quad (4.3)$$

4.1.2 Ritz Method

The approximation functions, $w = \varphi_i$, are the weight functions available in the Ritz method. The approximate solution is subjected to lower continuity restrictions than the original differential equation or its weighted-integral version since it comprises both the governing differential equation and the problem’s natural boundary conditions. For a linear variational problem, the approach is detailed here (same as weak form).

Discretization in the form of a finite series is attempted by considering the variational form deriving from the weak formulation in *Eq. (4.3)*.

$$u_N(x) = \varphi_o(x) + \sum_{j=1}^N c_j \varphi_j(x) \quad (4.4)$$

The constants c_j are referred to as the “Ritz coefficients.” If c_j is unknown after discretizing a parameter, it can be determined in such a way that *Eq. (4.3)* applies for each $w = \varphi_i$ ($i = 1, 2, \dots, N$), i.e., *Eq. (4.3)* holds for N alternative choices of w , resulting in N distinct algebraic relations among c_j . The “approximate functions” φ_j and φ_o are selected so that u_N meets the stated necessary boundary conditions.

Chapter 4: Numerical Formulation

Now, by substituting $w = \varphi_i$ ($i = 1, 2, \dots, N$) into Eq. (4.4), for c_j ($j = 1, 2, \dots, N$), a system of N equations may be formed from Eq. (4.3).

$$B\left(\varphi_i, \varphi_o + \sum_{j=1}^N c_j \varphi_j\right) = l(\varphi_i) \quad (4.5)$$

Eq. (4.5) yields as B is linear in u ,

$$\sum_{j=1}^N B(\varphi_i, \varphi_j) c_j = l(\varphi_i) - B(\varphi_i, \varphi_o) \quad (4.6)$$

$$\Rightarrow \sum_{j=1}^N K_{ij} c_j = l_i \quad ; i = 1, 2, \dots, N \quad (4.7)$$

where

$$K_{ij} = B(\varphi_i, \varphi_j) \quad (4.8)$$

$$l_i = l(\varphi_i) - B(\varphi_i, \varphi_o) \quad (4.9)$$

In matrix form, the algebraic equations in Eq. (4.7) may be written as,

$$[K]\{c\} = \{l\} \quad (4.10)$$

4.1.3 Finite Element Formulation of the Present Work

The finite element approach is used to solve the differential equation (3.31) since a close form solution is not attainable. At first, Eq. (3.31) is multiplied by a trial function w and integrated across the domain of the problem according to the variational approach, yielding:

$$\begin{aligned}
 & \int_a^b w \frac{d^2 F}{dr^2} dr + \int_a^b w \left(\frac{1}{r} - \frac{dE}{E} \right) \frac{dF}{dr} dr \\
 & \quad + \int_a^b w \frac{1}{r} \left(v \frac{dE}{E} - \frac{1}{r} \right) F dr \\
 & = \int_a^b w \left\{ \rho \omega^2 r \left(\frac{dE}{E} r - \frac{d\rho}{\rho} r - v - 3 \right) - E \alpha \left(\frac{d\alpha}{\alpha} T + \frac{dT}{dr} \right) \right\} dr
 \end{aligned} \tag{4.11}$$

Assuming that,

$$f(r) = \rho \omega^2 r \left(\frac{dE}{E} r - \frac{d\rho}{\rho} r - v - 3 \right) - E \alpha \left(\frac{d\alpha}{\alpha} T + \frac{dT}{dr} \right) \tag{4.12}$$

Thus, Eq. (4.11) becomes,

$$\int_a^b w \frac{d^2 F}{dr^2} dr + \int_a^b w \left(\frac{1}{r} - \frac{dE}{E} \right) \frac{dF}{dr} dr + \int_a^b w \frac{1}{r} \left(v \frac{dE}{E} - \frac{1}{r} \right) F dr = \int_a^b w f(r) dr \tag{4.13}$$

Integration by parts yields,

$$\begin{aligned}
 & - \int_a^b \frac{dw}{dr} \frac{dF}{dr} dr + \left[w \frac{dF}{dr} \right]_a^b \\
 & \quad + \int_a^b w \left(\frac{1}{r} - \frac{dE}{E} \right) \frac{dF}{dr} dr + \int_a^b w \frac{1}{r} \left(v \frac{dE}{E} - \frac{1}{r} \right) F dr = \int_a^b w f(r) dr
 \end{aligned} \tag{4.14}$$

Chapter 4: Numerical Formulation

$$\begin{aligned} \Rightarrow \int_a^b \frac{dw}{dr} \frac{dF}{dr} dr - \int_a^b w \left(\frac{1}{r} - \frac{dE}{dr} \right) \frac{dF}{dr} dr - \int_a^b w \frac{1}{r} \left(\nu \frac{dE}{dr} - \frac{1}{r} \right) F dr = - \int_a^b w f(r) dr \\ + w(b) \frac{dF}{dr}(b) - w(a) \frac{dF}{dr}(a) \end{aligned} \quad (4.15)$$

The following boundary condition instances are investigated for the current FGM rotating disk problem.

Case I:

- i. At $r = a$, $\sigma_r = 0$, $T = T_1$
- ii. At $r = b$, $\sigma_r = 0$, $T = T_2$

Both the inner and outer surfaces of the FGM disk are free from any type of load.

Case II:

- i. At $r = a$, $u_r = 0$, $T = T_1$
- ii. At $r = b$, $\sigma_r = 0$, $T = T_2$

The inner surface has no radial displacement since it is attached to a shaft. In addition, the outer surface of the FGM disk is free from any type of load.

Therefore, both types of boundary conditions are essential and homogenous. These boundary conditions must be satisfied by the function w .

Now, the disk's radial domain $\Omega = (a, b)$ is partitioned into N subdomains $\Omega^n = (r_n, r_{n+1})$, where $n = 1, 2, \dots, N$. Eq. (4.15) is valid in all subdomains Ω^n since it is valid throughout the domain Ω . As a result, Eq. (4.15) has the following variational form:

$$B(w, F) = l(w) \quad (4.16)$$

Chapter 4: Numerical Formulation

where

$$B(w, F) = \int_{r_n}^{r_{n+1}} \frac{dw}{dr} \frac{dF}{dr} dr - \int_{r_n}^{r_{n+1}} w \left(\frac{1}{r} - \frac{dE}{dr} \right) \frac{dF}{dr} dr - \int_{r_n}^{r_{n+1}} w \frac{1}{r} \left(v \frac{dE}{dr} - \frac{1}{r} \right) F dr \quad (4.17)$$

$$l(w) = - \int_{r_n}^{r_{n+1}} w f(r) dr + w(r_{n+1}) \frac{dF}{dr}(r_{n+1}) - w(r_n) \frac{dF}{dr}(r_n) \quad (4.18)$$

Here, the solution is assumed in the form of,

$$F = \sum_{j=1}^2 F_j^n \varphi_j^n \quad (4.19)$$

Furthermore, E , α , ρ , and T must likewise be discretized since their equations are dependent of r , where r is the integration's independent variable.

$$E = \sum_{j=1}^2 E_j^n \varphi_j^n \quad (4.20)$$

$$\alpha = \sum_{j=1}^2 \alpha_j^n \varphi_j^n \quad (4.21)$$

$$\rho = \sum_{j=1}^2 \rho_j^n \varphi_j^n \quad (4.22)$$

$$T = \sum_{j=1}^2 T_j^n \varphi_j^n \quad (4.23)$$

Chapter 4: Numerical Formulation

where

$$\varphi_1^n = \frac{r_{n+1} - r}{r_{n+1} - r_n} \quad (4.24)$$

$$\varphi_2^n = \frac{r - r_n}{r_{n+1} - r_n} \quad (4.25)$$

According to the Ritz Method, $w = \varphi_i$

Now, Eq. (4.16) yields when the Ritz Method is used with Eqs. (4.19) to (4.23),

$$\sum_{j=1}^2 K_{ij}^n F_j^n = \sum_{j=1}^2 L_{ij}^n \quad (4.26)$$

where

$i = 1, 2$

$$\begin{aligned} K_{ij}^n = & \int_{r_n}^{r_{n+1}} \frac{d\varphi_i^n}{dr} \frac{d\varphi_j^n}{dr} dr \\ & - \int_{r_n}^{r_{n+1}} \varphi_i^n \left(\frac{1}{r} - \frac{E_j^n \frac{d\varphi_j^n}{dr}}{E_j^n \varphi_j^n} \right) \frac{d\varphi_j^n}{dr} dr - \int_{r_n}^{r_{n+1}} \varphi_i^n \frac{1}{r} \left(\nu \frac{E_j^n \frac{d\varphi_j^n}{dr}}{E_j^n \varphi_j^n} - \frac{1}{r} \right) \varphi_j^n dr \end{aligned} \quad (4.27)$$

$$\begin{aligned} L_{ij}^n = & \int_{r_n}^{r_{n+1}} \varphi_i^n \left\{ \left(E_j^n \varphi_j^n \times \alpha_j^n \frac{d\varphi_j^n}{dr} \times T_j^n \varphi_j^n \right) + \left(E_j^n \varphi_j^n \times \alpha_j^n \varphi_j^n \times T_j^n \frac{d\varphi_j^n}{dr} \right) \right. \\ & \left. - \rho_j^n \varphi_j^n \omega^2 r \left(\frac{E_j^n \frac{d\varphi_j^n}{dr}}{E_j^n \varphi_j^n} r - \frac{\rho_j^n \frac{d\varphi_j^n}{dr}}{\rho_j^n \varphi_j^n} r - \nu - 3 \right) \right\} dr + \varphi_i^n(r_{n+1}) \frac{d\varphi_j^n}{dr}(r_{n+1}) \\ & - \varphi_i^n(r_n) \frac{d\varphi_j^n}{dr}(r_n) \end{aligned} \quad (4.28)$$

Chapter 4: Numerical Formulation

In the *RHS* of Eq. (4.26), all values of E_j^n , α_j^n , ρ_j^n , and T_j^n are known. As a result, if all values of the *RHS* of Eq. (4.26) are determined, the *RHS* is reduced to a vector L_i^n . Therefore, Eq. (4.26) may be simplified to,

$$\sum_{j=1}^2 K_{ij}^n F_j^n = L_i^n ; \quad i = 1,2 \quad (4.29)$$

Eq. (4.29) is a set of algebraic equations that, by meeting the continuity requirement $F_2^n = F_1^{n+1}$, may be combined to generate a global set of algebraic equations. The Gauss elimination method is then utilized for solving the global system of algebraic equations. The discrete values of F at the global node points are obtained by solving Eq. (4.29). The radial, circumferential, and von Mises stresses can then be calculated using Eqs. (3.24), (3.25), (3.29) and (3.33), respectively.

$$\sigma_r = \frac{1}{r} \sum_{j=1}^2 F_j^n \varphi_j^n \quad (4.30)$$

$$\sigma_\theta = \sum_{j=1}^2 F_j^n \frac{d\varphi_j^n}{dr} + \sum_{j=1}^2 \rho_j^n \varphi_j^n \omega^2 r^2 \quad (4.31)$$

$$u_r = \frac{r}{E_j^n \varphi_j^n} \sum_{j=1}^2 \left[F_j^n \frac{d\varphi_j^n}{dr} - \frac{\nu}{r} F_j^n \varphi_j^n \right] + \sum_{j=1}^2 \frac{\rho_j^n \varphi_j^n \omega^2 r^3}{E_j^n \varphi_j^n} + \alpha_j^n \varphi_j^n T_j^n \varphi_j^n r \quad (4.32)$$

$$\sigma' = \sqrt{\sigma_r^2 - \sigma_r \sigma_\theta + \sigma_\theta^2} \quad (4.33)$$

It is worth noting that, depending on the values of volume fraction of the materials A and B throughout the disk, the current finite element model may be used for a Functionally Graded Material (FGM) as well as a homogeneous circular rotating disk.

4.2 Optimization Model

4.2.1 Inverse Method

An inverse problem is a special kind of problem in which, instead of having a prescribed material distribution, the material distribution is instead calculated according to the objective function. The output of the problem is controlled by the objective function. In addition, the optimization model for inverse problem allows for both the minimization and maximizing of the objective function. If the minimum stress profile throughout an object is intended, then the objective function must be set accordingly. Next, the optimization model will minimize the objective function and deliver the material distribution that corresponds to the objective function's global minimum value. Likewise, if the material distribution corresponding to the prescribed stress field is required, optimization can also provide the material distribution as output if the objective function is properly set.

Once the values of volume fractions at each node V_A^i ($i = 1, n$) are specified, the corresponding values of bulk modulus K and shear modulus G are derived from *Eqs. (3.1) to (3.4)* and used in *Eqs. (3.5) and (3.6)* to calculate the values of Young's Modulus E and Coefficient of Thermal Expansion α , respectively, at each nodal point. Here n is the number of nodal points and V_A is volume fraction of constituent "A". Moreover, utilizing *Eq. (3.8)* allows for the calculation of the density ρ as well as the thermal conductivity k of the FGM disk according to the designated volume fraction at each nodal point. For the temperature profile of the FGM disk, the temperatures at the inner and outer surfaces of the FGM disk are determined by the boundary conditions, and the temperatures that lie in between the inner and outer surfaces are estimated with the help of *Eqs. (3.7) and (3.10) to (3.15)*. The details of the optimization model's solution procedure are now provided below.

4.2.1.1 Differential Evolution

The objective function is minimized using a method called differential evolution [109,110], which is employed in the optimization model of the present work. Differential evolution is an efficient approach to minimizing the value of a function [111]. In this method, the algorithm keeps track of a population of m vectors, $\{x_1, x_2, x_3, \dots, x_j, \dots, x_m\}$ where $m \gg n$, while n is the total number of nodal points or variables. Each vector contains the values of n number of variables, where all the values are assigned randomly. A new population having m vectors is produced at the beginning of the algorithm, which is called initialization. The next step is mutation. In mutation, j^{th} new point is formed by selecting three random vectors, x_1, x_2 , and x_3 from the population and generating the equation $x_j^M = x_1 + S(x_2 - x_3)$, where S is a real scaling factor. Here, x_j^M is the mutant vector, and the values of j vary from 1 to m . Then, a new vector x_{new} is generated from x_j^P and x_j^M by selecting the i^{th} coordinate from x_j^M with a probability of 50% and otherwise selecting the coordinate from x_j^P , where x_j^P is the parent vector which is chosen randomly from the population, and the values of i vary from 1 to n . This step is called recombination and x_{new} is the offspring vector. In the selection step, when $f(x_{new}) < f(x_j^P)$, then x_{new} will take the place of x_j^P in the next generation population, otherwise x_j^P will remain unchanged in the next generation population. Here, f is the objective function.

The differential evolution method is difficult to implement computationally, but it is generally durable and has a tendency to perform well for situations that contain a number of local minima and the differential evolution approach guarantees a global minimum.

The flow diagram of initialization, mutation, recombination and selection steps of the differential evolution method is mentioned in Fig. 4.3. The steps involved in the differential evolution algorithm continue to run until the global minimum value of the objective function is obtained. The elaborate flow diagram of the differential evolution method is demonstrated in Fig. 4.4.

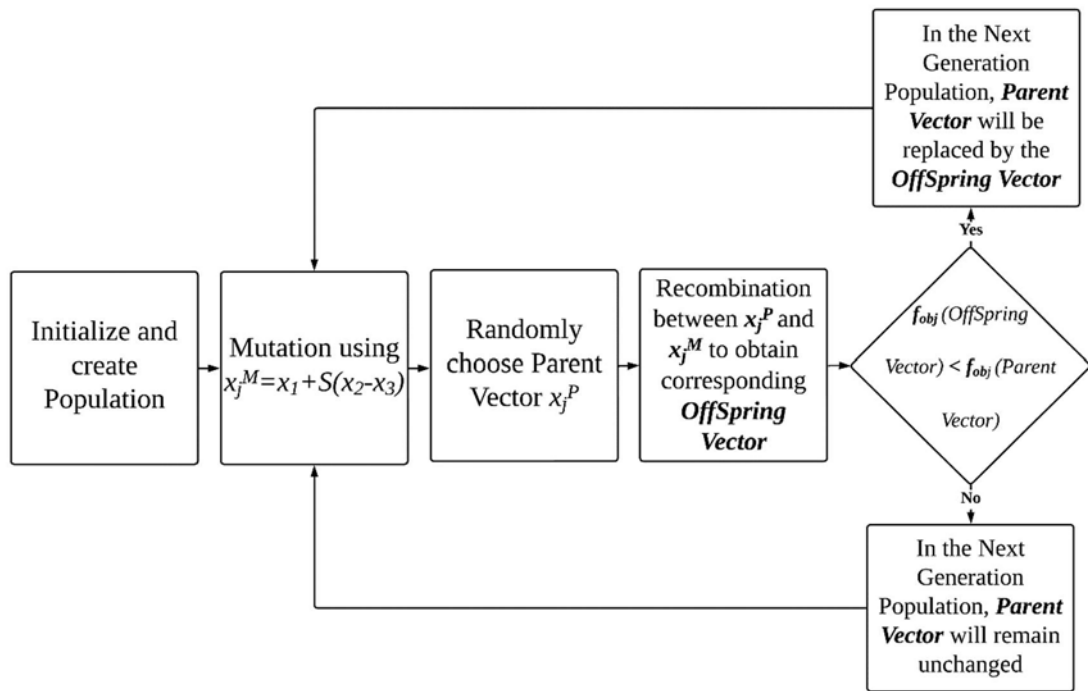


Fig. 4.3: Flow diagram of initialization, mutation, recombination and selection steps of the differential evolution algorithm.

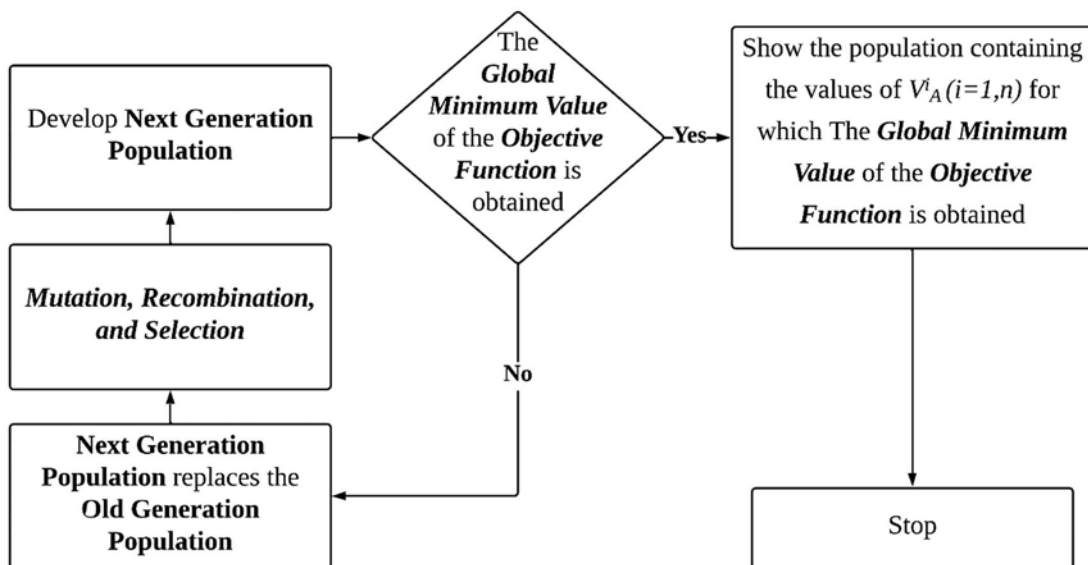


Fig. 4.4: Flow diagram of the Differential Evolution algorithm.

The entire process of the differential evolution method for the present study is described in detail in Figs. 4.5 and 4.6 for different objective functions.

4.2.1.2 Optimization Model for Minimum Stress

The objective function is defined by,

$$f_{obj}(V_A^i, i = 1, 2, \dots, n) = \sum_{i=1}^n \sigma_i^2$$

Here $\sigma_i (i = 1, n)$ is any kind of stress at each nodal point of the FGM disk and n is the number of nodes. The von Mises stress is the basis for the minimum stress profile across the FGM disk since the value of the von Mises stress determines whether or not the disk will yield or fail. The Differential Evolution Method is used to minimize the objective function, and the corresponding material distribution is achieved for the global minimum value of the objective function. The entire procedure is demonstrated in Fig. 4.5.

4.2.1.3 Optimization Model for Prescribed Stress

This section makes use of the same mathematical model as the previous one; the only difference is that the objective function has been modified in order to obtain a new output that is matched to the objective of this study.

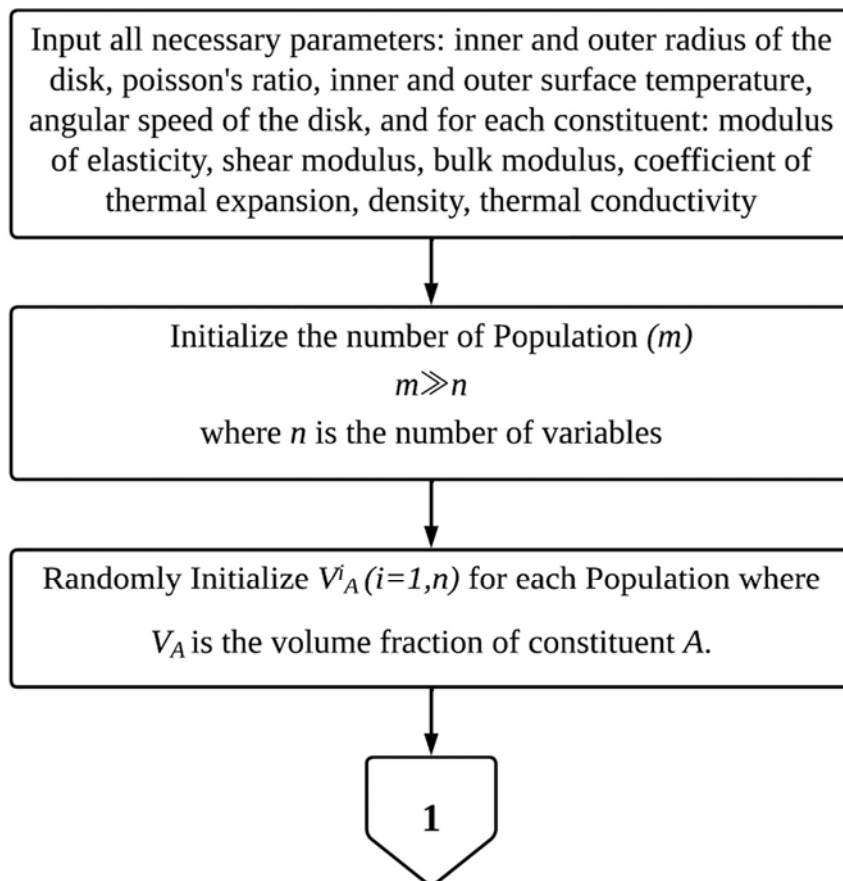
The objective function is defined by,

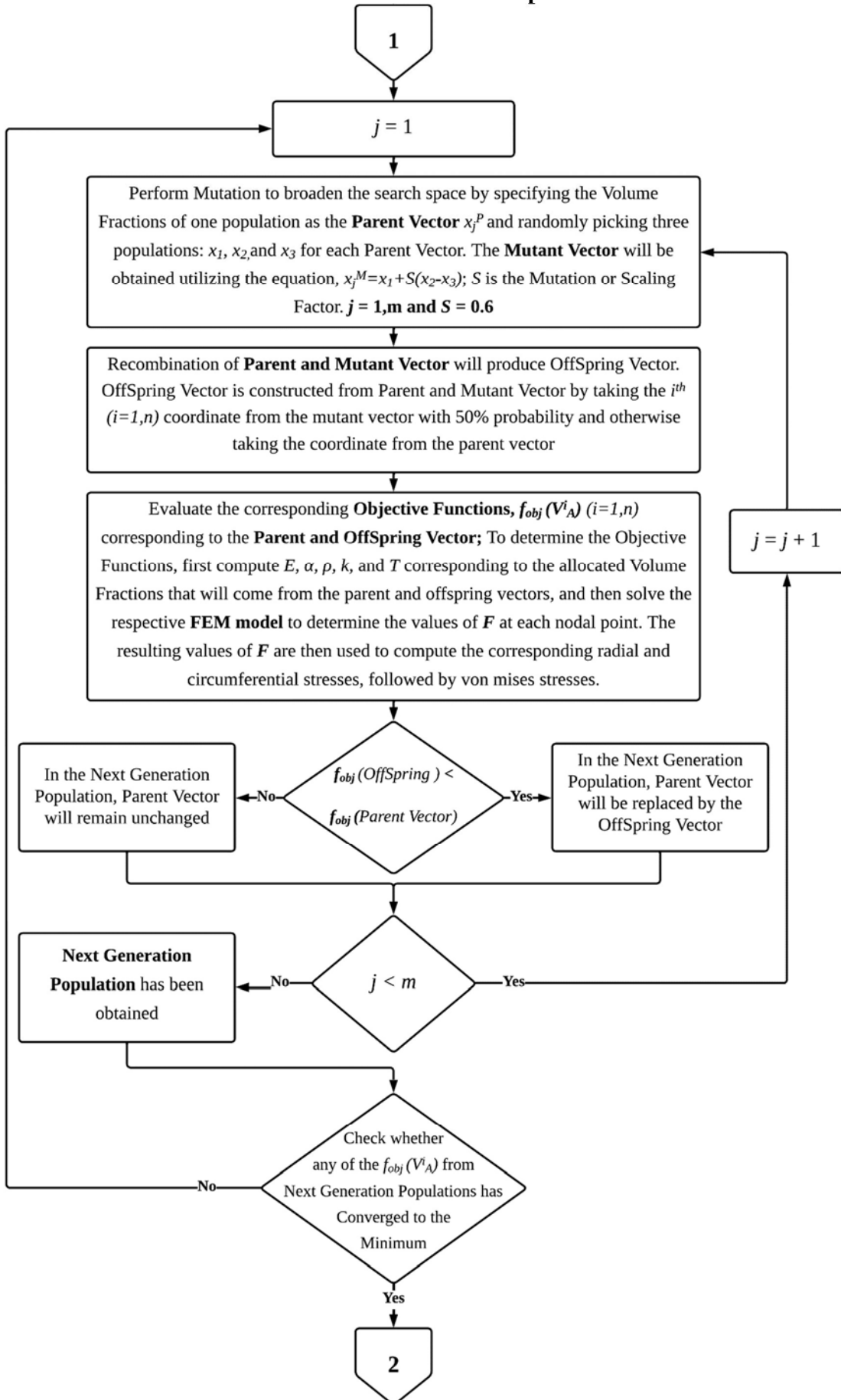
$$f_{obj}(V_A^i, i = 1, 2, \dots, n) = \sqrt{\sum_{i=1}^n \frac{(\sigma_i - \sigma_i^p)^2}{\sigma_i^2}}$$

Here $\sigma_i (i = 1, n)$ and $\sigma_i^p (i = 1, n)$ are calculated and prescribed stresses, respectively and the stress may be radial, circumferential, von Mises, or any other kind of stress. In addition, n is the number of nodes in the FGM disk. The objective function is minimized by utilizing the Differential Evolution Method, and the corresponding material distribution is attained for the objective function's global minimum value. A tolerance ϵ needs to be chosen for this model in order to achieve the purpose of predicting the prescribed stress. The value of ϵ is assumed as 0.1 for the present study. If the value of the objective function is less than or equal to ϵ , the model will output the optimum material distribution; otherwise, the model will

Chapter 4: Numerical Formulation

specify that the prescribed stress profile cannot be predicted. Fig. 4.6 illustrates an elaborate representation of the complete process.





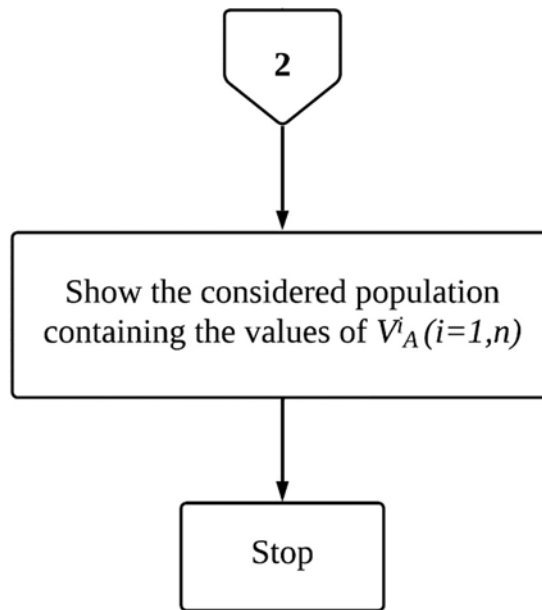
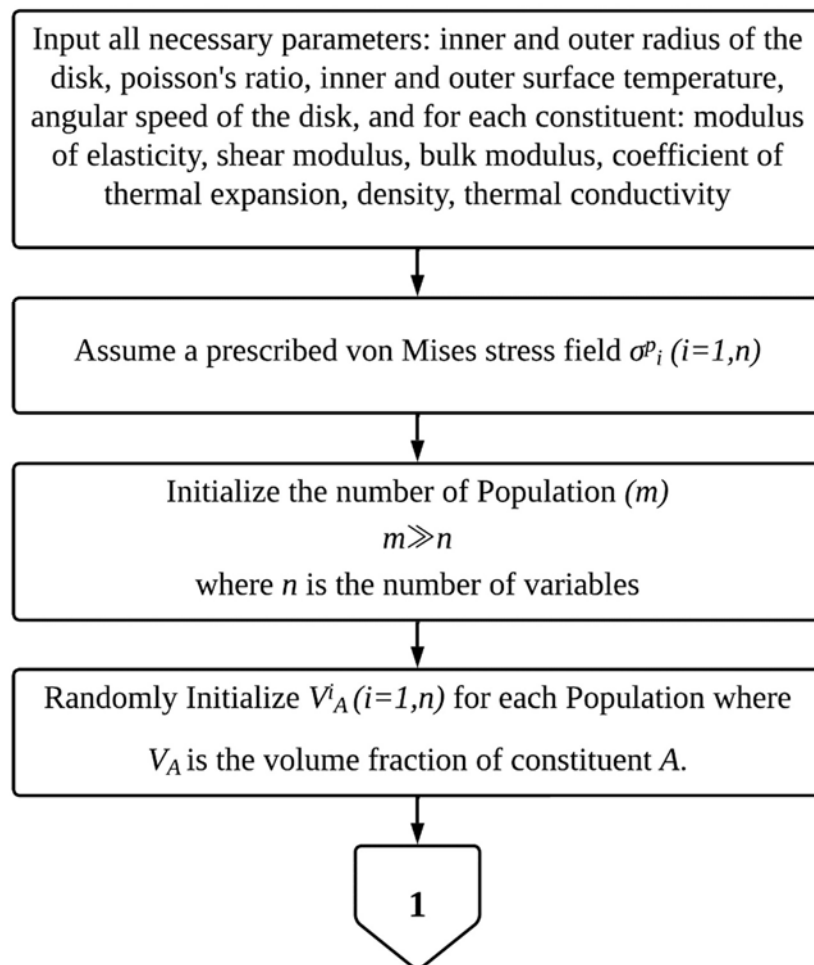
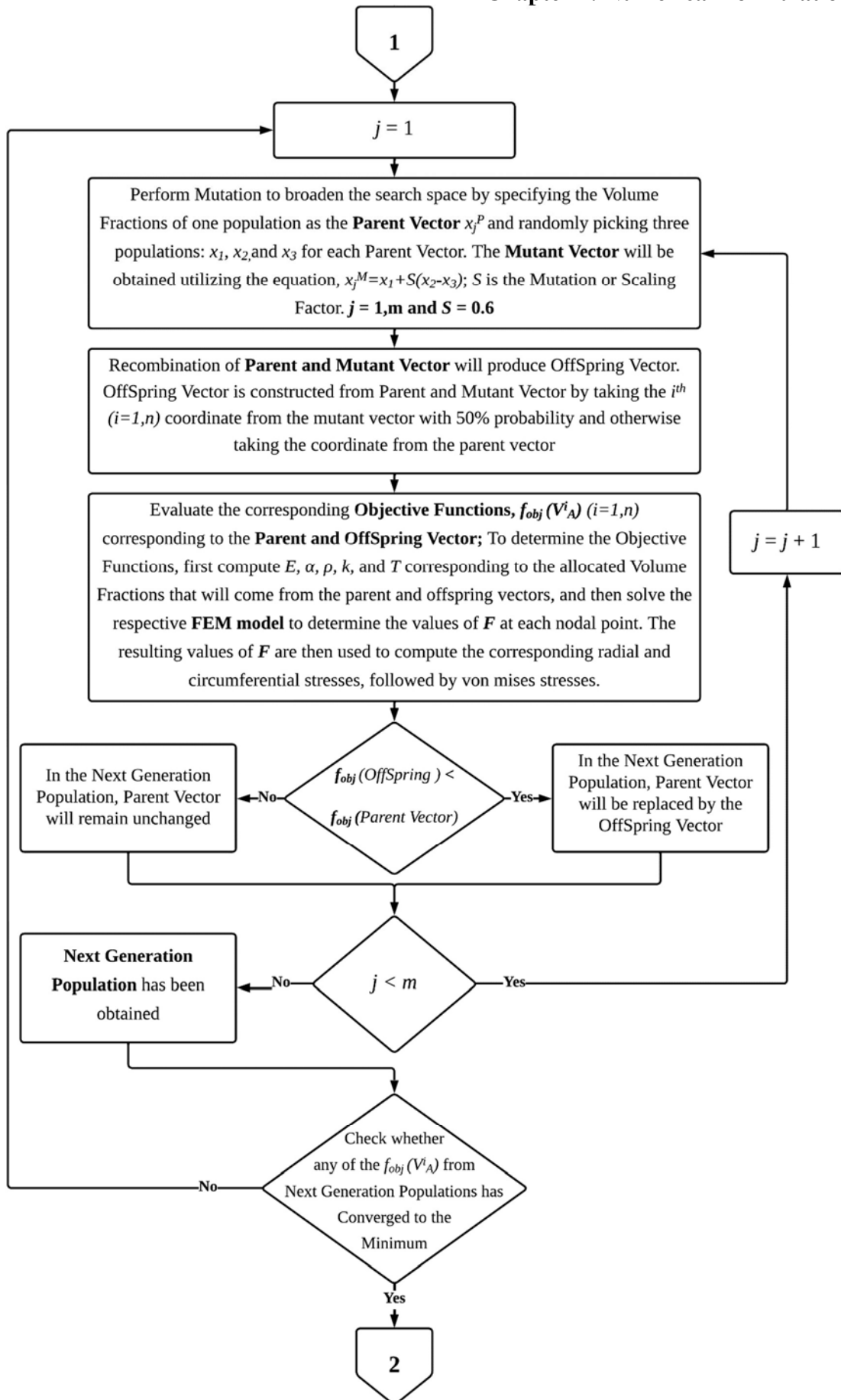


Fig. 4.5: Flowchart for optimization model to realize the minimum stress throughout the FGM disk.





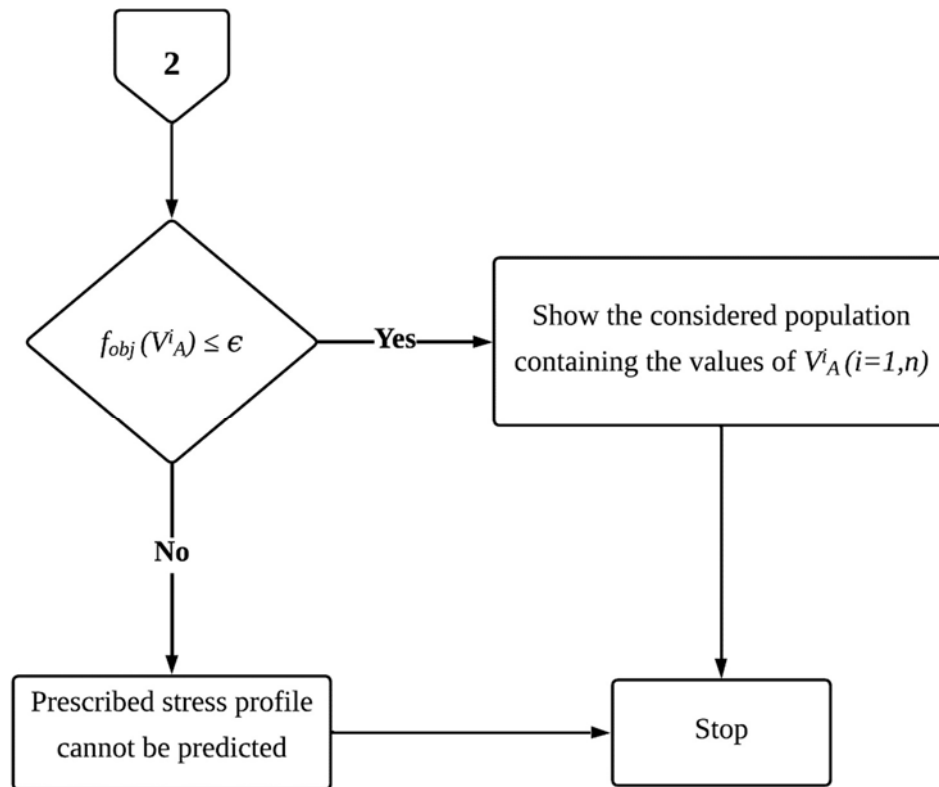


Fig. 4.6: Flowchart for optimization model to realize the prescribed stress profile across the FGM disk.

4.2.2 Direct Method

The direct method is the most well-known approach for calculating the required results for a specified material distribution. Any material distribution can be employed in the direct model of present work to evaluate the corresponding stresses, strains, and displacements. However, the material distribution obtained from the optimization model is considered as prescribed material distribution in the current study to compute corresponding stresses and also the radial displacement when needed. The entire procedure is demonstrated in Fig. 4.7.

Chapter 4: Numerical Formulation

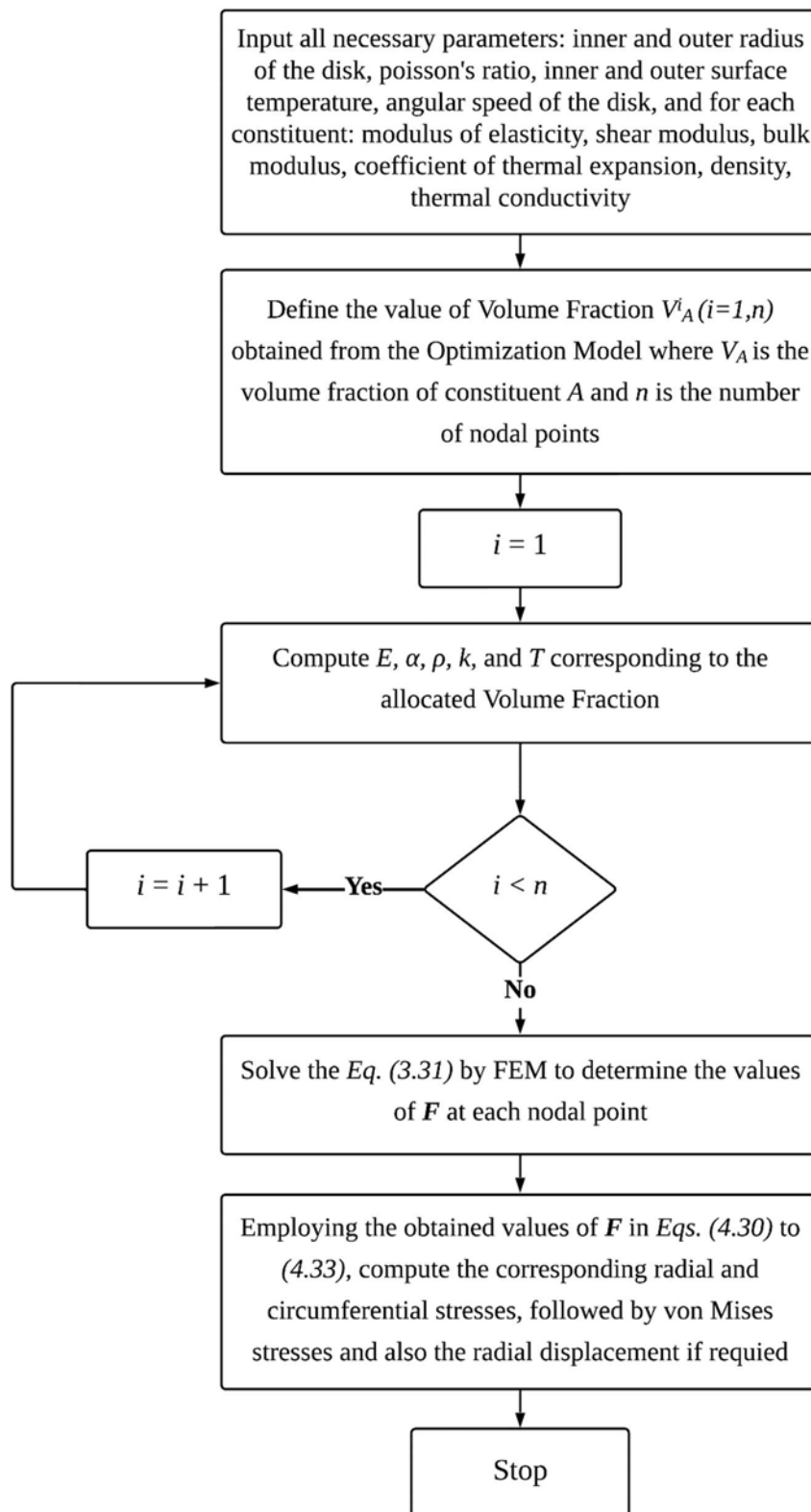


Fig. 4.7: Flowchart for direct problem to determine von Mises, radial and circumferential stresses, and radial displacement throughout the FGM disk.

CHAPTER 5

RESULTS AND DISCUSSION

The numerical model of inverse and direct problems developed in the present study can be used for any materials A and B . However, Al and Al_2O_3 are used in the present work for materials A and B , respectively, to demonstrate the models since Al_2O_3 has excellent cutting and grinding characteristics. In fact, depending on the design requirements, the symbols A and B employed in the theoretical models might be any materials. Table 5.1 summarizes the mechanical and thermal characteristics of these constituent materials. Poisson's ratio of Al_2O_3 is approximately 0.26, and for Al, it varies from 0.31 to 0.34. Therefore, Poisson's ratio of the Al/ Al_2O_3 FGM disk must be between 0.26 and 0.34. Within this range, the Poisson's ratio is taken as 0.3, and it is kept constant throughout the disk.

Table 5.1: Mechanical and thermal properties of Al and Al_2O_3				
Type	Materials	Properties		
		Young's Modulus (GPa)	Coefficient of thermal expansion (/°C)	Density (g/cm^3)
A	Al	71	23.1×10^{-6}	2.70
B	Al_2O_3	380	8.0×10^{-6}	0.96

Chapter 5: Results and Discussion

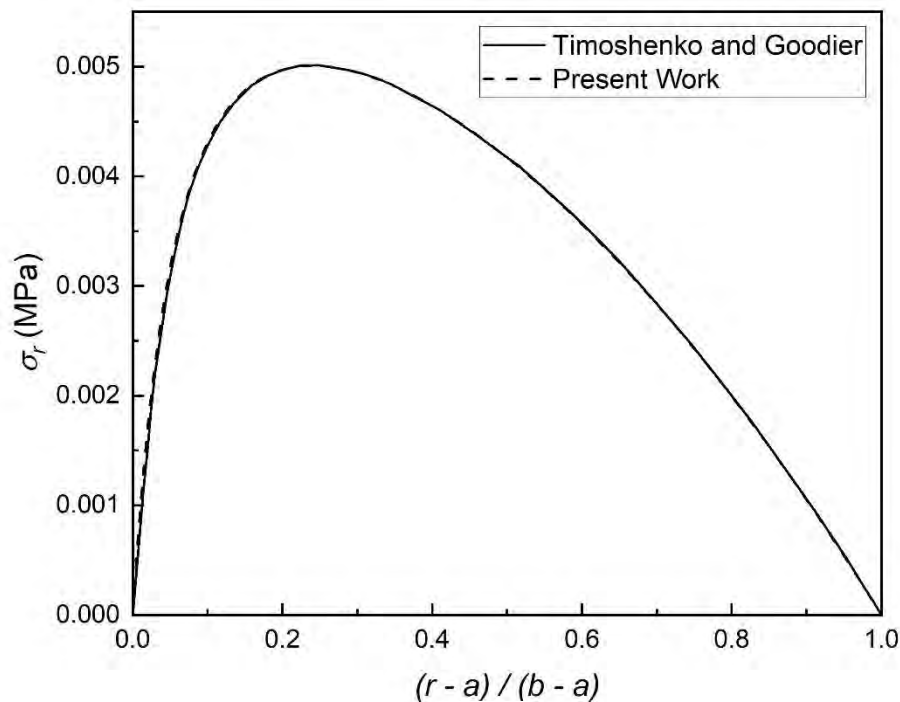
Mathematica software running on a computer with 16 Gigabytes (GB) of Random Access Memory (RAM) is used to solve both the inverse problem and the direct problem that is involved with this study. *Mathematica* is the software that needs precise codes to be written in *Wolfram Language* in order to solve the respective problems. For the current study, two Wolfram Language codes are constructed to solve the inverse problem and the direct problem, respectively, for which flow charts are demonstrated in Figs. 4.5 to 4.7. In this chapter, all results derived from *Wolfram Language* code using *Mathematica* software are presented graphically and discussed elaborately.

5.1 Validation of the Finite Element Model

The present work is validated by applying the finite element model to three distinct instances and comparing the determined results to the solutions found by Timoshenko and Goodier [69], Sadd [70], and Madan *et al.* [71], respectively. The validated finite element model is subsequently employed in the mathematical model of inverse problem.

5.1.1 Comparison with Timoshenko and Goodier

The current finite element model is applied to the situation of a simple homogeneous isotropic disk of *Al* to determine the components of stress due to rotation only, without considering any thermal load, and the results are compared with the analytical solution given by Timoshenko and Goodier [69]. It should be noted that the current finite element model can be applied to a homogeneous disk under rotation if the volume fraction of any constituent is set to one, and *Al* is such constituent in this case. In addition, ε^* is set to zero to ignore the thermal load. Fig. 5.1 shows a comparison of the stress components for $b/a = 10$ and angular speed $N = 150$ rpm, where perfect agreement between the current work and Timoshenko and Goodier [69] has been found.



(a)

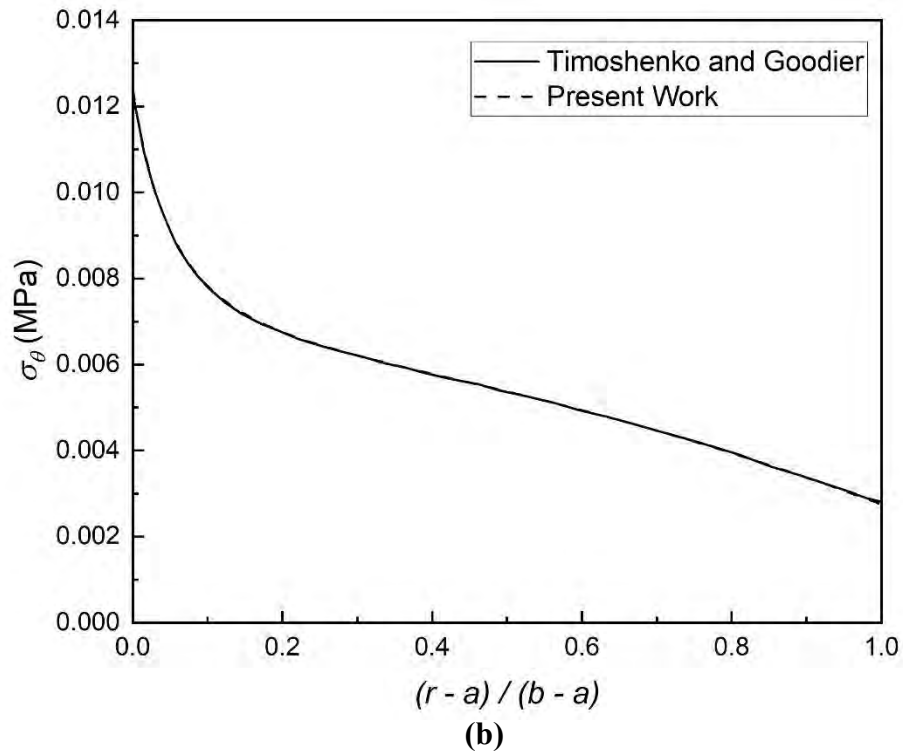


Fig. 5.1: Comparison of (a) radial stress and (b) circumferential stress with Timoshenko and Goodier [69] in a homogeneous circular disk under rotation only.

5.1.2 Comparison with Sadd

The current finite element model is applied to a homogeneous steel plate that is subjected to thermal load only when the temperatures at the plate's inner and outer surfaces are 100°C and 0°C, respectively. The modulus of elasticity of steel is taken as 200 GPa and the coefficient of thermal expansion as $8.0 \times 10^{-6} / ^\circ\text{C}$. The comparison of the stress components corresponding to $b/a = 3$ and the angular speed $N = 0$ rpm are presented in Fig. 5.2. It is observed that the results accord well within the acceptable range.

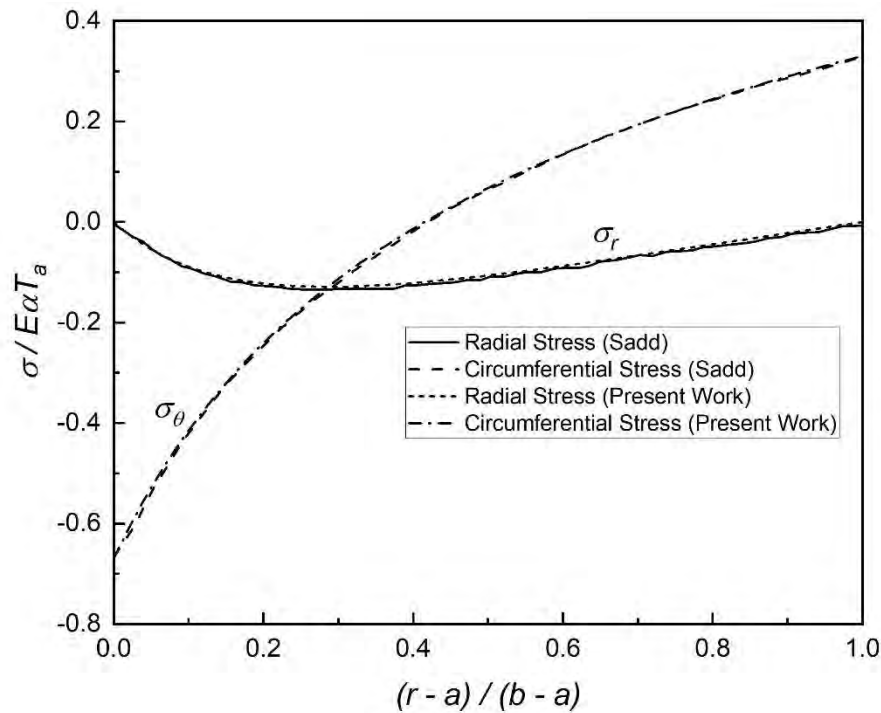


Fig. 5.2: Comparison of radial and circumferential stress with Sadd [70] in a homogeneous circular plate under thermal load only.

5.1.3 Comparison with Madan *et al.*

In order to assess the model's feasibility for dealing with functionally graded material (FGM) disks, it is applied in the context of an FGM disk of aluminum and silicon carbide to determine the radial, circumferential, and von Mises stresses owing to rotation alone, without taking into consideration any thermal load. In this case, aluminum and silicon carbide are used as metal and ceramic, respectively, and the material distribution across the FGM disk is assumed to be linear. Furthermore, the mass density of pure metal and pure ceramic is 2643 and 2130 kg/m³, respectively, while the modulus of elasticity is 67 and 302 GPa, respectively. The computed radial, circumferential, and von Mises stresses are compared to those found by Madan *et al.* [71]. Fig. 5.3(a) and 5.3(b) illustrate the comparison of the radial, circumferential, and von Mises stresses for $b/a = 10$ and $b/a = 20$, respectively. The results obtained from the present work agree well within the permissible limit with Madan *et al.* [71], as shown in Fig. 5.3(a) and 5.3(b), with the largest difference being just 0.53%.

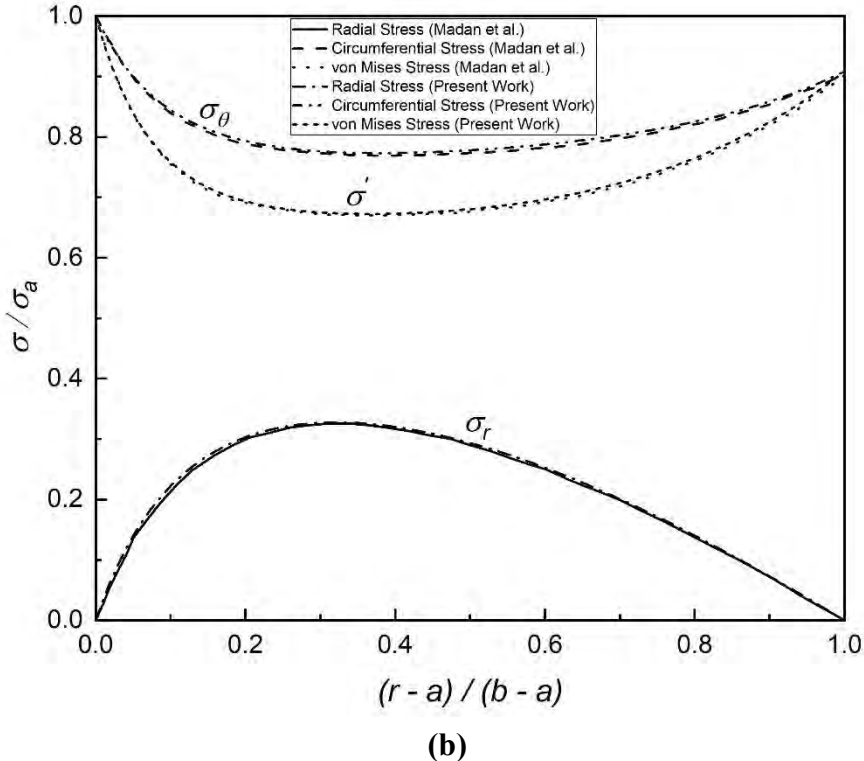
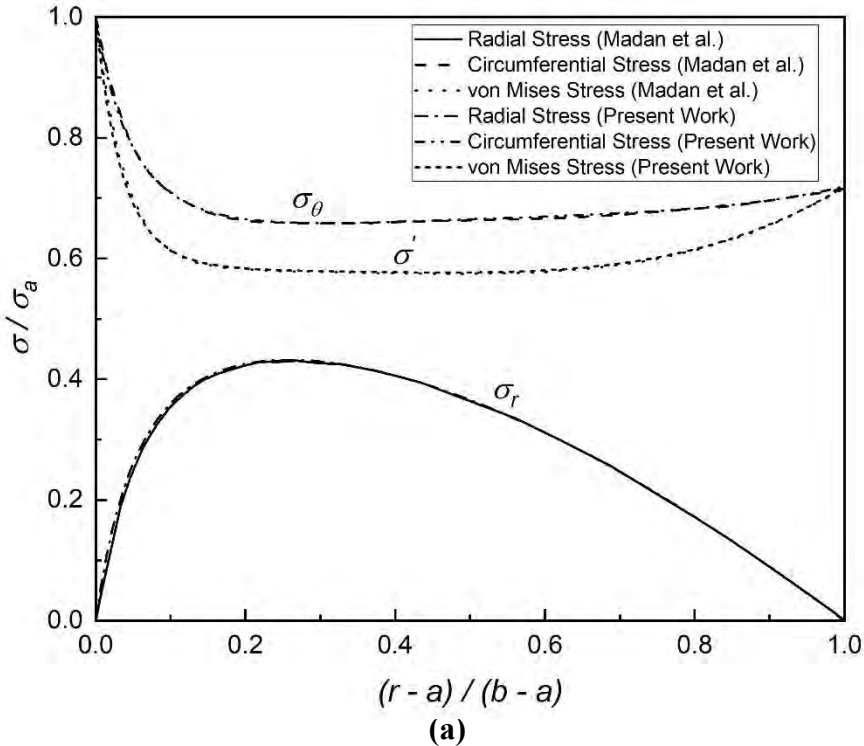


Fig. 5.3: Comparison of radial, circumferential, and von Mises stresses in a rotating FGM circular disk corresponding to (a) $b/a = 10$ and (b) $b/a = 5$ with Madan *et al.* [71].

5.2 Validation of the Optimization Model

The FEM model was used to develop an optimization model in which the objective function is responsible for the output. The objective function $f_{obj}(V_A^i)$ is simply selected as $\sum_{i=1}^n \sigma_i^2$ for obtaining the minimum stress throughout the FGM disk, and the model is presented in Fig. 4.5. Likewise, for estimating required or prescribed stress across the FGM disk, objective function $f_{obj}(V_A^i)$ is defined as,

$\sqrt{\sum_{i=1}^n \frac{(\sigma_i - \sigma_i^p)^2}{\sigma_i^2}}$, and the model is illustrated in Fig. 4.6. Here σ and σ^p are calculated

and prescribed von Mises stress, respectively. Both optimization models are identical in the sense that the objective function may be modified to produce the intended outcome. To verify this optimization model, the von Mises stresses in a rotating FGM disk determined by *Madan et al.* [71] were adopted and assumed as the prescribed stress profile across the FGM disk. The FGM disk corresponds to $b/a = 5$, and additional discussions for the disk are stated in the preceding section. The optimization model is then used to realize the material distribution over the FGM

disk corresponding to the prescribed stress profile utilizing $\sqrt{\sum_{i=1}^n \frac{(\sigma_i - \sigma_i^p)^2}{\sigma_i^2}}$ as the objective function, and the value of the objective function is obtained as 0.001. In Fig. 5.4, the calculated material distribution across the FGM disk using the present work's optimization model is compared to the assumed material distribution of *Madan et al.* [71]. Fig. 5.4 demonstrates excellent agreement within the acceptable limit. Therefore, the computed material distribution derived by the optimization model of the present work is almost the same as the assumed material distribution of *Madan et al.* [71]. Finally, by using a direct problem, the calculated material distribution was utilized to compute the von Mises stress across the FGM disk. Fig. 4.7 depicts a direct problem. The obtained results agree well within the allowable range with *Madan et al.* [71], as illustrated in Fig. 5.5.

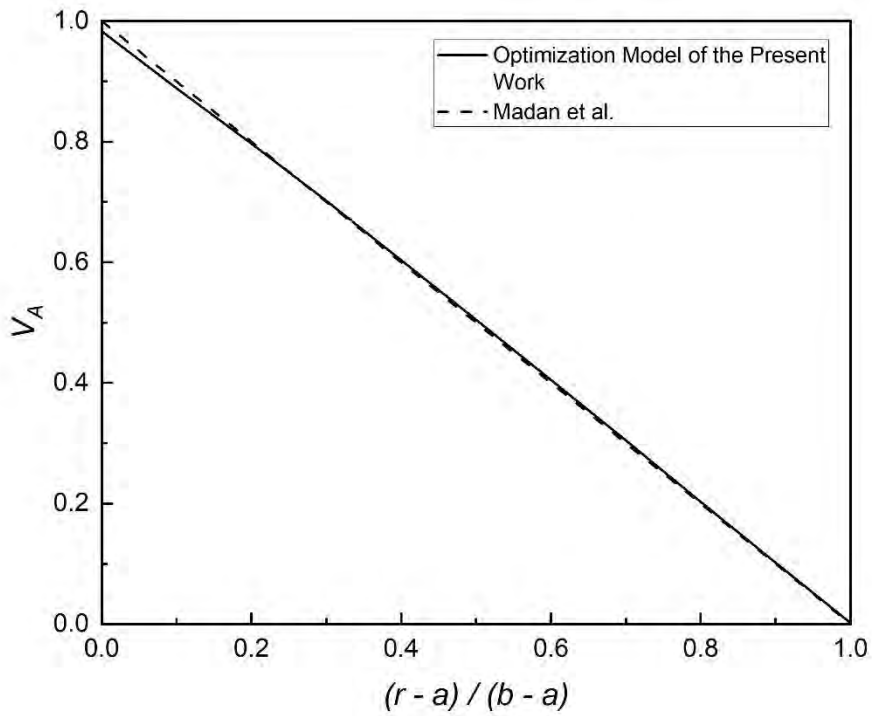


Fig. 5.4: Comparison of material distribution in a rotating FGM circular disk corresponding to $b/a = 5$ with Madan *et al.* [71].

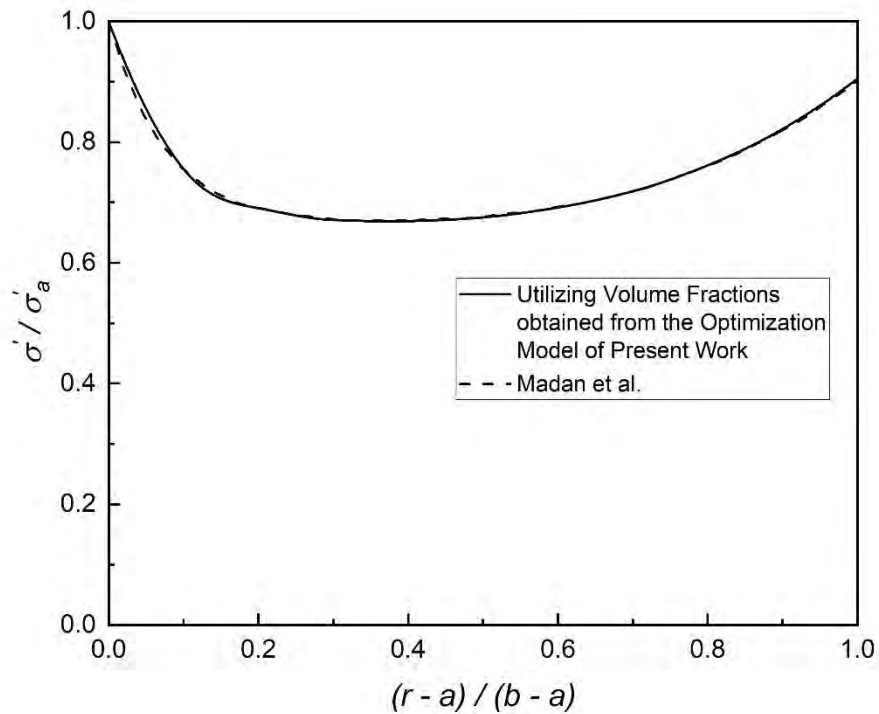


Fig. 5.5: Comparison of von Mises stress in a rotating FGM circular disk corresponding to $b/a = 5$ with Madan *et al.* [71].

Chapter 5: Results and Discussion

The disks have only meshed in the radial direction with uniform distribution and equal size of the elements since all of the characteristics of interest are only functions of the radial distance of the disk. The length of each element must be specified for both finite element models, one of which will be used in the Inverse Problem Optimization Problem and another in the Direct Problem. In this situation, the optimization model uses the Differential Evolution Method to run a large number of iterations in order to find the global minimum value of the specified objective function. Until the global minimum is established, all data pertaining to iterations is stored in RAM. Therefore, the calculation is computationally extremely expensive and requires a large amount of RAM on a computer. As a result, the smallest allowable element size for a finite element model used in the optimization model on a machine with 16 GB of RAM becomes 5 mm for an FGM disk with $b/a = 5$. Nevertheless, if the optimization model has to go through 1000 iterations in order to compute the global minimum of the respective objective function, then it will need the amount of RAM memory that is equivalent to having an element that is 0.005 mm in size. Moreover, if the number of elements is taken into account, then for $b = 100$, the number of elements is 16, but after 1000 iterations, the optimization model will consume the RAM space equivalent to the number of elements of 16000. Even after one thousand iterations, the result of the optimization model for inverse problem may not appear. Therefore, a large number of iterations, generally much more than 1000, are frequently required to minimize the objective function and produce the result. Because of these incredibly mathematically expensive calculations, the optimization model takes about half a day to provide an output.

Nonetheless, such optimization model is able to produce results with the highest possible level of accuracy since the model has been validated perfectly in Section 5.2. Furthermore, in Section 5.2, validation is carried out using the same Optimization model as mentioned above, which demonstrates that the calculated material distribution model is in perfect agreement with the assumed material distribution that Madan *et al.* [71] presented. Thus, the optimization model of the present work is capable of giving results with perfect precision.

Chapter 5: Results and Discussion

However, in the case of the Direct Problem, since the results are obtained after just one iteration, there is no restriction on either the minimum length or the number of elements involved in the finite element model. Therefore, in order to solve the finite element model, the mathematical model for the direct problem developed in the present work can be used with any length or number of elements. Because radial and circumferential stresses are estimated from the parameter F , the convergence test for F is performed by solving a direct problem. F has been calculated through a direct problem in which the prescribed material distribution is the material distribution corresponding to the minimum stress profile across the FGM disk of $b/a = 5$, implementing the first boundary condition. In addition, the optimization model developed in this study yields the material distribution corresponding to the minimal stress profile over the FGM disk. The von Mises stress is the basis for the minimum stress profile across the FGM disk since the value of the von Mises stress determines whether or not the disk will yield or fail. It should be noted that the von Mises stress is derived from the radial and circumferential stresses, and it is apparent that the convergence of F assures the convergence of the von Mises stress.

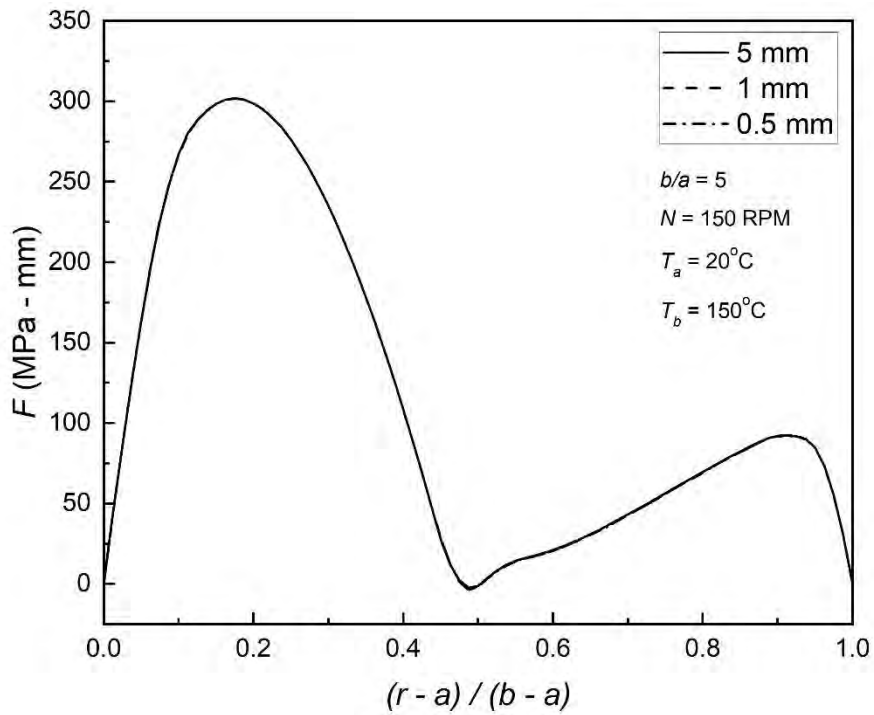


Fig. 5.6: The influence of element size on the parameter F .

The convergence criterion of F is shown in Fig. 5.6 throughout the full radial thickness of the disk, and it is obvious from Fig. 5.6 that the value of F is identical for all element sizes. Nevertheless, all of the data reported in this chapter relate to an element size of 0.5 mm, which was selected to guarantee greater accuracy of the analyses.

5.3 Evaluation of Optimum Material Distribution Corresponding to Minimum Stress

5.3.1 Boundary Condition: Case I

For the inverse problem of determining the minimum stress profile with the first boundary condition, an FGM disk with $b/a = 5$ was investigated. Material distribution is calculated for determining minimum von Mises stress because the yielding or failing of the material is based on the value of the von Mises stress. The FGM disk is configured to rotate at 150 RPM and has an inner surface temperature of 20°C. The material distribution is determined for three different outer surface temperatures, namely 100°C, 200°C, and 300°C and presented in Fig. 5.7. Usually, high temperature is induced at the outer surface of circular cutters or grinding disks; therefore, different values of high temperature are assumed as the outer surface temperature of the FGM disk to analyze the corresponding optimum material distributions.

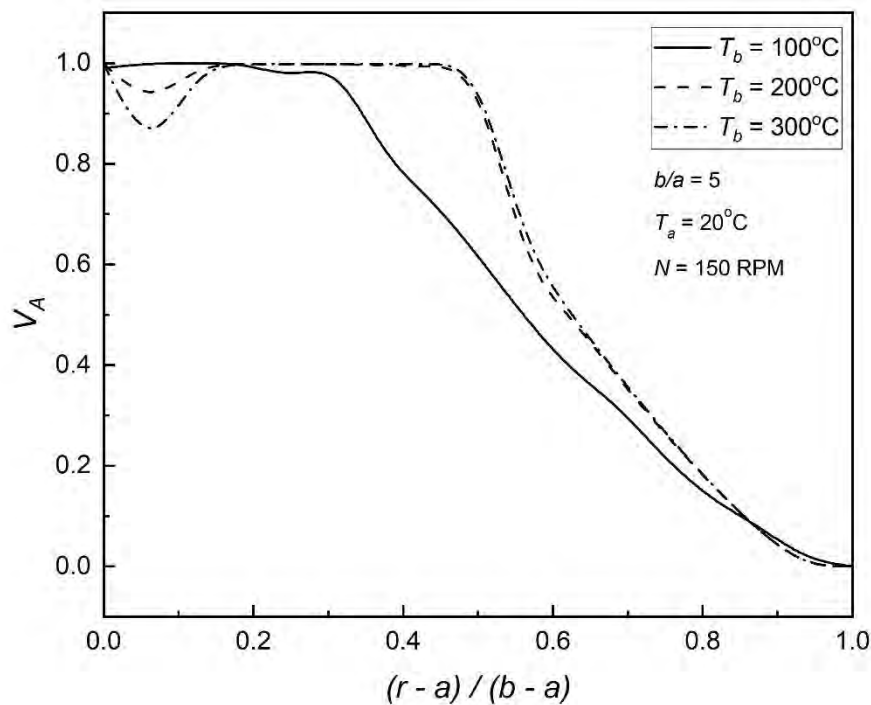


Fig. 5.7: Effect of outer surface temperature on optimum material distribution of an FGM disk under Boundary Condition I.

Chapter 5: Results and Discussion

According to Fig. 5.7, the volume fraction of Al at the inner surface of the FGM disk is nearly 100%. For 100°C inner surface temperature, Al gradually approaches 100%, and from near normalized radius $(r - a)/(b - a) = 0.2$, it begins to reduce where the reduction rate is modest up to around $(r - a)/(b - a) = 0.3$ and then begins to decrease nonlinearly to 0% at the outer surface. On the other hand, the nonlinear decrease begins at about $(r - a)/(b - a) = 0.47$ for 200°C and 300°C. In addition, around the inner area, the volume fraction of Al drops to nearly 95% for 200°C and near 86% for 300°C before returning to 100% near $(r - a)/(b - a) = 0.2$. The optimum material distributions suddenly decrease and then again increase near the inner surface of the disk, as seen in Fig. 5.7. It occurs because of the boundary condition of the inner surface of the disk. Moreover, the outer surface temperature and temperature differences between the inner and outer surfaces of the disk also have an impact on the optimum material distribution of the disk. The von Mises stress, radial stress, and circumferential stress corresponding to the material distributions are depicted in Figs. 5.8, 5.9, and 5.10.

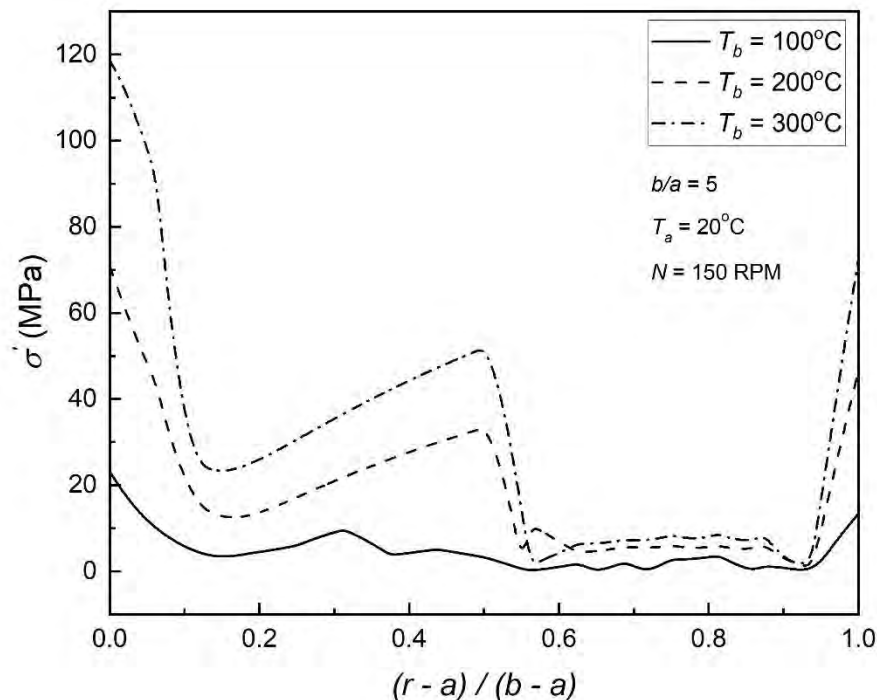


Fig. 5.8: Effect of outer surface temperature on the minimum von Mises stress corresponding to optimum material distribution of an FGM disk under Boundary Condition I.

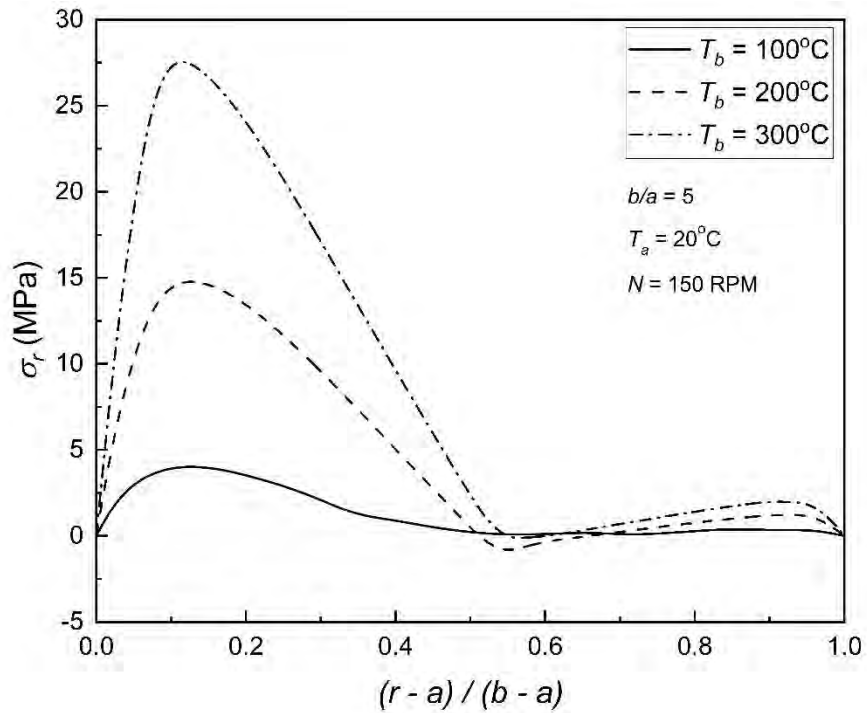


Fig. 5.9: Effect of outer surface temperature on the radial stress corresponding to minimum von Mises stress and optimum material distribution of an FGM disk under Boundary Condition I.

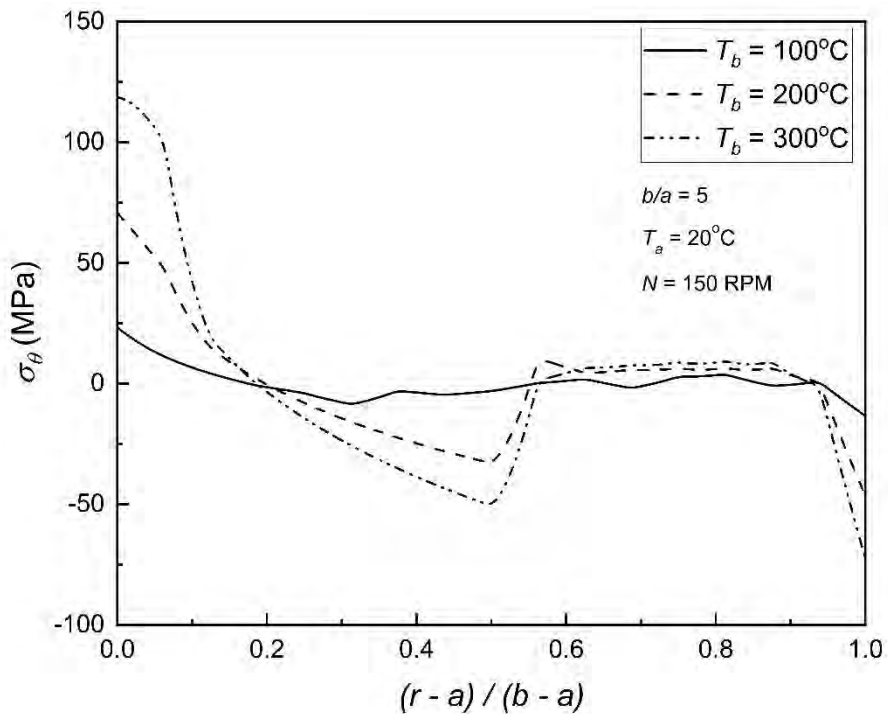


Fig. 5.10: Effect of outer surface temperature on the circumferential stress corresponding to minimum von Mises stress and optimum material distribution of an FGM disk under Boundary Condition I.

Chapter 5: Results and Discussion

For 300°C outer surface temperature, the peak value of von Mises stress is observed to be slightly less than 120 MPa, as shown in Fig. 5.8. The yield stress of Al is 276 MPa, while that of Alumina is 15.4 GPa. Thus, the FGM disk will begin to yield if the von Mises stress is at or above 276 MPa at any point throughout the FGM disk. Therefore, even though the temperature difference between two surfaces is large, the inverse problem revealed a material distribution that could greatly reduce the developed stress, which may be characterized as the minimal stress profile.

Further inspection of Fig. 5.8 reveals that the von Mises stresses corresponding to the normalized radius of 0.15 to 0.56 are considerably less than 60 MPa and 40 MPa for outer surface temperatures of 200°C and 300°C, respectively. The stress may be stated to be insignificant across the FGM disk, having 100°C outer surface temperature when compared to others because of the lower temperature difference between the inner and outer surfaces of the disk. Moreover, von Mises stresses become minimum at the normalized radius of 0.56 to 0.94, and the lowest values are obtained in this area. Finally, von Mises stresses grow towards the outer surface but remain below 80 MPa. Fig. 5.9 demonstrates that the radial stresses satisfy the boundary condition, and at the normalized radius of 0.5 to 0.6, radial stress becomes compressive for 200°C and 300°C, but otherwise stays tensile across the FGM disk at all temperatures. Circumferential stress in the FGM disks depicted in Fig. 5.10 remains tensile across the inner area and compressive towards the outer region. Over the remaining portion of the disk, circumferential stress initially becomes compressive, then tensile. However, except for the inner and outer regions, the FGM disk with 100°C outer surface temperature develops nearly zero circumferential stress.

Chapter 5: Results and Discussion

To observe the effect of variation of inner surface temperature, the temperature of the FGM disk's outer surface is kept constant at 150°C, while the temperature of the inner surface is assumed to be 0°C, 50°C, 75°C, and 100°C. Four different temperatures are assumed at the inner surface of the disk because, depending on the operating conditions, the inner surface of the circular cutter or grinding disk might be at a lower or higher temperature. The calculated material distributions for the minimum von Mises stress profiles obtained by utilizing the optimization model of the current study are shown graphically in Fig. 5.11. The inner surface is seen to be 100% Al, while the outer surface is 100% Alumina for 0°C and 50°C inner surface temperatures. In addition, the volume fraction of Al at the inner surface of the FGM disk begins to decrease as the inner surface temperature rises while it rises at the outer surface. Volume fractions fall smoothly and nonlinearly from the inner to the outer surface, with the exception of the disk with 0°C inner surface temperature, where it declines to almost 80% and then increases to 100%, being Al dominating until the normalized radius of 0.58.

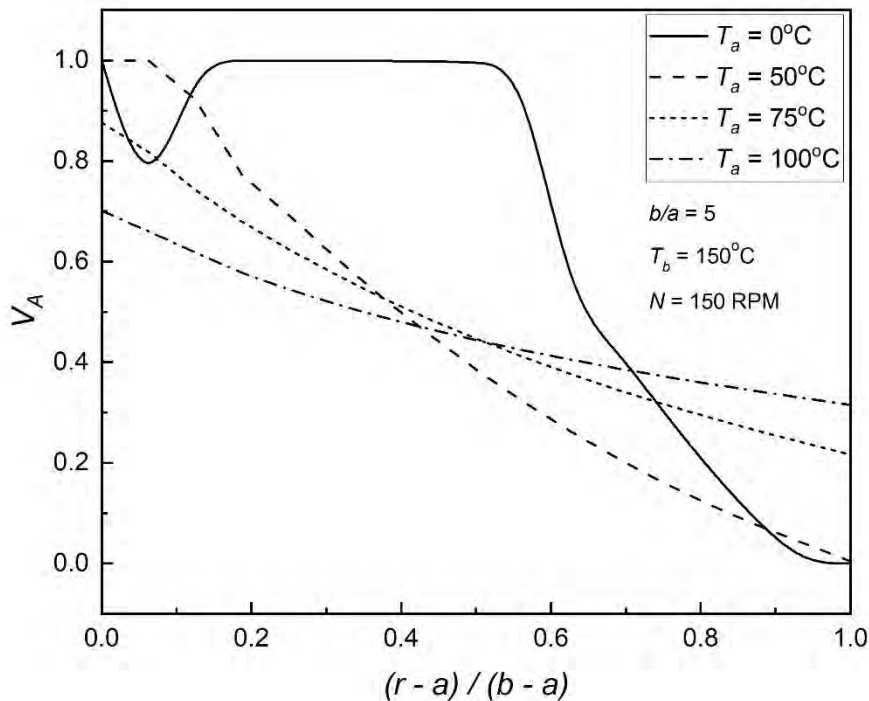


Fig. 5.11: Effect of inner surface temperature on optimum material distribution of an FGM disk under Boundary Condition I.

Chapter 5: Results and Discussion

Fig. 5.11 exhibits that the optimum material distribution near the inner surface of the disk has a tendency to sharply decrease and then increase immediately when the inner surface temperature is at 0°C . The boundary condition at the inner surface is responsible for this behavior. Nevertheless, this behavior is not achieved under the same boundary condition in the other three optimum material distributions presented in Fig. 5.11 due to different inner surface temperatures and temperature differences between inner and outer surfaces. Figs. 5.12 to 5.15 show the von Mises, radial, and circumferential stresses associated with the computed material distributions. Fig. 5.12 exhibits the von Mises stress of an FGM disk with a 0°C inner surface temperature, where it is obvious that the value of von Mises stress is less than 30 MPa across half of the disk and somewhat greater than 30 MPa at the outer surface. However, at the inner surface of the disk, the value is around 73 MPa which is significantly low when compared to the yield stress of the disk.

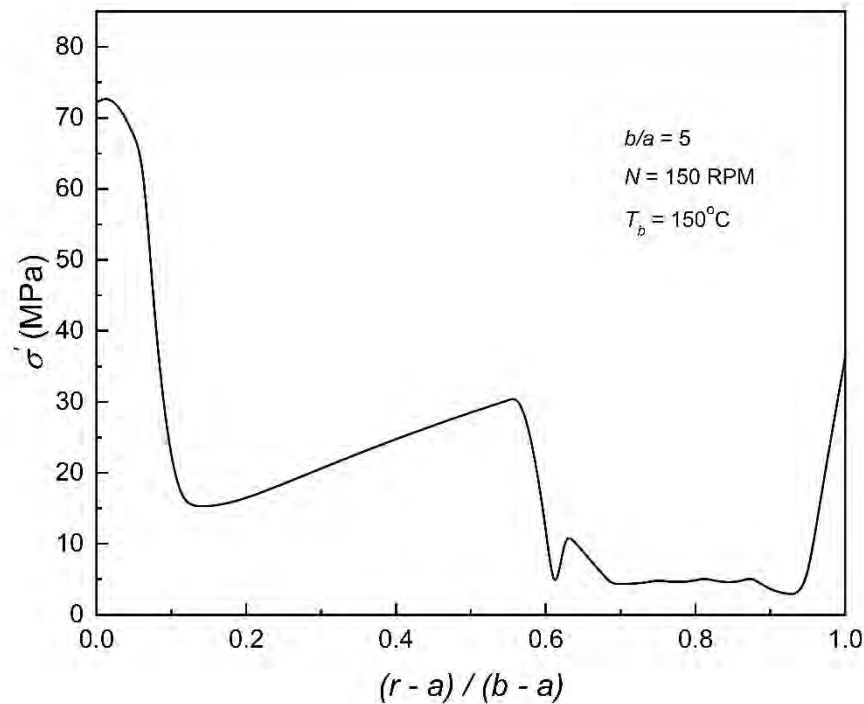


Fig. 5.12: Effect of 0°C inner surface temperature on the minimum von Mises stress corresponding to optimum material distribution of an FGM disk under Boundary Condition I.

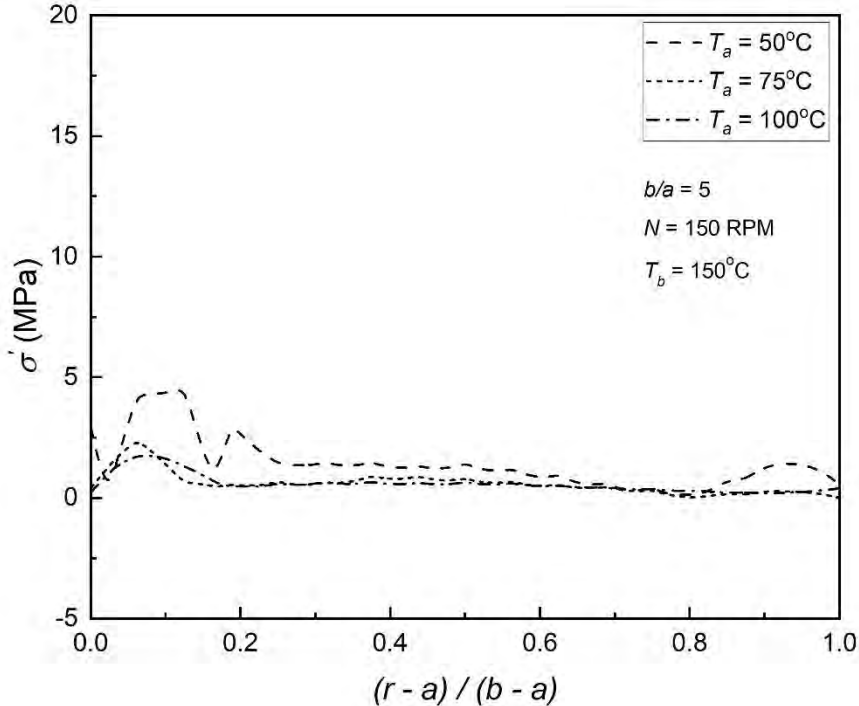


Fig. 5.13: Effect of inner surface temperature on the minimum von Mises stress corresponding to optimum material distribution of an FGM disk under Boundary Condition I.

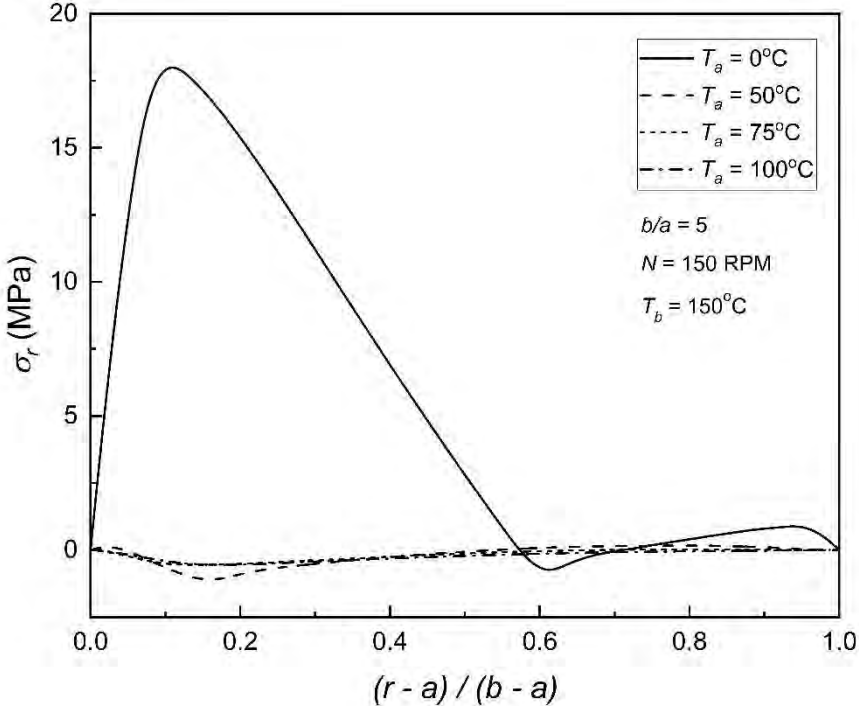


Fig. 5.14: Effect of inner surface temperature on the radial stress corresponding to minimum von Mises stress and optimum material distribution of an FGM disk under Boundary Condition I.

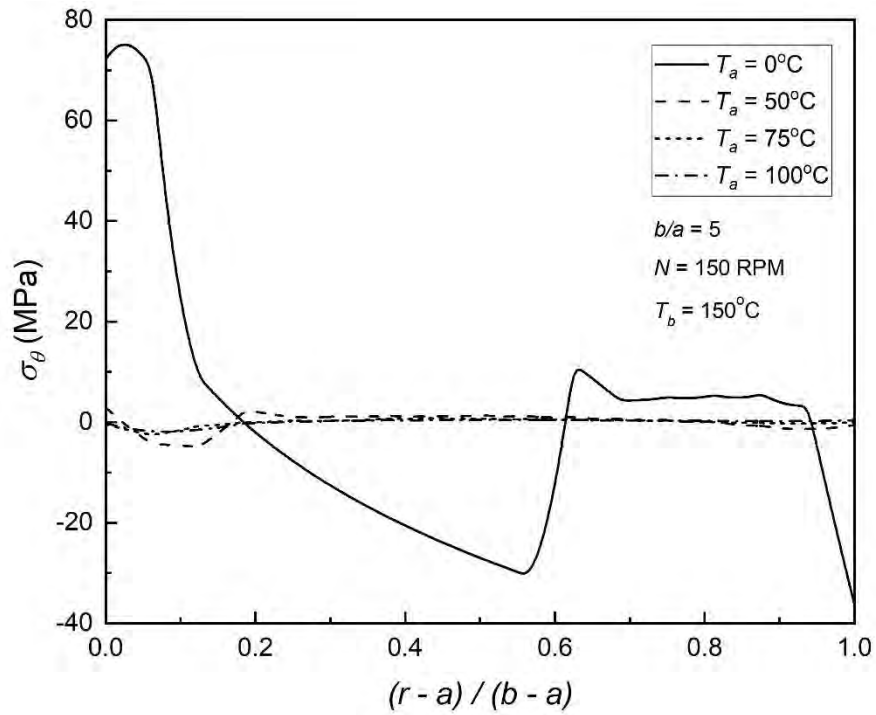


Fig. 5.15: Effect of inner surface temperature on the circumferential stress corresponding to minimum von Mises stress and optimum material distribution of an FGM disk under Boundary Condition I.

Thus, the current study’s optimization model is capable of projecting such a material distribution for which the lowest stress may be attained, which is far below the yield strength of the FGM disk. Furthermore, the numerical values of the von Mises stress decrease dramatically as the inner surface temperature of the FGM disk increases, as seen in Fig. 12 and Fig. 13, because the temperature differences decrease. Fig. 5.13 indicates that at inner surface temperatures of 75°C and 100°C, the values of von Mises stress are almost zero and linear in character. Additionally, values of von Mises stress for 50°C inner surface temperature are higher than that of 75°C and 100°C inner surface temperature of the disk. Nonetheless, in such a situation, the maximum von Mises stress is even less than 5 MPa. As the inner surface temperature of the disk increases, both radial and circumferential stress fall considerably and become nearly linear in nature, as seen in Figs. 5.14 and 5.15. The nature of radial and circumferential stresses at lower inner surface temperatures is similar to that stated in Figs. 5.9 and 5.10. They are not entirely tensile, however, even when the

Chapter 5: Results and Discussion

temperature of the inner surface rises. In addition, Fig. 5.14 exhibits that the radial stresses fulfill the boundary condition.

The inner and outer surface temperatures of the FGM disk are now kept at 20°C and 150°C, respectively, while the rotating speed of the disk is changed to observe the effect on optimum material distribution for the lowest stress profile. The optimal material distribution is represented in Fig. 5.16, where the nature of the distributions is almost identical. However, the numerical values of the optimal volume fraction and the point from which it begins to decrease are not the same for all speeds, and as the rotating speed of the disk increases, the volume fraction of Al begins to decrease earlier along the radial distance of the disk. In addition, the numerical values of the volume fraction of Al are observed to be minimal at 15000 RPM. Because all distributions are calculated for the first boundary condition, and the temperatures at the inner and outer surfaces are constant, the sharp fall and rise nature of the distribution over the inner region of the disk is apparent in all distributions, as seen in Fig. 5.16.

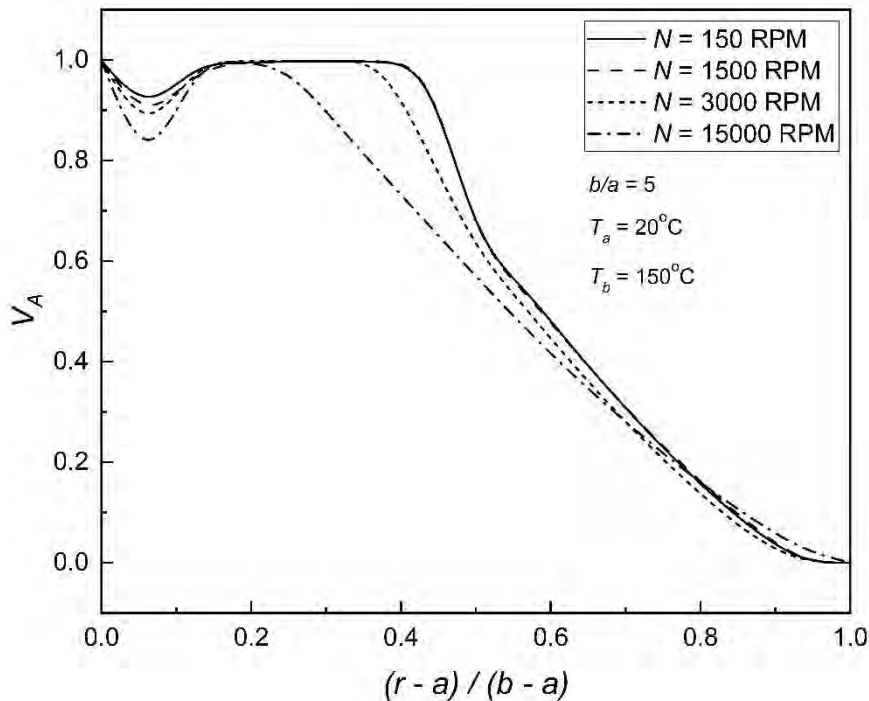


Fig. 5.16: Effect of angular speed on optimum material distribution of an FGM disk under Boundary Condition I.

Chapter 5: Results and Discussion

Figs. 5.17, 5.18, and 5.19 exhibit von Mises, radial, and circumferential stresses that correspond to these optimum material distributions, and the nature of the curves is similar to that of Figs. 5.8, 5.9, and 5.10. Fig. 5.17 reveals that the numerical value of von Mises stress increases with the increase of the rotating speed of the disk over the inner region. Moreover, the material distribution properly minimized the stress profile, such that von Mises stresses across the FGM disk are remarkably similar from low to higher rotating speeds, where the peak value is likewise too low, such as around 65 MPa. Unlike at lower rotating speeds, the von Mises stress profile at a high rotating speed like 15000 RPM corresponding to the optimum material distribution, does not tend to increase over the disk except near the inner and outer surfaces. Though the radial stress rises with increasing rotating speed of the disk throughout the FGM disk, the value of radial stress becomes lower for 1500 RPM than for 150 RPM after about $(r - a)/(b - a) = 0.2$, as described in Fig. 5.18. In addition, the satisfaction of the boundary condition is also observed. Fig. 5.19 demonstrates that circumferential stress values are almost identical for all angular speeds except the angular speed corresponding to 15000 RPM.

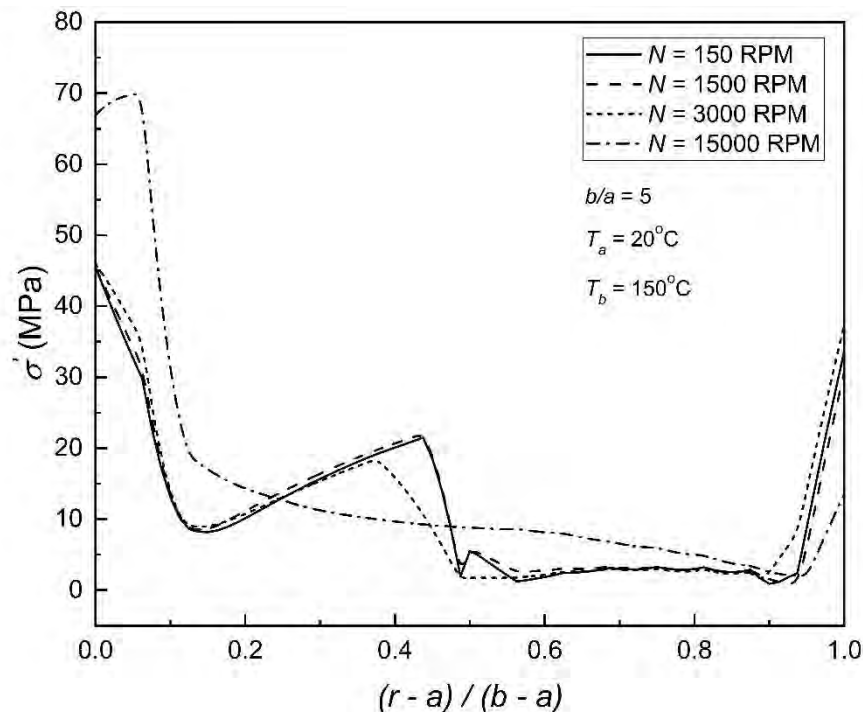


Fig. 5.17: Effect of angular speed on the minimum von Mises stress corresponding to optimum material distribution of an FGM disk under Boundary Condition I.

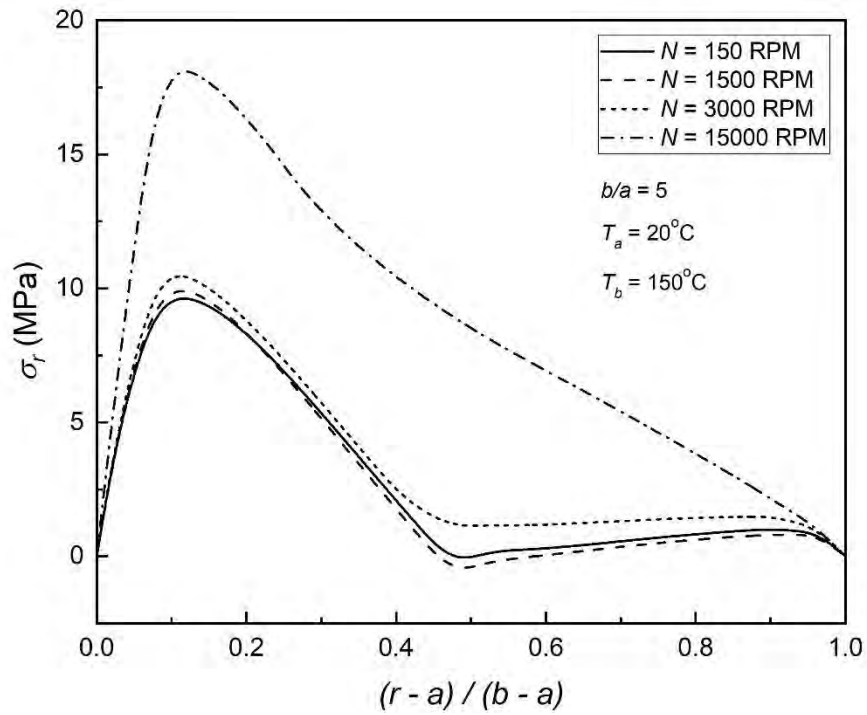


Fig. 5.18: Effect of angular speed on the radial stress corresponding to minimum von Mises stress and optimum material distribution of an FGM disk under Boundary Condition I.

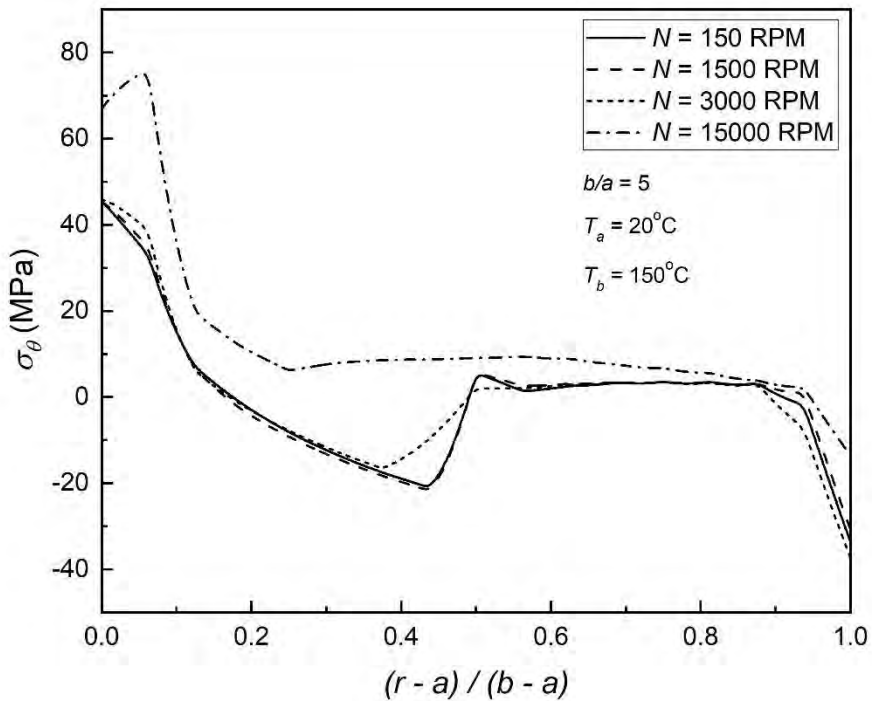


Fig. 5.19: Effect of angular speed on the circumferential stress corresponding to minimum von Mises stress and optimum material distribution of an FGM disk under Boundary Condition I.

Chapter 5: Results and Discussion

Now, an FGM disk has been explored, which rotates at 150 RPM and has inner and outer surface temperatures of 20°C and 150°C, respectively. The optimal material distributions are obtained using an Optimization model for various aspect ratios, namely $b/a = 2.5$, $b/a = 5$, and $b/a = 10$, as shown in Fig. 5.20. The aspect ratio of the FGM disk significantly influences the material distribution of the FGM disk, as seen in Fig. 5.20. The behavior of the material distribution is identical for all aspect ratios, although the numerical values differ along with the point at which the declining nature begins. Moreover, the numerical value of the volume percentage of Al drops throughout the significant region of the disk as the aspect ratio rises. The nature or behavior of the corresponding von Mises, radial, and circumferential stresses is the same. However, since their values are different for different radial thicknesses of the FGM disk, the positions where the curves rise and fall on the normalized radius are also different from each other. The boundary condition causes optimum material distributions to rapidly decline and then increase near the inner surface of the disk, although this nature of the distribution is insignificant in the FGM disk of radial thickness according to $b/a = 10$.

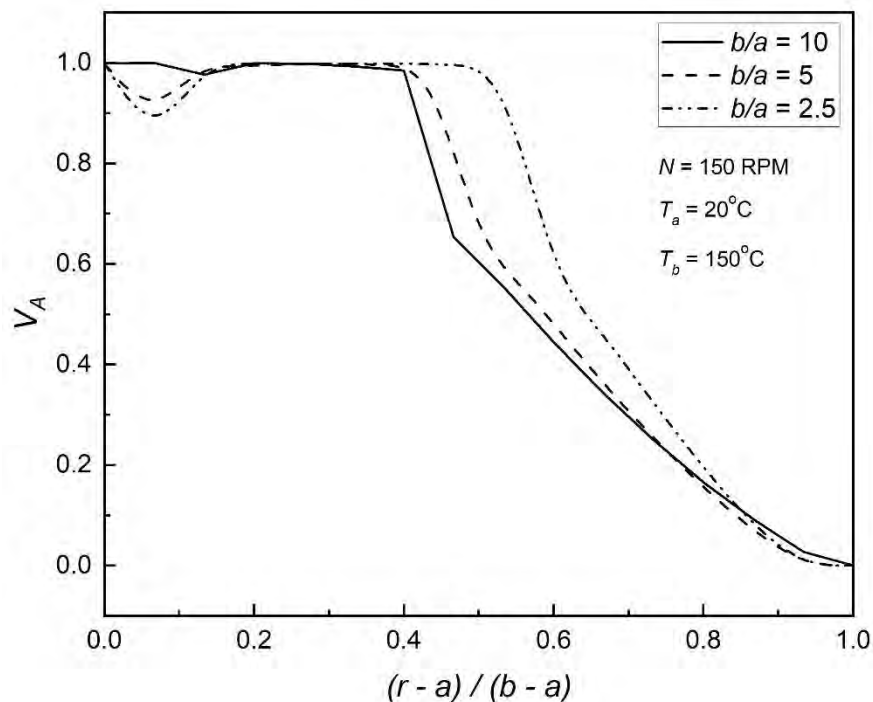


Fig. 5.20: Effect of aspect ratio of disk on optimum material distribution of an FGM disk under Boundary Condition I.

Chapter 5: Results and Discussion

Figs. 5.21, 5.22, and 5.23 depict von Mises, radial, and circumferential stresses. The greatest value of von Mises stress is less than 50 MPa, which is too low relative to the yield stress of the FGM disk. The comparatively higher von Mises stress values are observed only at the inner and outer surfaces. In contrast, the value across the other area is excessively low after the mid-region. Employing optimum material distribution, it is evident from Fig. 5.21 that the FGM disk with $b/a = 10$ has the lowest stress profile over the FGM disk among the mentioned aspect ratios over the normalized radius of 0 to 0.15 and 0.4 to 0.5. Fig. 5.22 illustrates that radial stress of an FGM disk with aspect ratio $b/a = 10$ is found to be compressive across the mid-region. However, when $b/a = 5$, compressive radial stress is measured across a small region. The satisfaction of the boundary condition is also observed in Fig. 5.22.

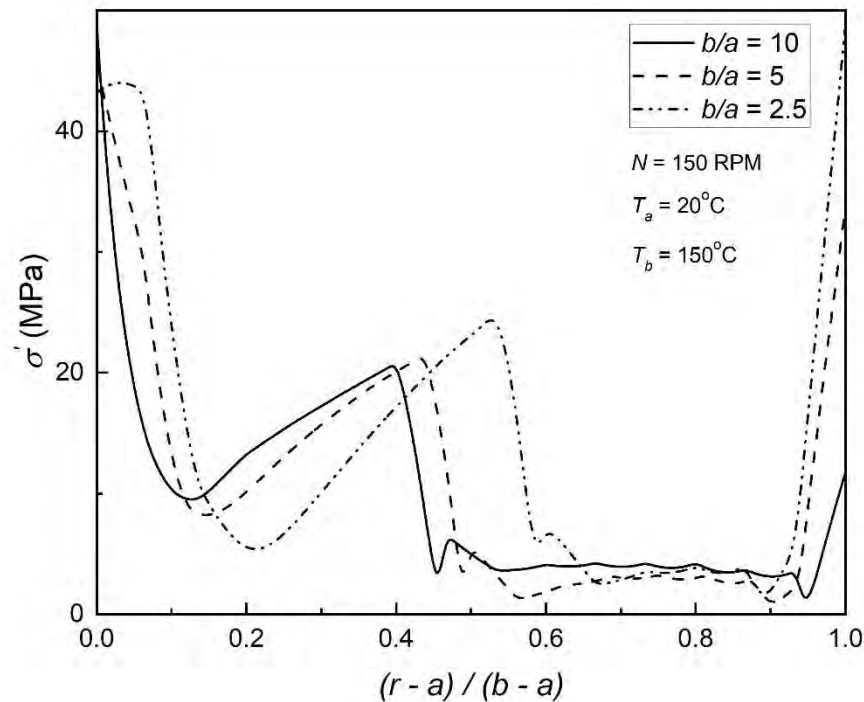


Fig. 5.21: Effect of aspect ratio on the minimum von Mises stress corresponding to optimum material distribution of an FGM disk under Boundary Condition I.

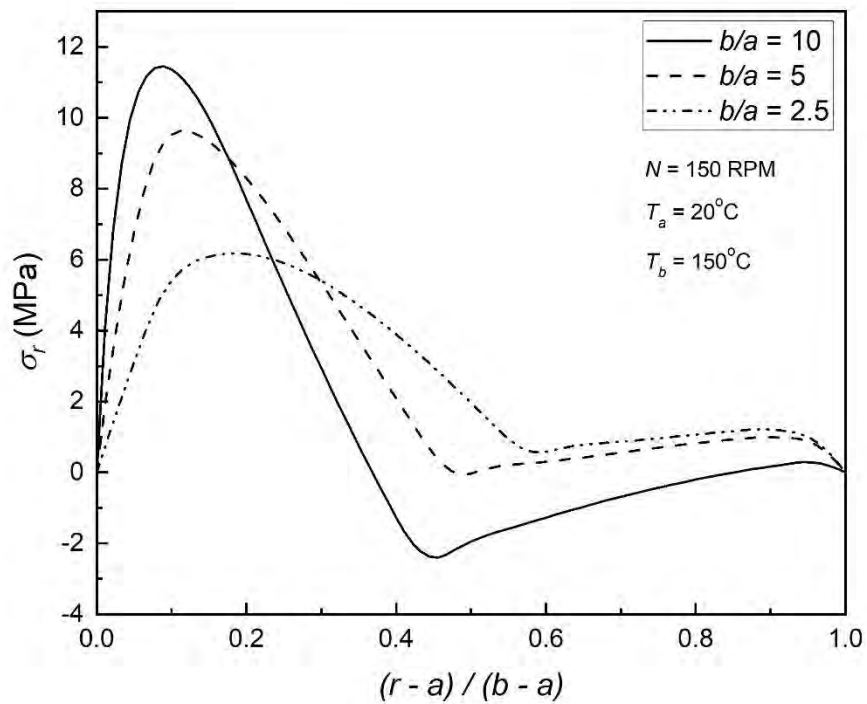


Fig. 5.22: Effect of aspect ratio on the radial stress corresponding to minimum von Mises stress and optimum material distribution of an FGM disk under Boundary Condition I.

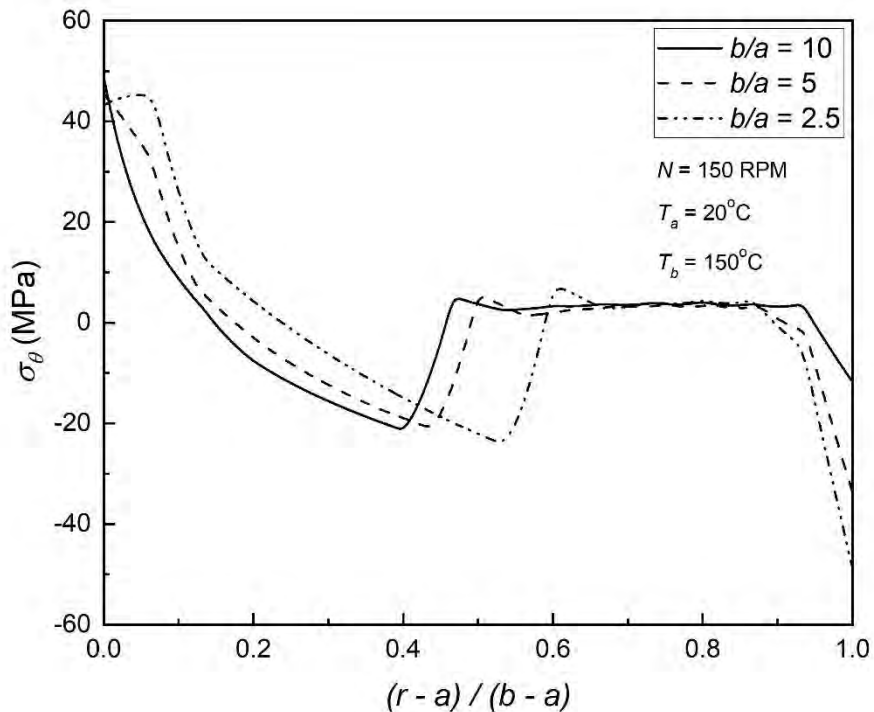


Fig. 5.23: Effect of aspect ratio on the circumferential stress corresponding to minimum von Mises stress and optimum material distribution of an FGM disk under Boundary Condition I.

5.3.2 Boundary Condition: Case II

For the inverse problem of determining the minimum stress profile with the second boundary condition, an FGM disk with $b/a = 5$ was investigated in this section. Material distribution, like the preceding section, is calculated to determine the lowest von Mises stress since the yielding or failing of the material is dependent on the value of the von Mises stress. The FGM disk is configured to rotate at 150 RPM and has an inner surface temperature of 20°C. Like the first boundary condition, the material distribution is determined for three outer surface temperatures, namely 100°C, 200°C, and 300°C, as presented in Fig. 5.24. When Figs. 5.7 and 5.24 are compared, and it is clear that the nature of material distributions is similar for different outer surface temperatures, but the numerical values of volume fractions of constituent A: Al are obviously different at the same normalized radius due to the different boundary conditions. The optimum material distribution for the second boundary condition, unlike the first, does not have a decreasing-increasing tendency near the inner surface because of the different boundary condition.

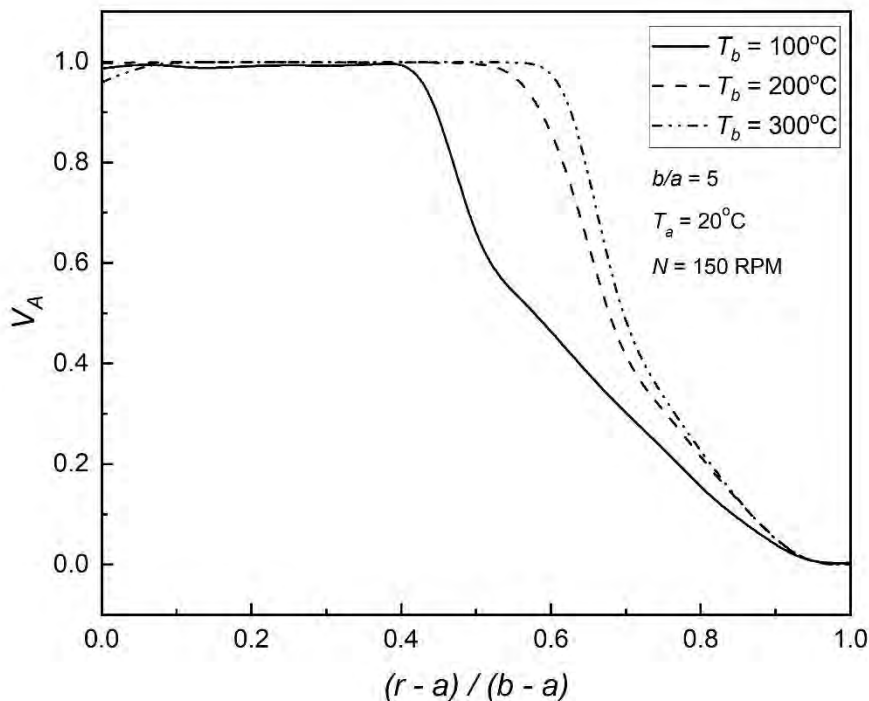


Fig. 5.24: Effect of outer surface temperature on optimum material distribution of an FGM disk under Boundary Condition II.

Chapter 5: Results and Discussion

Figs. 5.25, 5.26, and 5.27 exhibit the von Mises, radial, and circumferential stresses associated with the calculated optimum material distributions. As shown in Fig. 5.25, the outside surface temperature of 100°C causes the least stress, while increasing the outer surface temperature induces the stress to rise, which is the same as the first boundary condition. However, because of the different boundary conditions, the curves have completely different characteristics. The highest value is a little above 120 MPa , which is significantly less than half of the yield stress. Therefore, even when the temperature difference increased, the optimization model successfully estimated the optimum material distribution for which the minimum stress is developing, which is far less than the yield stress of the disk. Fig. 5.26 demonstrates that the radial stress becomes compressive after the center of the disk's radial distance across a short area at all temperatures; otherwise, it stays tensile. When the circumferential stress shown in Fig. 5.27 is studied, it is observed that it is compressive across the major part of the disk except for a tiny region near the outer surface where it is tensile. However, the von Mises stress profile ensures minimum stress across the FGM disk, which is much less than the disk's yield stress.

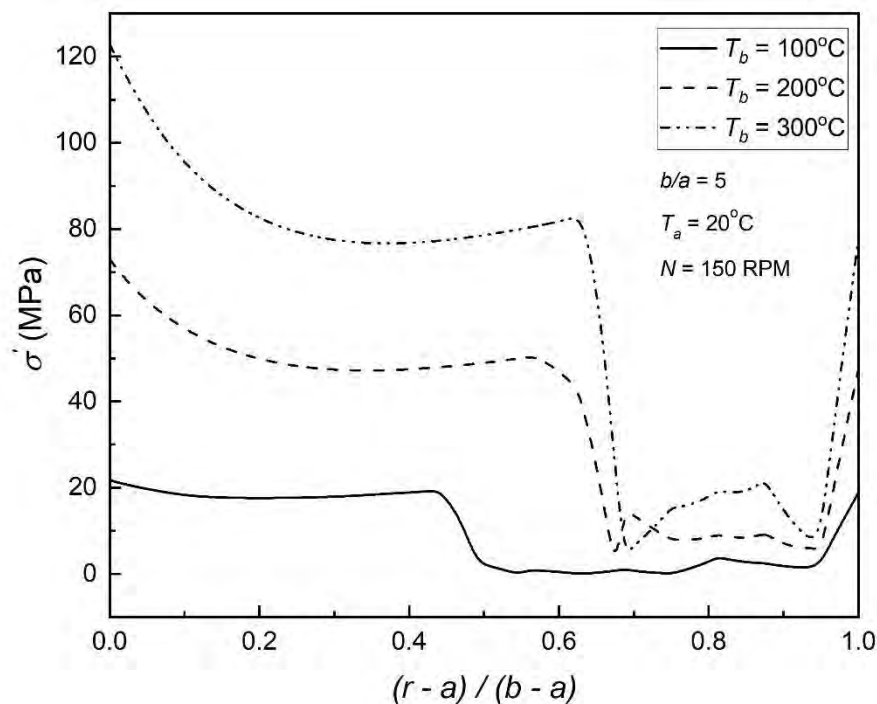


Fig. 5.25: Effect of outer surface temperature on the minimum von Mises stress corresponding to optimum material distribution of an FGM disk under Boundary Condition II.

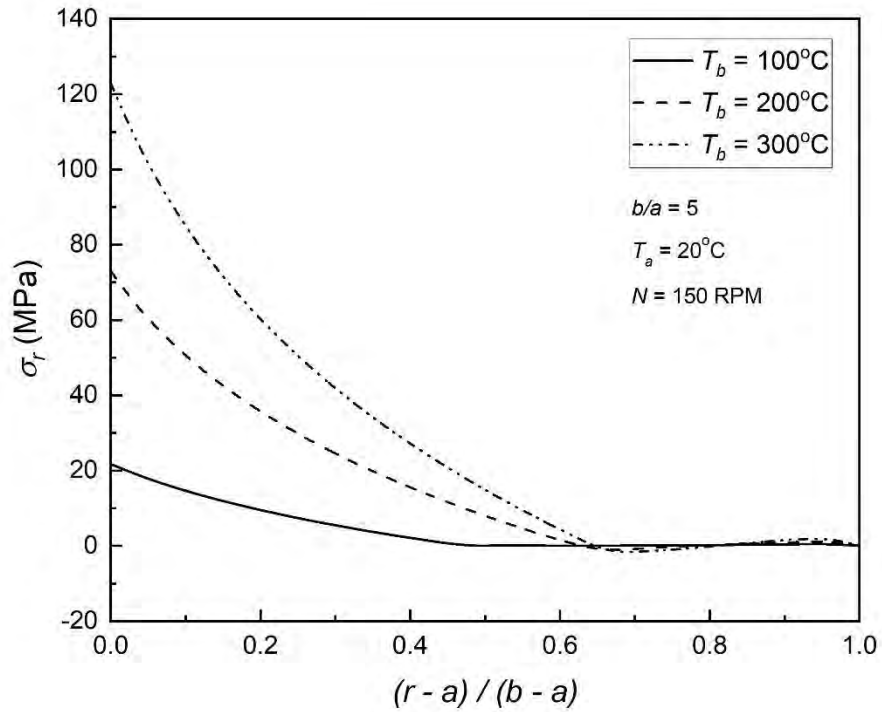


Fig. 5.26: Effect of outer surface temperature on the radial stress corresponding to minimum von Mises stress and optimum material distribution of an FGM disk under Boundary Condition II.

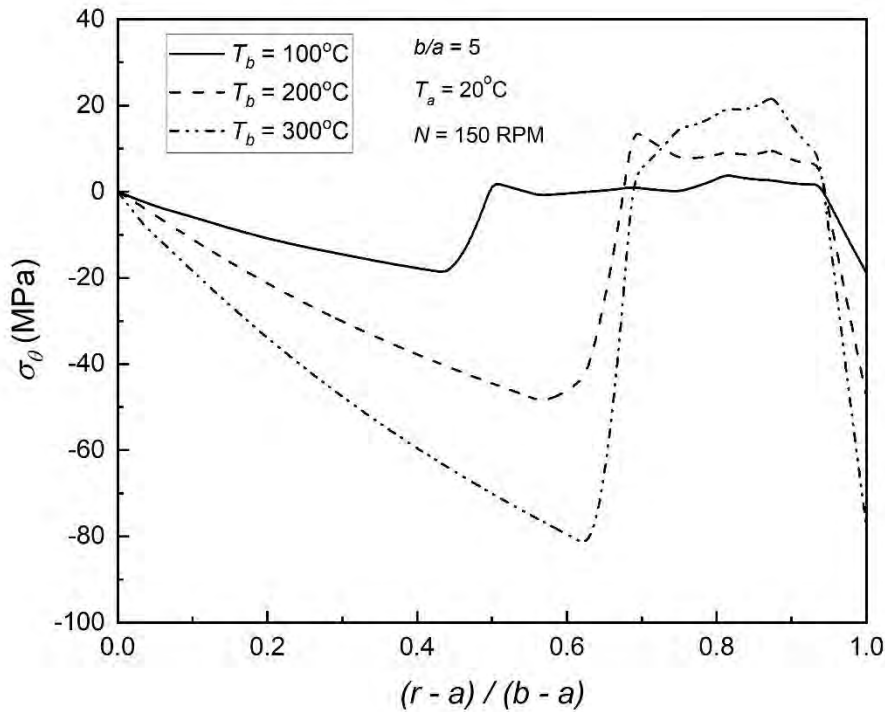


Fig. 5.27: Effect of outer surface temperature on the circumferential stress corresponding to minimum von Mises stress and optimum material distribution of an FGM disk under Boundary Condition II.

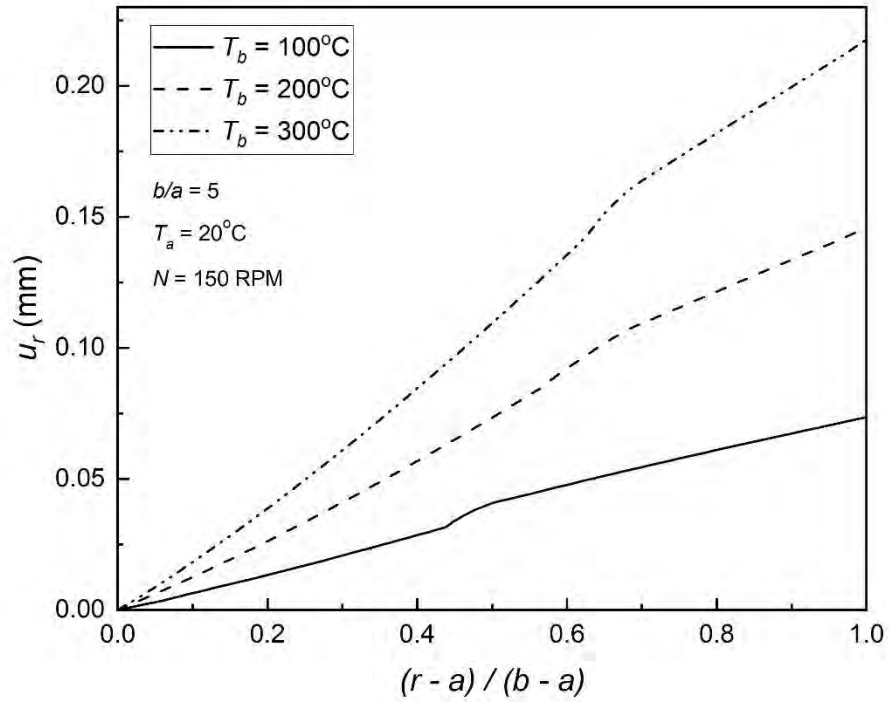


Fig. 5.28: Effect of outer surface temperature on the radial displacement corresponding to minimum von Mises stress and optimum material distribution of an FGM disk under Boundary Condition II.

Fig. 28 illustrates the radial displacement of the FGM disk corresponding to the minimum von Mises stress and optimum material distribution. Fig. 26 and Fig. 28 show that radial stress and displacement are zero at the outer and inner surfaces of the disk, respectively. Thus, the boundary condition is satisfied.

Chapter 5: Results and Discussion

Now, the temperature of the FGM disk's outer surface is kept constant at 150°C , while the inner surface's temperature varies. The calculated material distributions for the minimum von Mises stress profiles obtained by utilizing the optimization model of the current study are shown graphically in Fig. 5.29. In contrast to the first boundary condition, the inner surface of the FGM disk is made up of about 25% Al in the second boundary condition for optimum material distribution at 0°C inner surface temperature because of the different boundary condition. In addition, when the temperature is raised up to 100°C , percent of volume fraction stays between 90 and 100. Fig. 5.29 illustrates that the volume fraction of constituent Al declines throughout the disk's radial distance, except when the inner surface is at 0°C , where it initially jumps to 100% and then begins to drop at the normalized radius of 0.62. Moreover, when the inner surface temperature of the disk is 0°C and 50°C , the volume fraction of Al_2O_3 at the outer surface of the disk is found 100%, but it begins to reduce as the temperature of the inner surface increases. Thus, significant changes in the material distribution have been noticed for varied inner surface temperatures in order to achieve the optimum condition via an inverse approach to minimize stress.

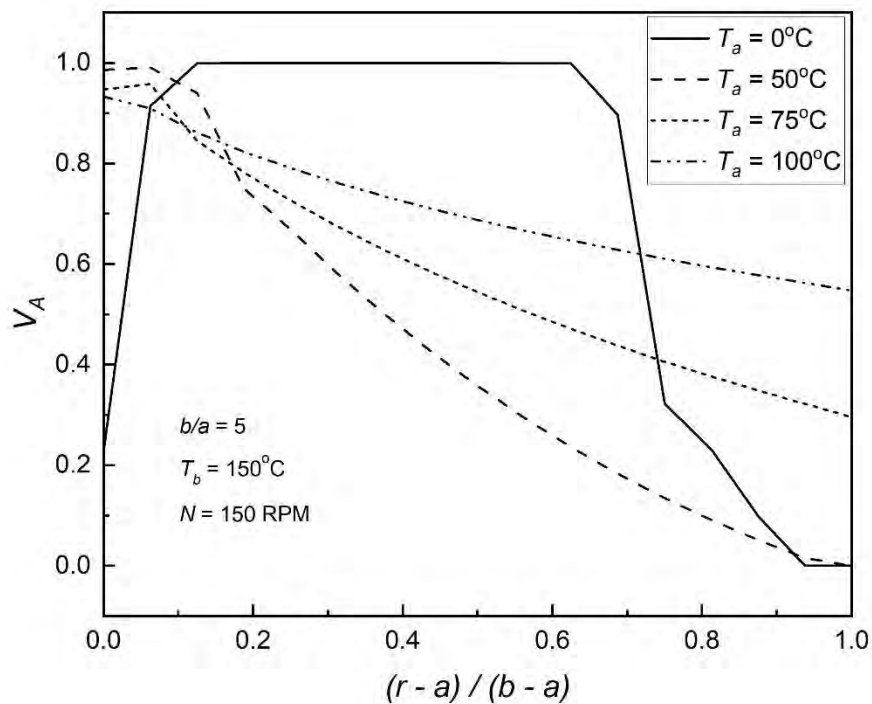


Fig. 5.29: Effect of inner surface temperature on optimum material distribution of an FGM disk under Boundary Condition II.

Chapter 5: Results and Discussion

Figs. 5.30 to 5.33 show the von Mises, radial, and circumferential stresses corresponding to the optimum material distribution obtained from the optimization model. When the von Mises stress is analyzed at various inner surface temperatures, as shown in Figs. 5.30 and 5.31, it is observed that the value of stress is significant only when the inner surface temperature is 0°C. The value is about 85 MPa near the inner surface, yet it is significantly less than the yield stress of the FGM disk. The stress progressively reduces to near zero at the outside surface, and the stress fluctuation is quite non-linear near the outer region, but such values of stress cannot even impact the effectiveness of the FGM disk since they are small when compared to the yield stress. When the inner surface temperature rises, the values of von Mises stress fall precipitously, and stress is almost zero across the FGM disk for smaller temperature differences between the two surfaces of the disk. However, if the inner surface of the disk is at 50°C, the developed stress is now much larger than zero throughout the disk, with the stress being greatest towards the inner and outer surfaces, as demonstrated in the von Mises stress profile of Fig. 5.31.

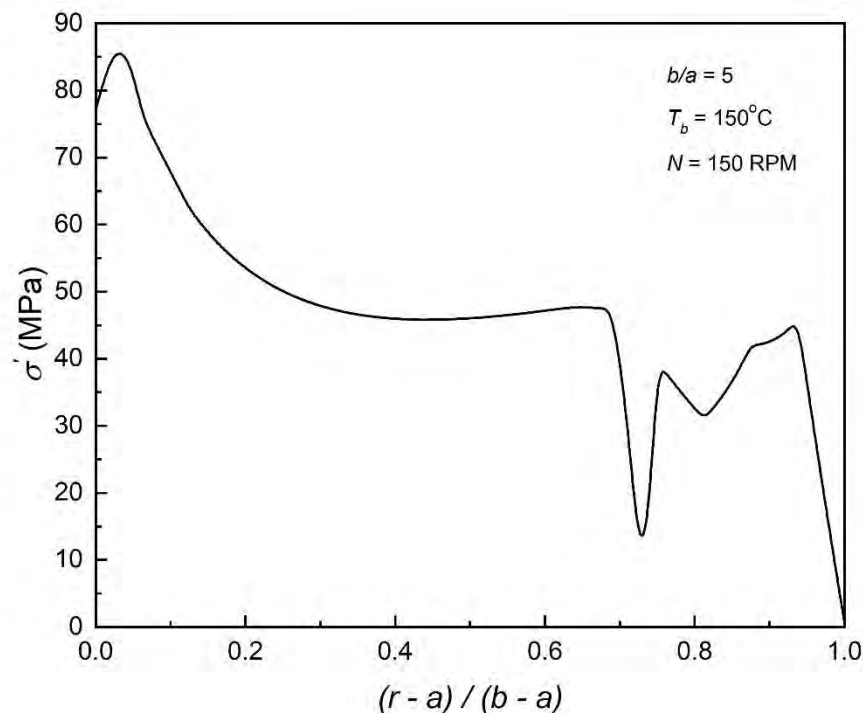


Fig. 5.30: Effect of 0°C inner surface temperature on the minimum von Mises stress corresponding to optimum material distribution of an FGM disk under Boundary Condition II.

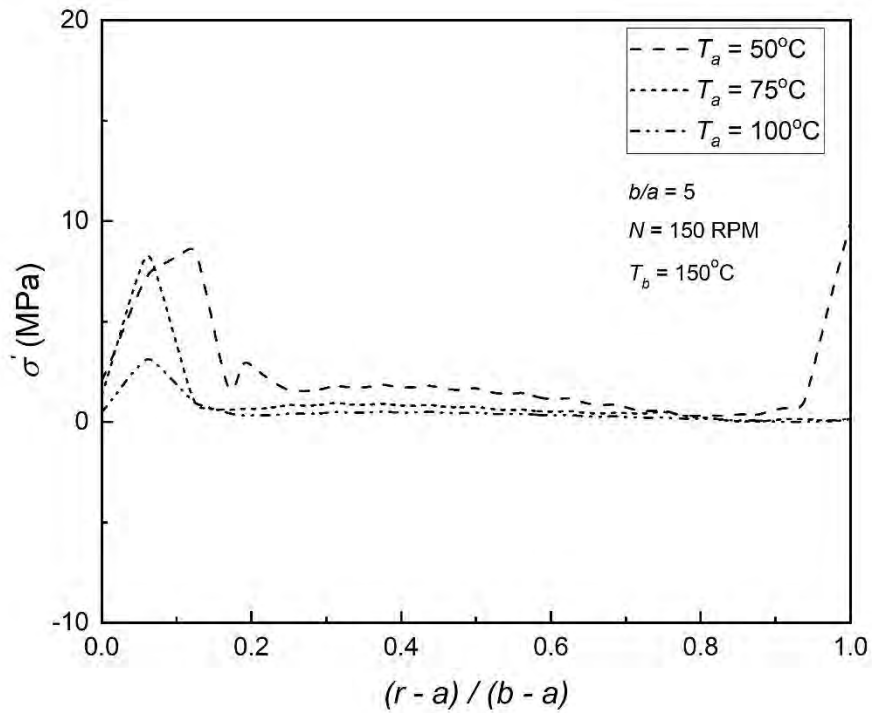


Fig. 5.31: Effect of inner surface temperature on the minimum von Mises stress corresponding to optimum material distribution of an FGM disk under Boundary Condition II.

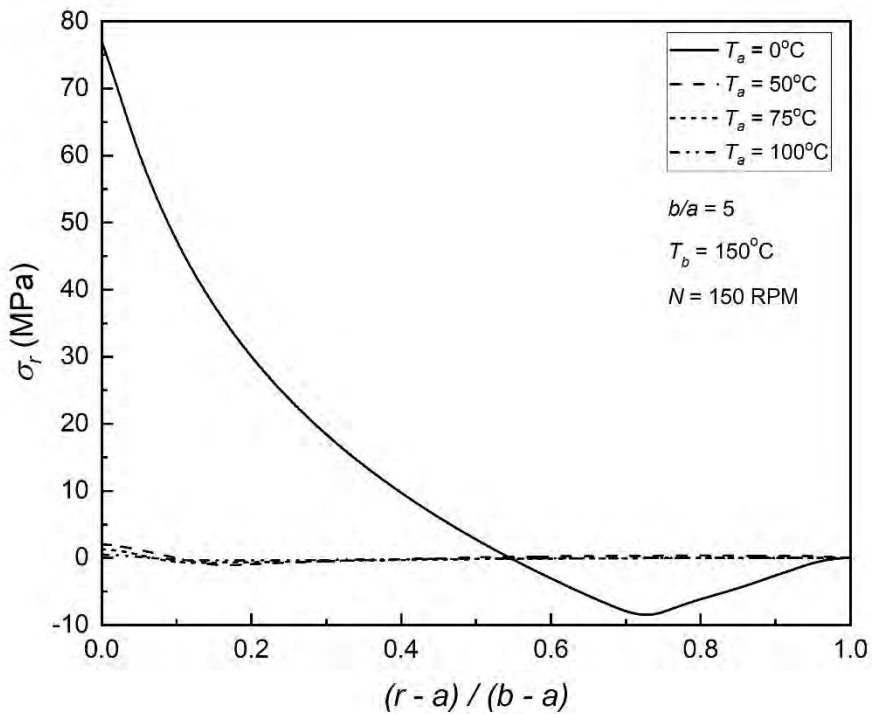


Fig. 5.32: Effect of inner surface temperature on the radial stress corresponding to minimum von Mises stress and optimum material distribution of an FGM disk under Boundary Condition II.

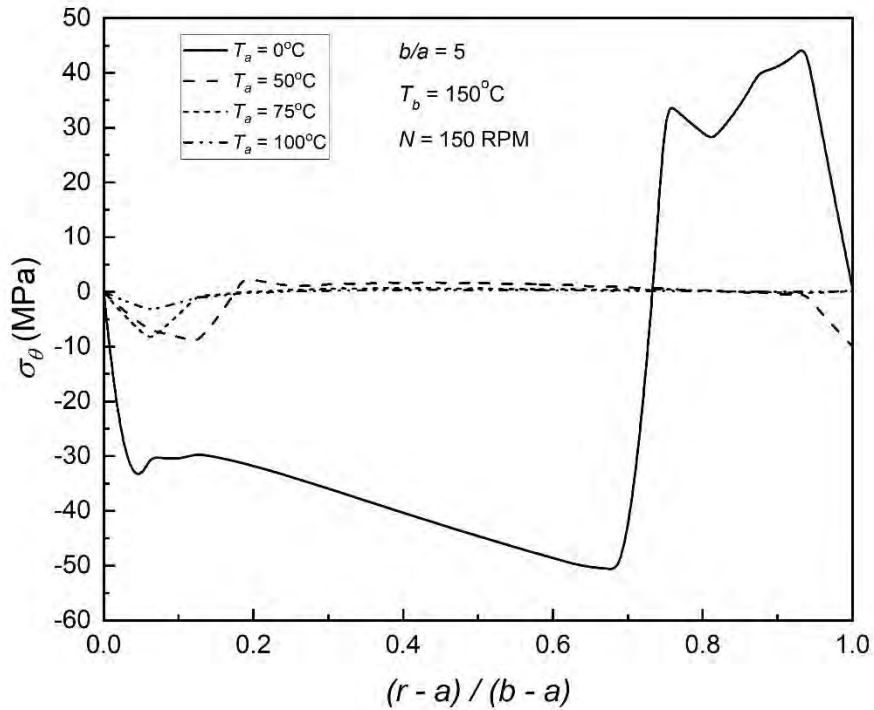


Fig. 5.33: Effect of inner surface temperature on the circumferential stress corresponding to minimum von Mises stress and optimum material distribution of an FGM disk under Boundary Condition II.

In addition, that peak number is around 10 MPa, which is negligible in terms of disk yield stress. Fig. 5.31 also illustrates that near the inner part of the disk, more stress is developed in comparison to the remainder of the disk region. Fig. 5.32 exhibits that for higher inner surface temperatures, radial stress is significant and compressive after approximately $(r - a)/(b - a) = 0.55$. Furthermore, they are nearly negligible for smaller temperature differences and compressive only near the inner surface. Likewise, circumferential stress is almost zero when the inner surface temperature is 50°C , 75°C , and 100°C , as illustrated in Fig. 5.33. When the inner surface temperature is 0°C , circumferential stress is compressive up to the normalized radius of 0.7 and then becomes tensile, whereas when the inner surface temperature is higher, circumferential stress is compressive only near the inner surface and also near the outer surface only if the temperature difference is significant.

Chapter 5: Results and Discussion

The radial displacement of the FGM disk corresponding to the least von Mises stress and optimum material distribution is represented in Fig. 34. Figs. 32 and 34 demonstrate that radial stress and displacement are zero at the disk's outer and inner surfaces, respectively. As a result, the boundary condition has been satisfied.

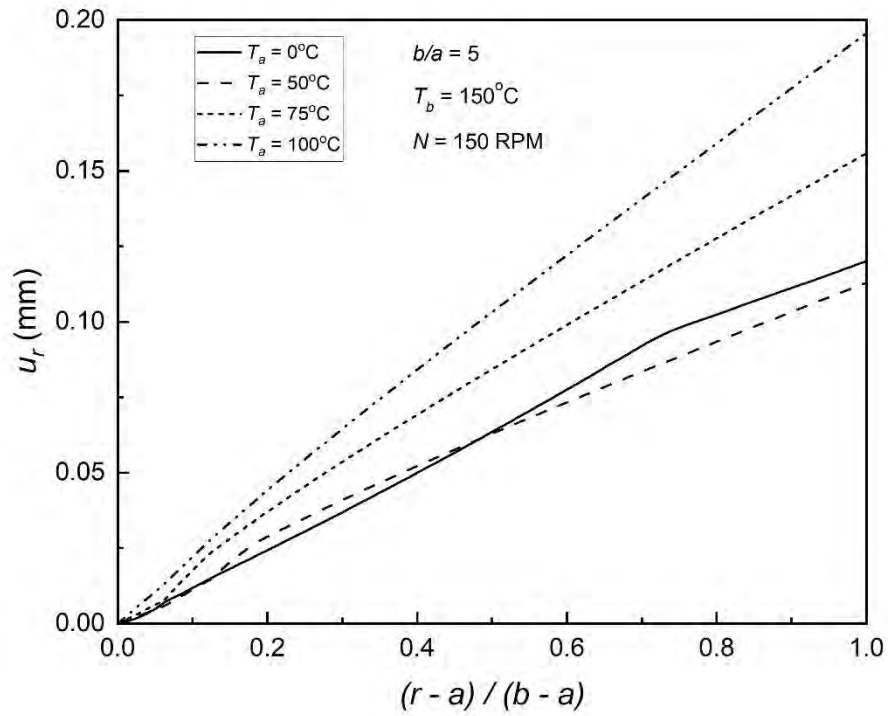


Fig. 5.34: Effect of inner surface temperature on the radial displacement corresponding to minimum von Mises stress and optimum material distribution of an FGM disk under Boundary Condition II.

Chapter 5: Results and Discussion

The inner and outer surface temperatures of the FGM disk are now set at 20°C and 150°C, respectively, while the rotating speed of the disk is varied to determine the optimum material distribution for the lowest stress profile. The optimum material distributions are shown in Fig. 5.35, where all distributions are almost identical except the distribution corresponding to 15000 RPM. Unlike the first boundary condition, in the case of the second boundary condition, optimum material distributions corresponding to the minimum von Mises stress are smooth over the inner region of the FGM disk. When Figs. 5.16 and 5.35 are examined, and it is apparent that, in contrast to the first boundary condition, the discrepancy between the values of volume fractions at various rotational speeds is not noteworthy when the second boundary condition is implemented.

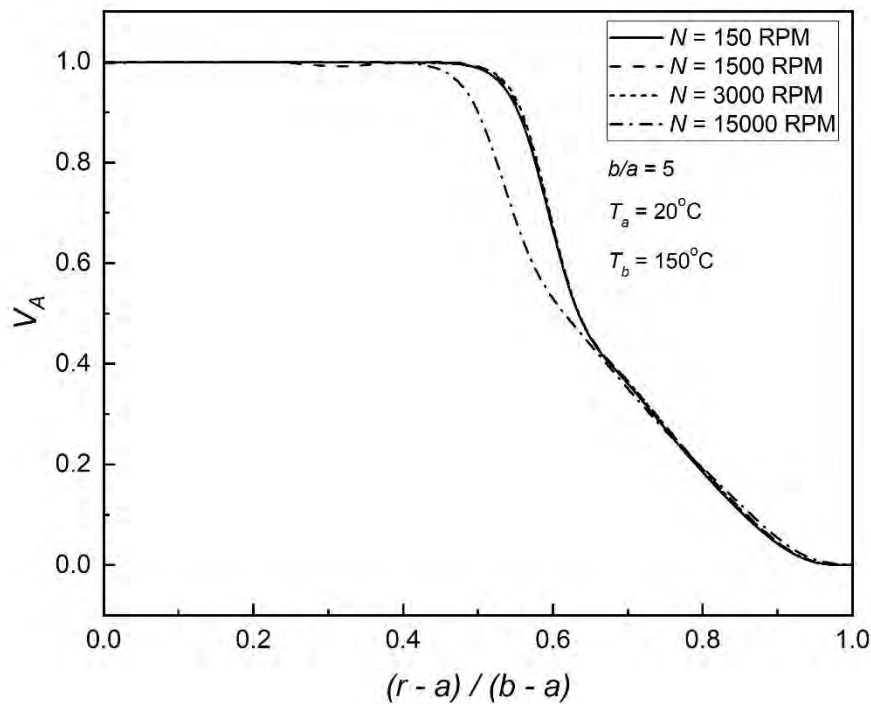


Fig. 5.35: Effect of angular speed on optimum material distribution of an FGM disk under Boundary Condition II.

Chapter 5: Results and Discussion

Figs. 5.36, 5.37, and 5.38 show von Mises, radial, and circumferential stresses that correspond to such optimum material distributions; the nature of the curves is similar to Figs. 5.25, 5.26, and 5.27, and Fig. 5.36 show that the numerical value of von Mises stress increases with the increase of the rotating speed of the disk over the inner region. The von Mises stresses across the FGM disk are remarkably similar from low to higher rotating speeds, where the peak value is likewise too low in comparison with the yield stress, and the peak stress is about 70 MPa. As shown in Figs. 5.37 and 5.38, both the radial and circumferential stresses are almost the same for 150 RPM, 1500 RPM, and 3000 RPM, and increase with an increase in the rotating speed of the disk throughout the FGM disk only at 15000 RPM. However, an exception is observed for the circumferential stress at the normalized radius of 0.36 to 0.88.

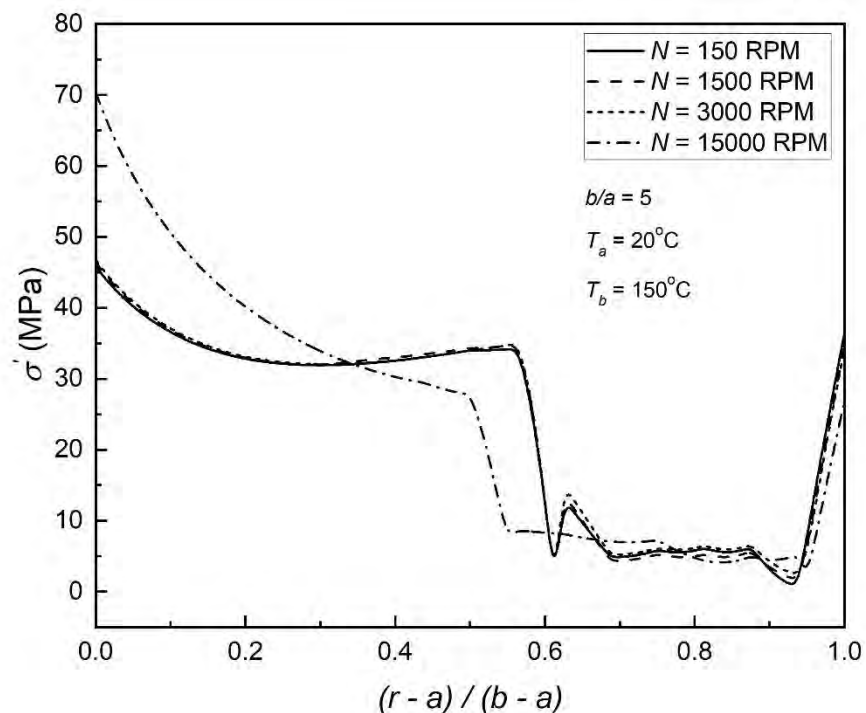


Fig. 5.36: Effect of angular speed on the minimum von Mises stress corresponding to optimum material distribution of an FGM disk under Boundary Condition II.

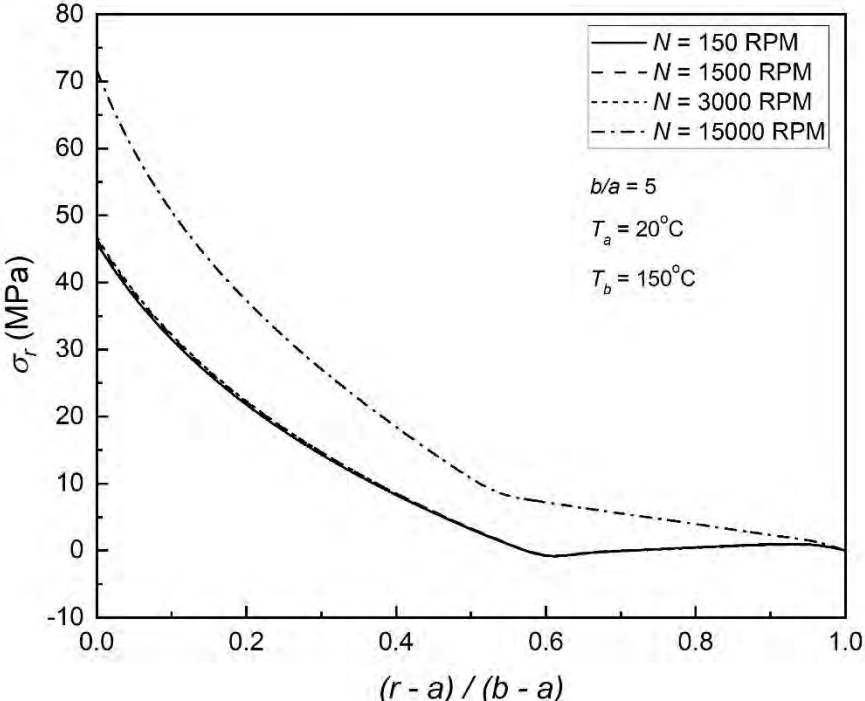


Fig. 5.37: Effect of angular speed on the radial stress corresponding to minimum von Mises stress and optimum material distribution of an FGM disk under Boundary Condition II.

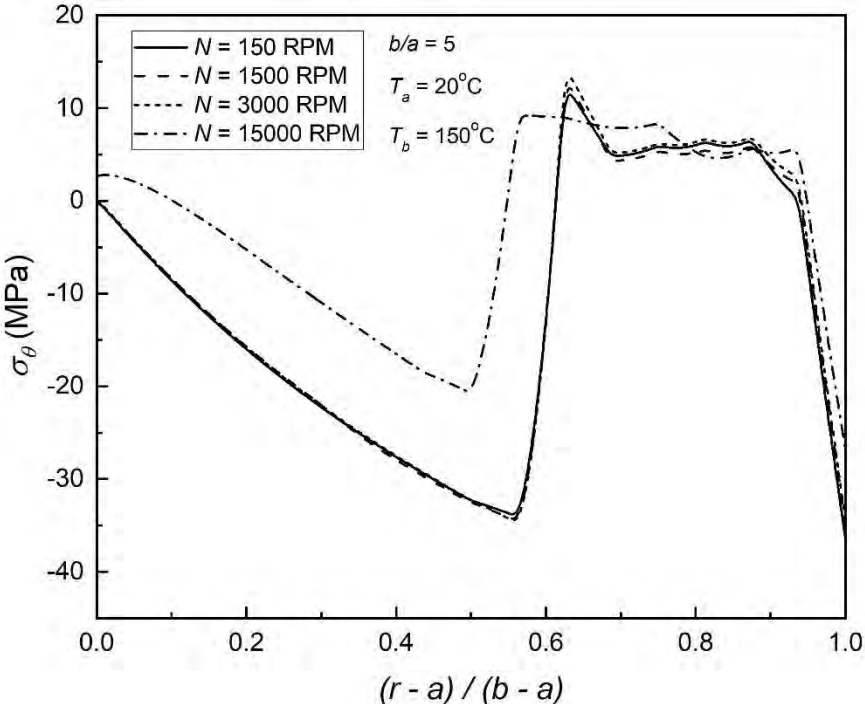


Fig. 5.38: Effect of angular speed on the circumferential stress corresponding to minimum von Mises stress and optimum material distribution of an FGM disk under Boundary Condition II.

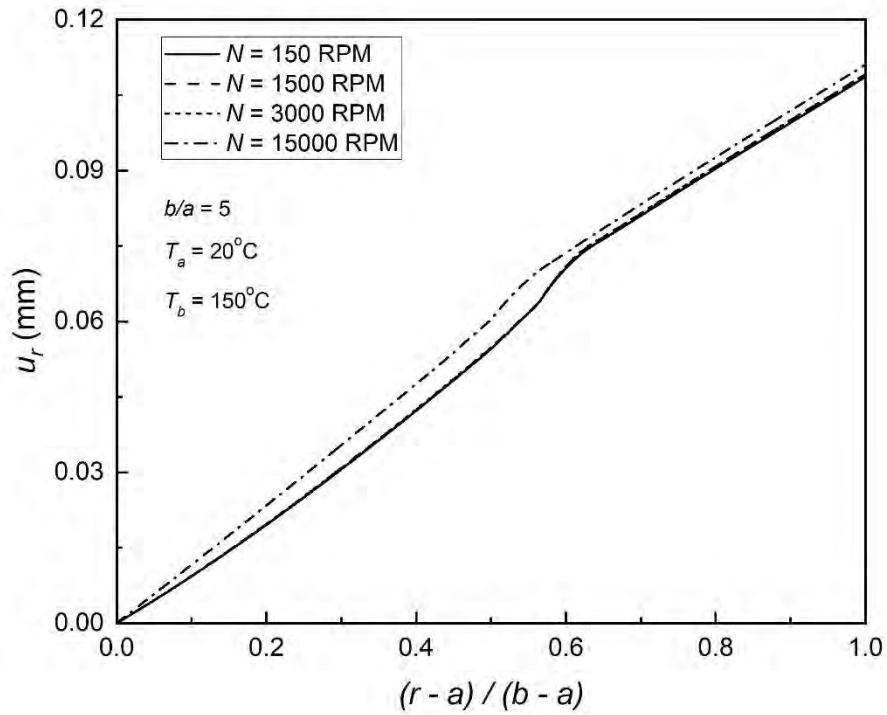


Fig. 5.39: Effect of angular speed on the radial displacement corresponding to minimum von Mises stress and optimum material distribution of an FGM disk under Boundary Condition II.

Fig. 39 depicts the radial displacement of the FGM disk corresponding to the minimum von Mises stress and optimum material distribution. Figs. 37 and 39 illustrate that radial stress and displacement are both zero at the outer and inner surfaces of the FGM disk, respectively. Therefore, the boundary condition is satisfied.

Chapter 5: Results and Discussion

An FGM disk has now been investigated, with inner and outer surface temperatures of 20°C and 150°C, respectively. The optimum material distributions corresponding to the minimum von Mises stress for different aspect ratios, namely $b/a = 2.5$, $b/a = 5$, and $b/a = 10$, are determined using the optimization model and shown in Fig. 5.40. In contrast to the first boundary condition, the second boundary condition results in optimum material distributions that are smooth over the inner region of the FGM disk. Nevertheless, the optimum material distribution of the FGM disk of $b/a = 10$ has a slight increasing-decreasing trend near the inner surface, which is not seen for the first boundary condition. Therefore, boundary condition causes this type of variation in the material distribution. Moreover, the material distribution of the FGM disk is greatly influenced by the aspect ratio of the FGM disk, as shown in Fig. 5.40.

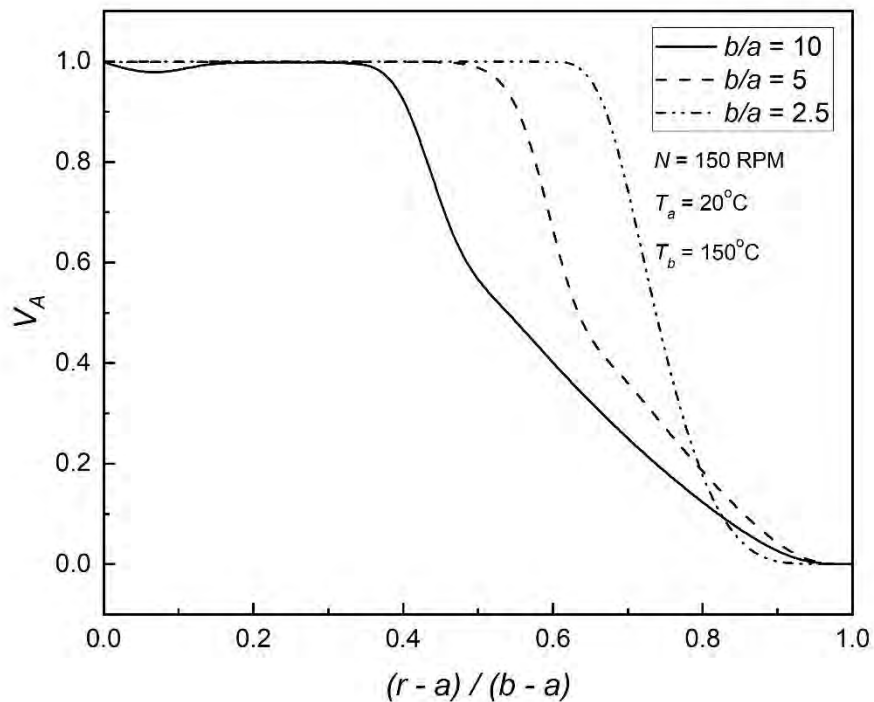


Fig. 5.40: Effect of aspect ratio on optimum material distribution of an FGM disk under Boundary Condition II.

Chapter 5: Results and Discussion

As various radial thicknesses of the FGM disk are taken into consideration, the numerical values of the optimum material distribution and the point at which the material distribution starts to decline are both different. In addition, the numerical value of the volume fraction of Al drops throughout the significant region of the disk as the aspect ratio rises. Figs. 5.41, 5.42, and 5.43 illustrate von Mises, radial, and circumferential stresses. The nature or behavior of the corresponding von Mises, radial, and circumferential stresses is similar. However, since the values are different for different aspect ratios, the positions where the curves rise and fall with the normalized radius are also different from each other. The highest value of von Mises stress is around 90 MPa, which is even less than one-third of the yield stress of the Al. Utilizing optimum material distribution, it is clear from Fig. 5.41 that the FGM disk corresponding to $b/a = 10$ has the minimum stress profile across the FGM disk among the specified aspect ratios.

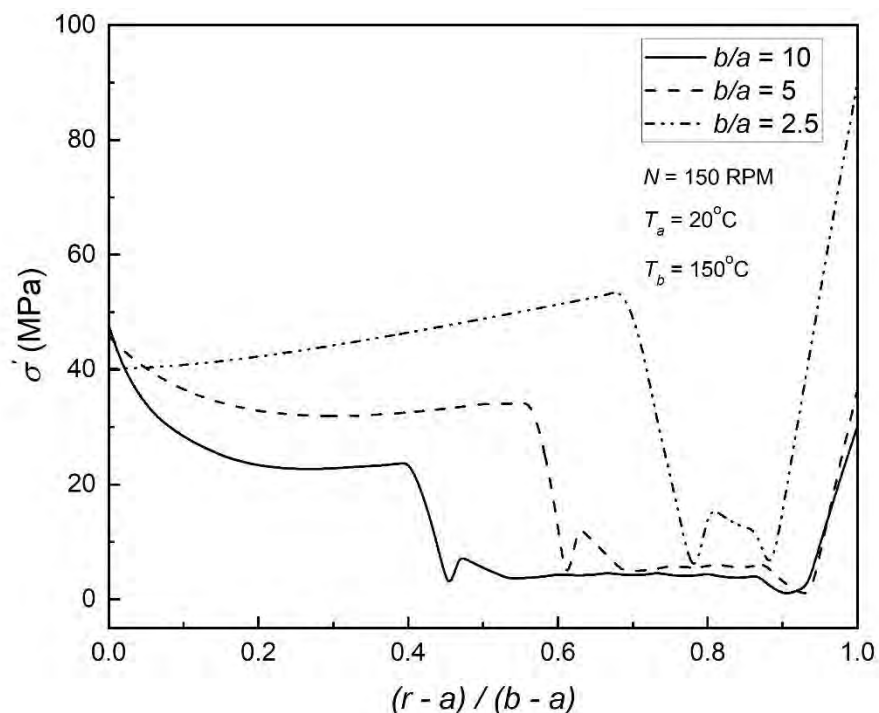


Fig. 5.41: Effect of aspect ratio on the minimum von Mises stress corresponding to optimum material distribution of an FGM disk under Boundary Condition II.

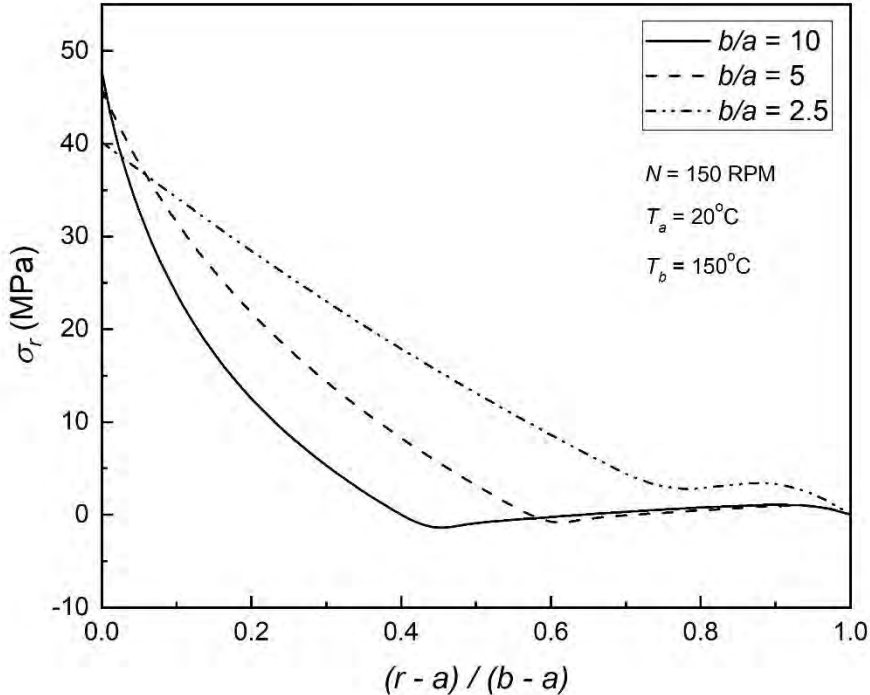


Fig. 5.42: Effect of aspect ratio on the radial stress corresponding to minimum von Mises stress and optimum material distribution of an FGM disk under Boundary Condition II.

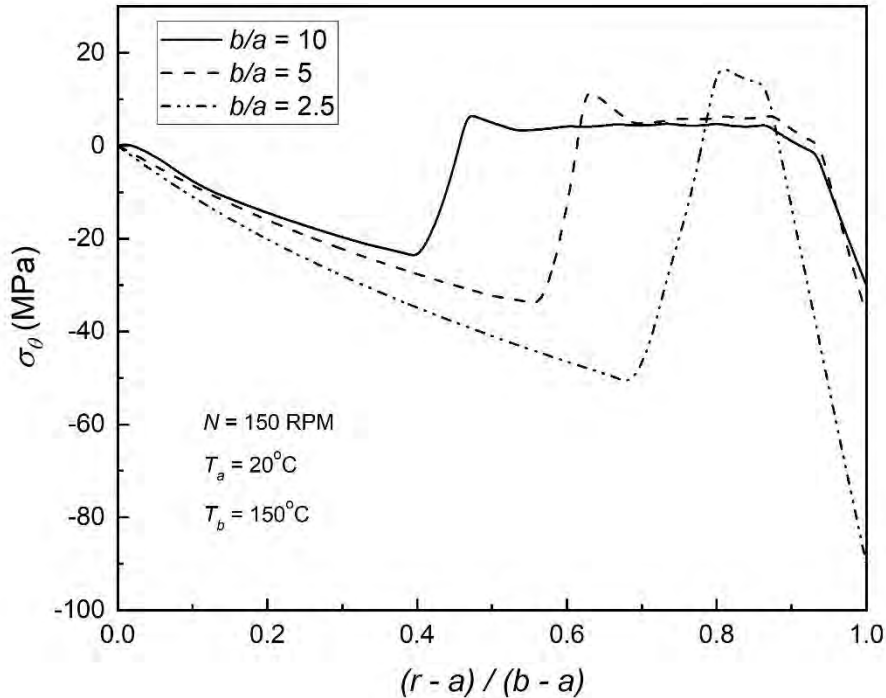


Fig. 5.43: Effect of aspect ratio on the circumferential stress corresponding to minimum von Mises stress and optimum material distribution of an FGM disk under Boundary Condition II.

Chapter 5: Results and Discussion

The radial displacement of the FGM disk corresponds to the minimum von Mises stress and optimum material distribution, as illustrated in Fig. 44. The radial stress and displacement profiles are shown in Fig. 5.42 and Fig. 5.44 confirm that the boundary condition is satisfied since the radial stress at the outer surface and radial displacement at the inner surface of the FGM disk are zero for all aspect ratios.

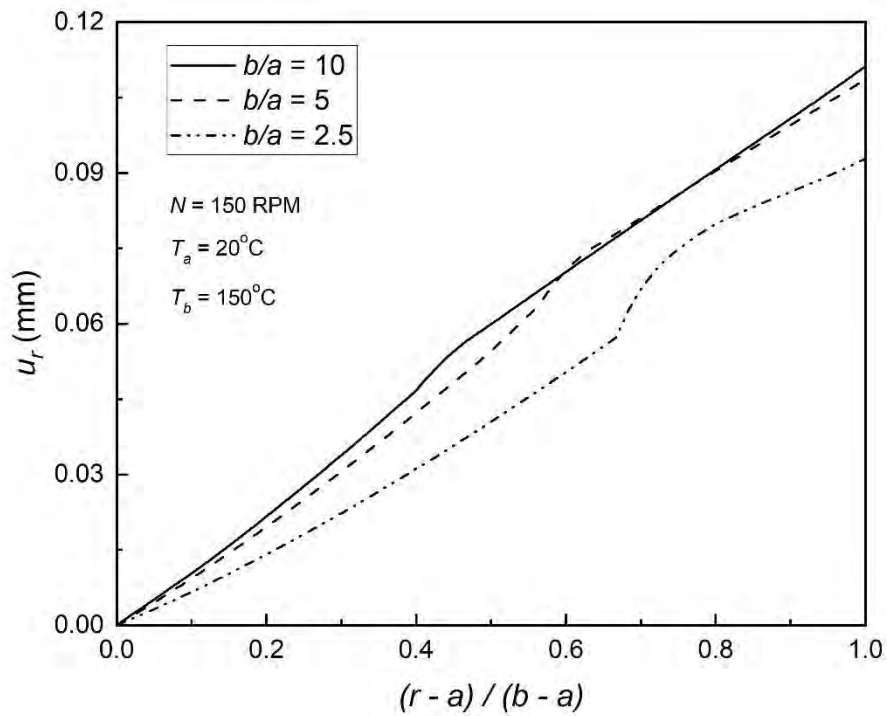


Fig. 5.44: Effect of aspect ratio on the radial displacement corresponding to minimum von Mises stress and optimum material distribution of an FGM disk under Boundary Condition II.

5.4 Evaluation of Optimum Material Distribution Corresponding to Prescribed Stress

5.4.1 Boundary Condition: Case I

The optimization model is used to calculate the optimum material distribution corresponding to the prescribed stress profile with the first boundary condition. FGM disks that correspond to $b/a = 2.5$ and $b/a = 5$ are explored in this study. The value of the von Mises stress is considered to be the basis for the specified stress field since the yielding or failure of the material is dependent on the value of the von Mises stress. The FGM disk is assumed to rotate at 150 RPM and has inner and outer surface temperatures of 20°C and 150°C, respectively. The value of the objective function acquired from the optimization model must be less than or equal to the prescribed small quantity ϵ , specified in Section 4.2.1, in order to determine the optimum material distribution according to the prescribed stress profile. The value of ϵ has been considered 0.1 for the present study.

At first, the prescribed stress is assumed to decrease from 60 MPa to 20 MPa, where the FGM disk corresponds to $b/a = 2.5$, as shown in Fig. 5.45. Since the optimization model yields the value of ϵ as 0.05, the material distribution is acceptable and is illustrated in Fig. 5.46. It is evident from Fig. 5.46 that the optimum material distribution profile decreases significantly near the inner surface of the disk and then again starts to increase, which occurs due to the boundary condition. In the case of minimum von Mises stress profiles implementing the first boundary condition mentioned in Section 5.3.1, this decreasing-increasing nature was also present in the optimum material distributions.

The prescribed stress profile specified in Fig. 5.45 is realized by designing the FGM disk having the material distribution shown in Fig. 5.46.

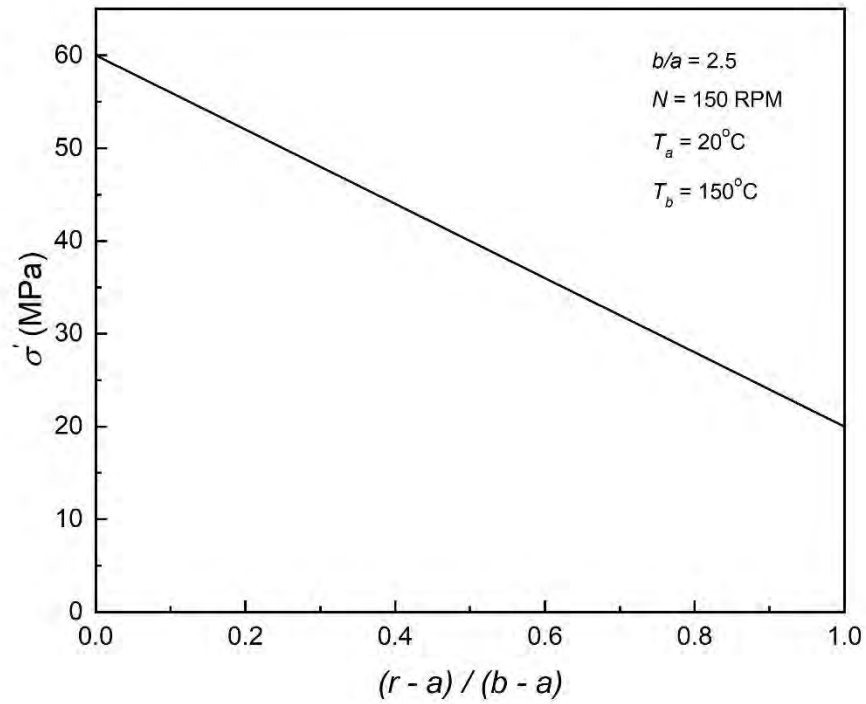


Fig. 5.45: Prescribed stress profile with a decreasing nature in an FGM disk corresponds to $b/a = 2.5$ under Boundary Condition I.

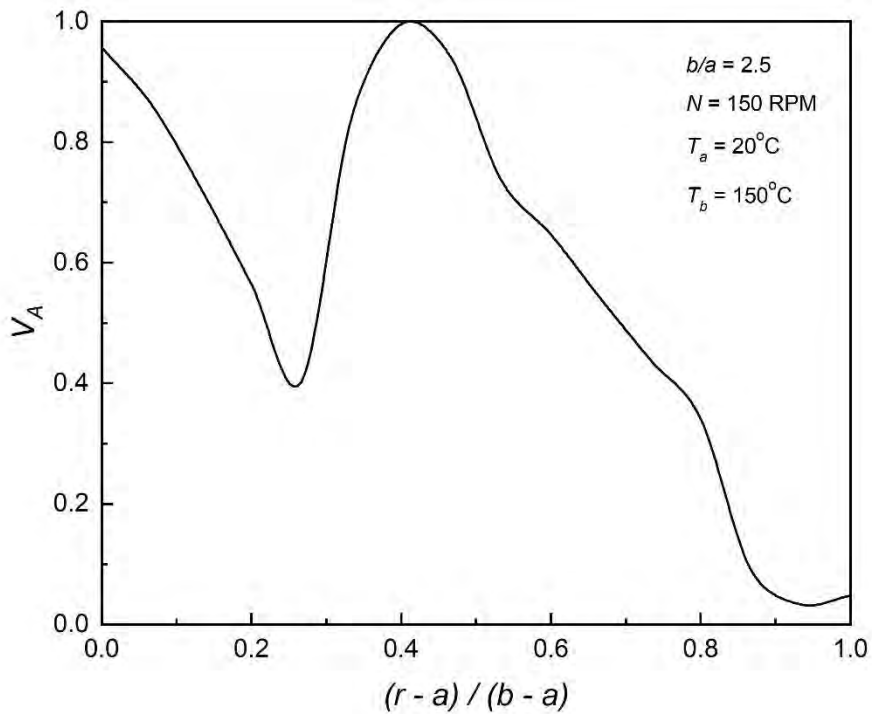


Fig. 5.46: Optimum material distribution in an FGM disk corresponding to the prescribed stress field of Fig. 5.45.

Chapter 5: Results and Discussion

The prescribed stress is then anticipated to grow from 40 MPa to 60 MPa from the inner to the outer surface of the FGM disk of $b/a = 2.5$, as shown in Fig. 5.47. In this scenario, the optimization model calculates ϵ as 0.06. As a result, the material distribution may be accepted and shown in Fig. 5.48. Though a different prescribed stress profile than Fig. 5.45 is realized by the optimum material distribution shown in Fig. 5.48, significant decrease-increase behavior over the inner region of the disk is also present in the distribution. However, the optimum material distribution of Fig. 5.48 is totally different from the distribution of Fig. 5.46 because of different prescribed stress profiles.

By designing the FGM disk with the material distribution depicted in Fig. 5.48, it is possible to realize the prescribed stress profile shown in Fig. 5.47.

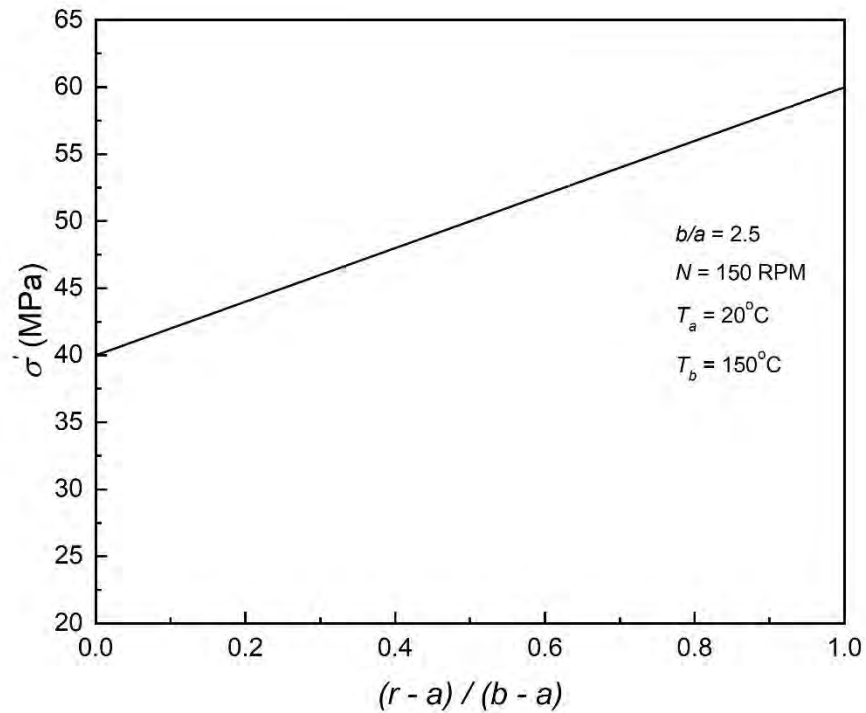


Fig. 5.47: Prescribed stress profile with an increasing nature in an FGM disk corresponds to $b/a = 2.5$ under Boundary Condition I.

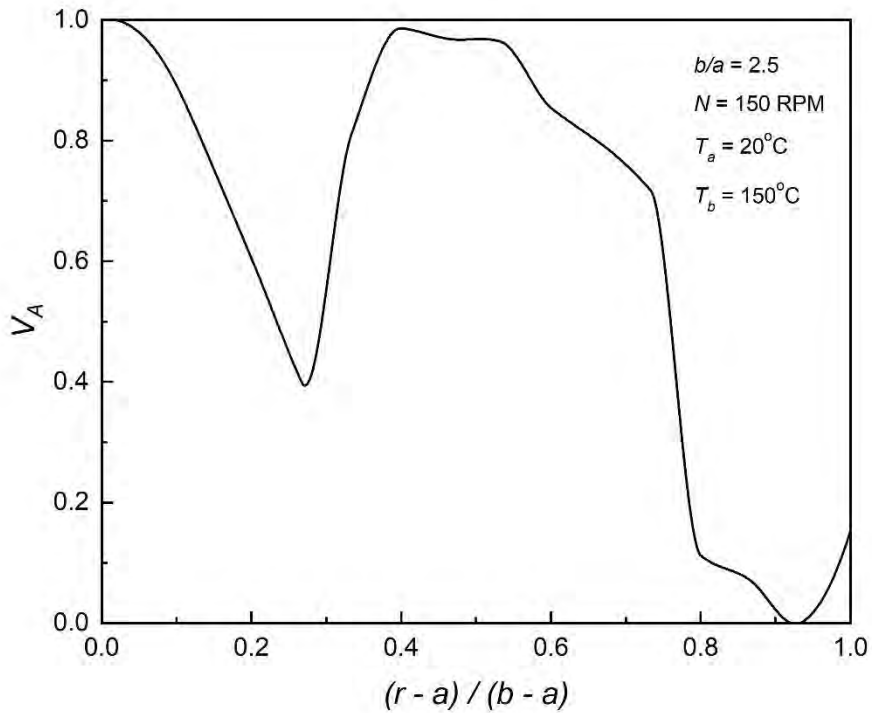


Fig. 5.48: Optimum material distribution in an FGM disk corresponding to the prescribed stress field of **Fig. 5.47**.

Finally, the prescribed stress of 60 MPa is maintained constant from the inner to the outer surface of the FGM disk with $b/a = 2.5$. Fig. 5.49 indicates the prescribed stress profile for this circumstance. In this instance, ϵ equals 0.068, indicating that the material distribution is acceptable and graphically shown in Fig. 5.50. The optimum material distribution with a significant decreasing-increasing trend over the inner region of the disk is obtained because of the first boundary condition.

The prescribed stress profile shown in Fig. 5.49 is predicted by designing the FGM disk having the material distribution illustrated in Fig. 5.50.

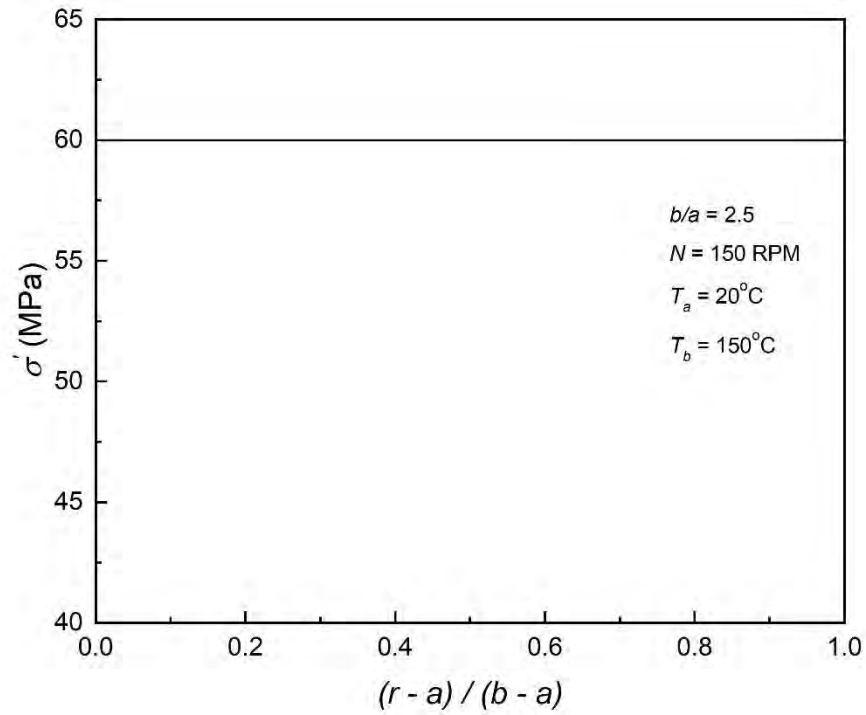


Fig. 5.49: Prescribed stress profile (Constant) in an FGM disk corresponds to $b/a = 2.5$ under Boundary Condition I.

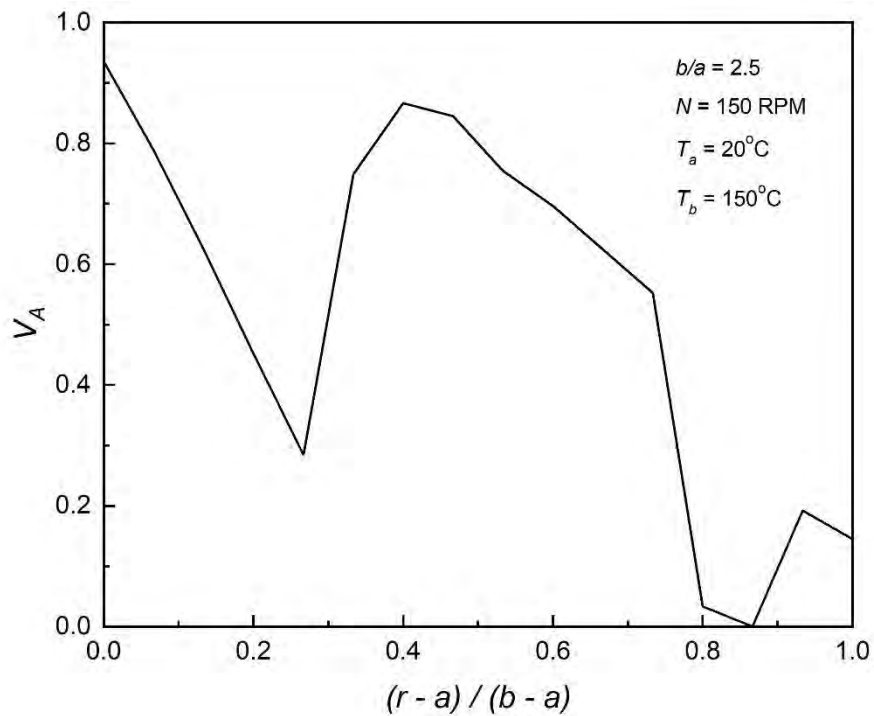


Fig. 5.50: Optimum material distribution in an FGM disk corresponding to the prescribed stress field of **Fig. 5.49**.

Chapter 5: Results and Discussion

The FGM disk having $b/a = 5$ has now been addressed. Firstly, the prescribed stress is predicted to decrease from 60 MPa to 20 MPa from the inner to the outer surface of the FGM disk, as depicted in Fig. 5.51. The value of ϵ is determined to be 0.04 using the optimization model, and thus, the calculated material distribution is able to realize the prescribed stress. Fig. 5.52 exhibits the corresponding material distribution. Optimum material distribution is totally different for the same prescribed von Mises stress profile because of the different radial thickness of the FGM disk. However, the material distribution decreases significantly and then again increases near the inner surface of the disk as the first boundary condition is implemented.

The prescribed stress profile presented in Fig. 5.51 is realized by designing the FGM disk having the material distribution shown in Fig. 5.52.

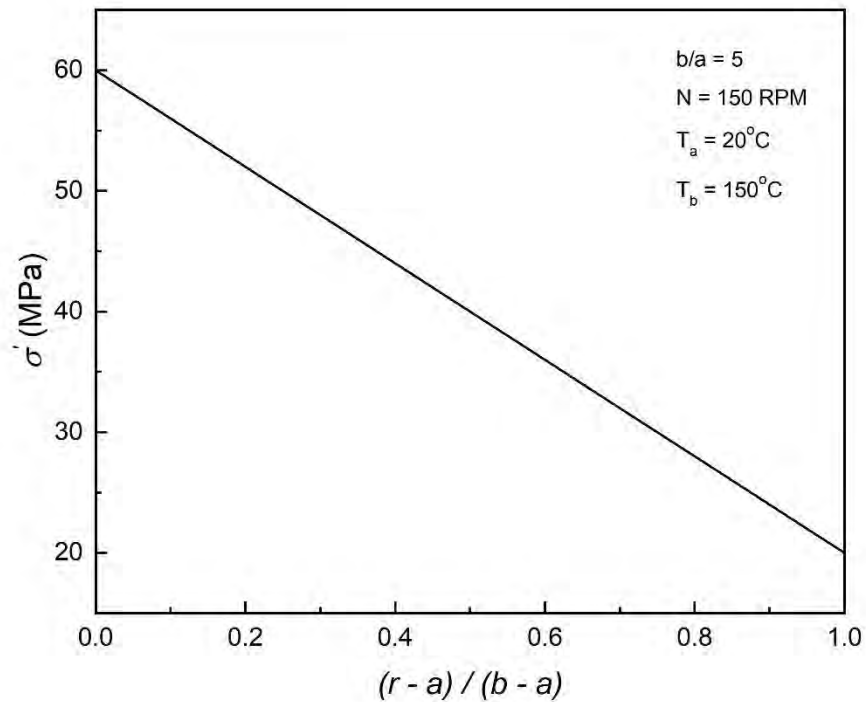


Fig. 5.51: Prescribed stress profile with a decreasing nature in an FGM disk corresponds to $b/a = 5$ under Boundary Condition I.

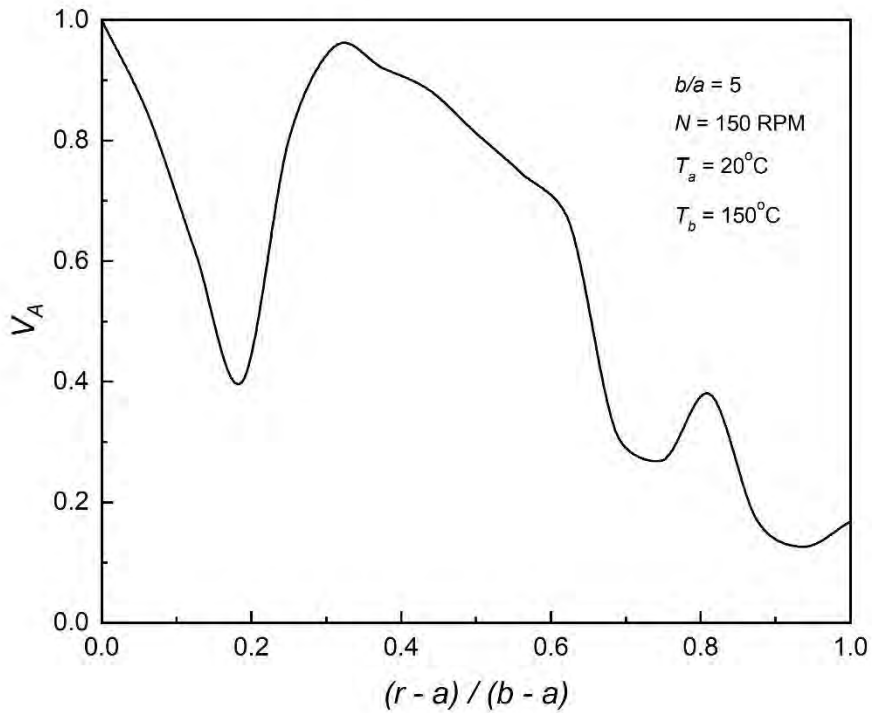


Fig. 5.52: Optimum material distribution in an FGM disk corresponding to the prescribed stress field of Fig. 5.51.

Furthermore, as illustrated in Fig. 5.53, the prescribed stress is projected to increase from 60 MPa to 80 MPa from the inner to the outer surface of the FGM disk with $b/a = 5$. The optimization model yields $\epsilon = 0.09$ for this instance. The optimum material distribution is acceptable as $\epsilon < 0.1$ and is shown in Fig. 5.54. Fig. 5.54 exhibits that the material distribution drops dramatically and then increases up to the normalized radius of 0.5. The first boundary condition is responsible for this behavior of the material distribution. Moreover, the radial thickness of the FGM disk also influences the optimum material distribution.

It is possible to predict the prescribed stress profile shown in Fig. 5.53 by designing the FGM disk with the material distribution of Fig. 5.54

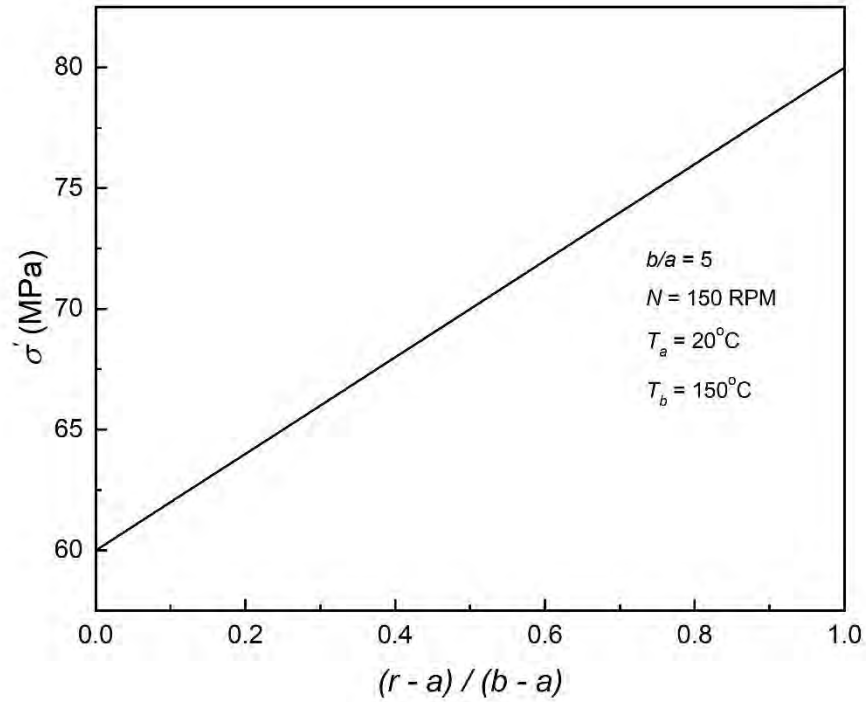


Fig. 5.53: Prescribed stress profile with an increasing nature in an FGM disk corresponds to $b/a = 5$ under Boundary Condition I.

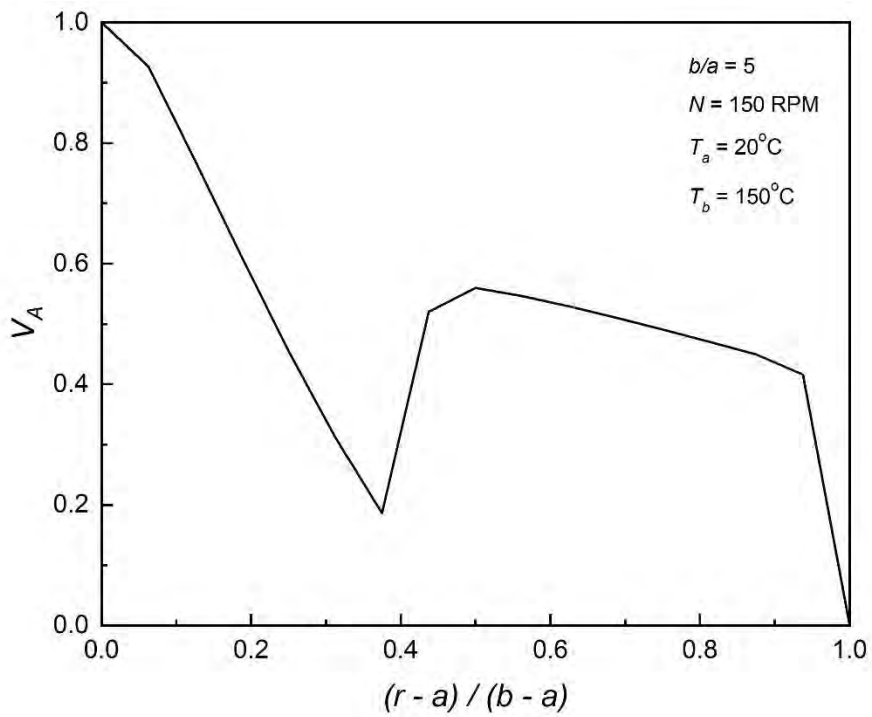


Fig. 5.54: Optimum material distribution in an FGM disk corresponding to the prescribed stress field of Fig. 5.53.

Chapter 5: Results and Discussion

Lastly, the prescribed stress of 60 MPa is kept constant from the inner to the outer surface of the FGM disk, as presented in Fig. 5.55. Now, ϵ is estimated as 0.06 for this prescribed stress using the inverse problem optimization problem of the present work. Therefore, the material distribution may be considered acceptable, as demonstrated in Fig. 5.56. The significant decrease-increase nature is again present in the optimum material distribution profile because of the boundary condition.

By designing the FGM disk with the material distribution shown in Fig. 5.56, it is possible to realize the prescribed stress profile shown in Fig. 5.55.

It is evident from Section 5.4.1 that for the similar prescribed stress field, the material distribution is considerably modified owing to varying values of b/a of the FGM disk.

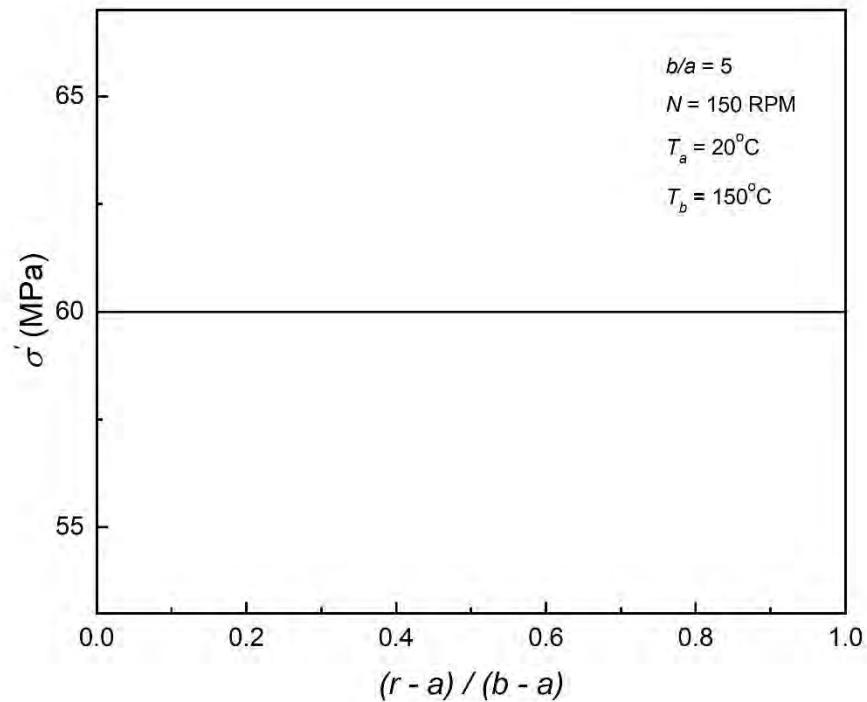


Fig. 5.55: Prescribed stress profile (Constant) in an FGM disk corresponds to $b/a = 5$ under Boundary Condition I.

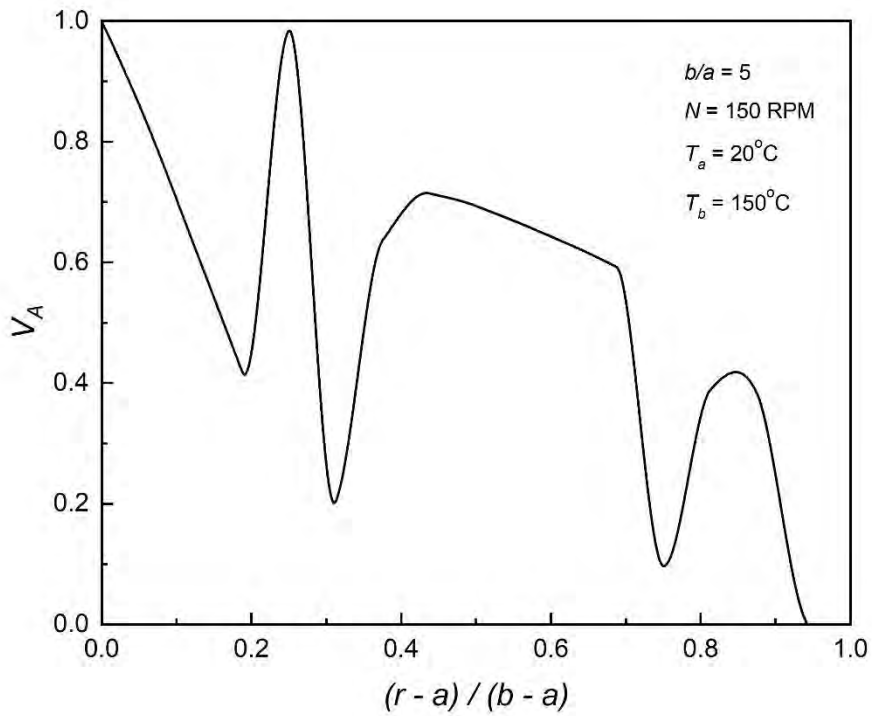


Fig. 5.56: Optimum material distribution in an FGM disk corresponding to the prescribed stress field of **Fig. 5.55**.

5.4.2 Boundary Condition: Case II

In this section, the optimization model is used to find the optimum material distribution for the prescribed stress profile with the second boundary condition. In this work, FGM disks with $b/a = 2.5$ and $b/a = 5$ are investigated. Moreover, the value of the von Mises stress is regarded to be the foundation for the prescribed stress field, similar to the preceding section, since the yielding or failure of the material is reliant on the value of the von Mises stress. The FGM disk revolves at 150 RPM and has 20°C and 150°C inner and outer surface temperatures, respectively. In order to calculate the best material distribution based on the prescribed stress profile, the value of the objective function obtained from the optimization model must be less than or equal to the tolerance provided in Section 4.2.1, as previously noted. In addition, for the purposes of this investigation, the value has been set to 0.1.

Chapter 5: Results and Discussion

As shown in Fig. 5.57, the prescribed stress is supposed to drop from 70 MPa to 40 MPa, where the FGM disk corresponds to $b/a = 2.5$. Because the optimization model yields the value of ϵ as 0.07, the material distribution is acceptable and is shown in Fig. 5.58. Unlike the first boundary condition, optimum material distribution for the second boundary condition doesn't have a significant decrease-increase nature near the inner surface of the disk. However, the distribution decreases to the extent that is far less than that of the first boundary condition. Thus, the boundary conditions have a significant effect on the optimum material distribution.

The prescribed stress profile specified in Fig. 5.57 is realized by designing the FGM disk having the material distribution shown in Fig. 5.58.

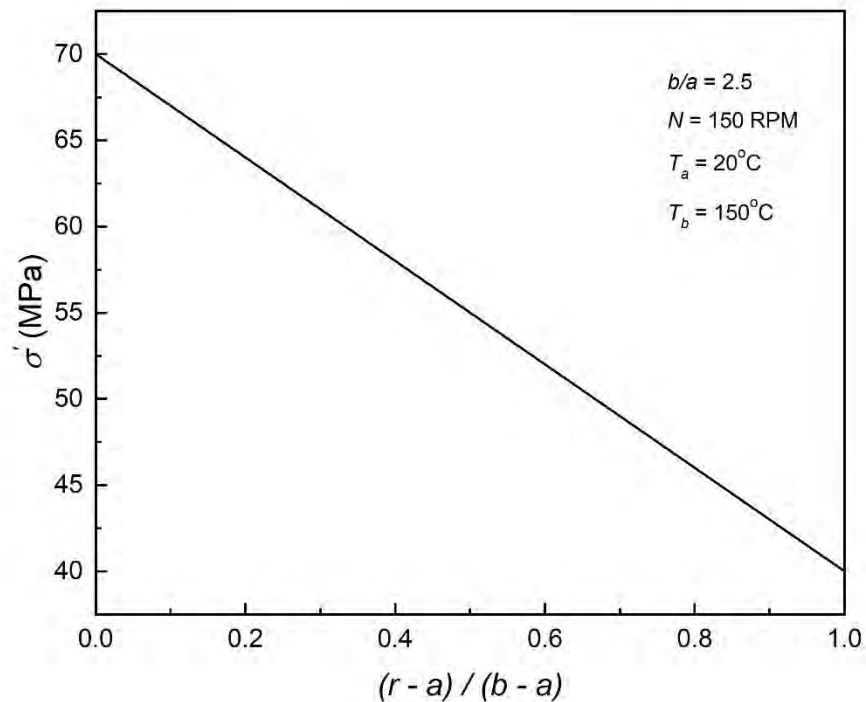


Fig. 5.57: Prescribed stress profile with a decreasing nature in an FGM disk corresponds to $b/a = 2.5$ under Boundary Condition II.

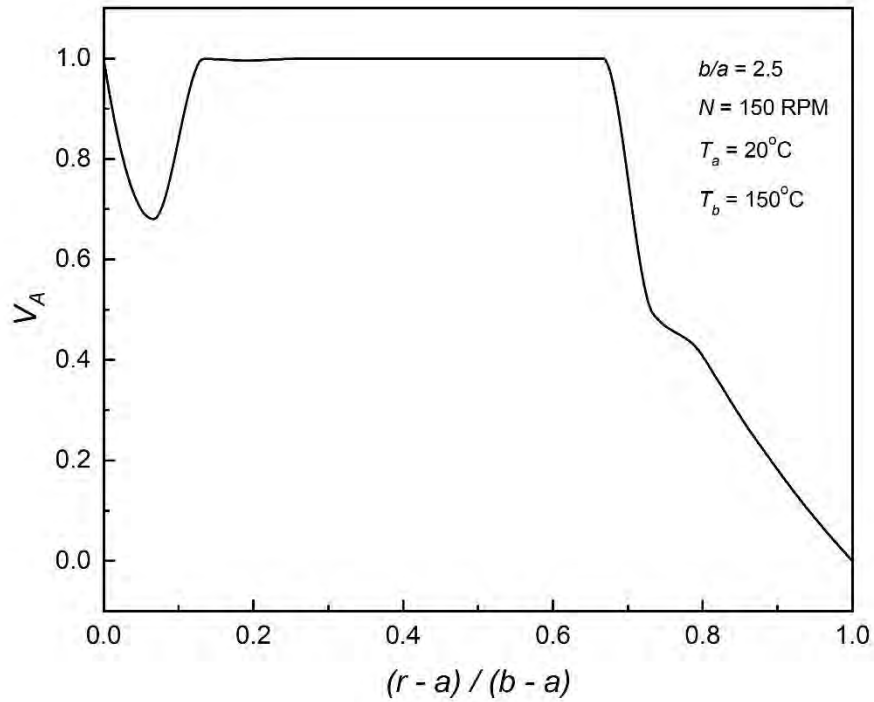


Fig. 5.58: Optimum material distribution in an FGM disk corresponding to the prescribed stress field of **Fig. 5.57**.

The increasing nature is now taken into account when determining the prescribed stress. As displayed in Fig. 5.59, the prescribed stress is assumed to increase from 40 MPa to 70 MPa from the inner to the outer surface of the FGM disk of $b/a = 2.5$. The optimization model calculates ϵ as 0.09 in this case. Therefore, the material distribution may be acceptable, as illustrated in Fig. 5.60. In contrast to the first boundary condition, smoother material distribution is obtained for the second boundary condition.

By designing the FGM disk with the material distribution depicted in Fig. 5.60, it is possible to realize the prescribed stress profile shown in Fig. 5.59.

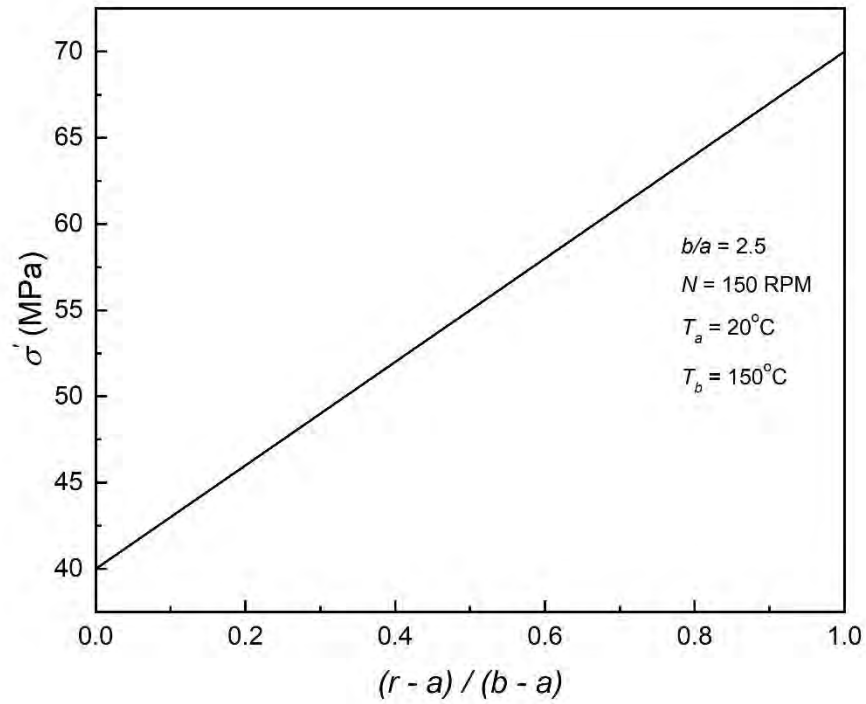


Fig. 5.59: Prescribed stress profile with an increasing nature in an FGM disk corresponds to $b/a = 2.5$ under Boundary Condition II.

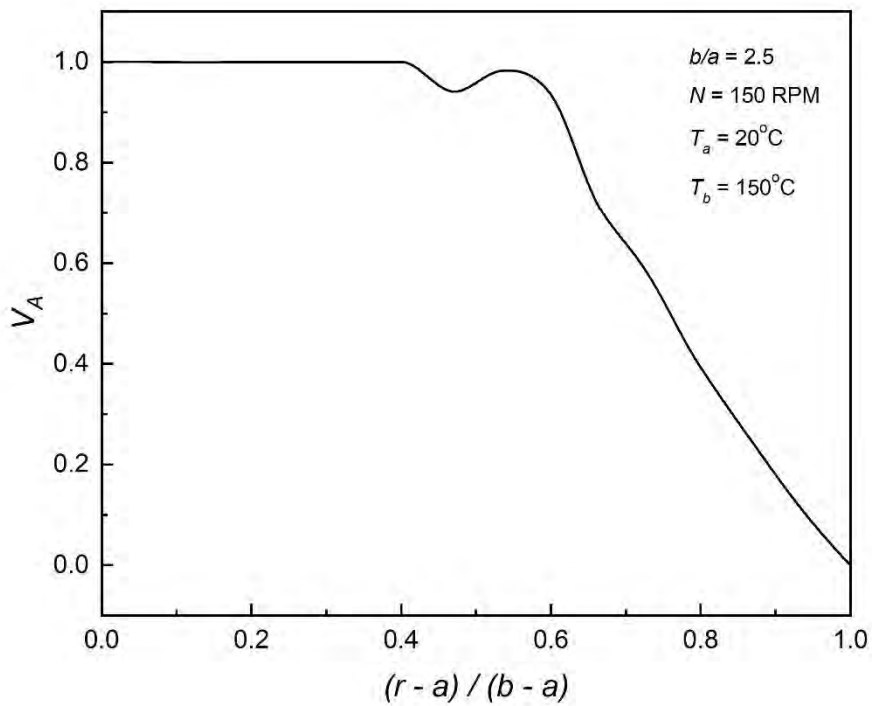


Fig. 5.60: Optimum material distribution in an FGM disk corresponding to the prescribed stress field of **Fig. 5.59**.

Chapter 5: Results and Discussion

Finally, with $b/a = 2.5$, the prescribed stress of 50 MPa is assumed to remain constant from the inner to the outer surface of the FGM disk. The prescribed stress profile for this instance is shown in Fig. 5.61. In this case, $\epsilon = 0.06$, confirming that the material distribution is suitable to adopt, as represented graphically in Fig. 5.62. The optimum material distribution for the second boundary condition, unlike the first, has a negligible decreasing-increasing tendency near the inner surface because of the different boundary condition. Therefore, optimum material distribution corresponding to the similar prescribed von Mises stress profile for the second boundary condition is smoother than that of the first boundary condition.

The prescribed stress profile shown in Fig. 5.61 is predicted by designing the FGM disk having the material distribution illustrated in Fig. 5.62.

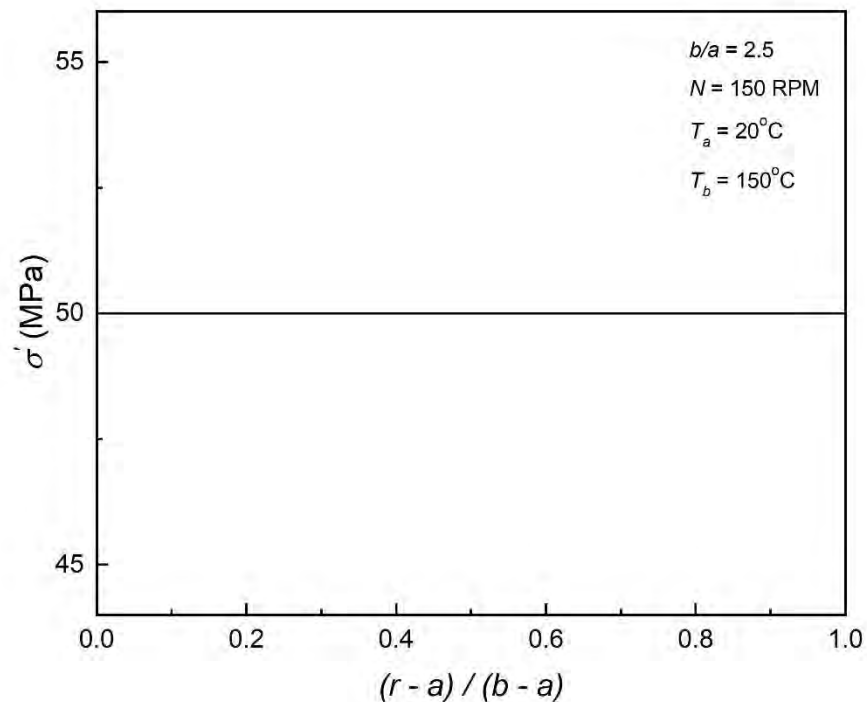


Fig. 5.61: Prescribed stress profile (Constant) in an FGM disk corresponds to $b/a = 2.5$ under Boundary Condition II.

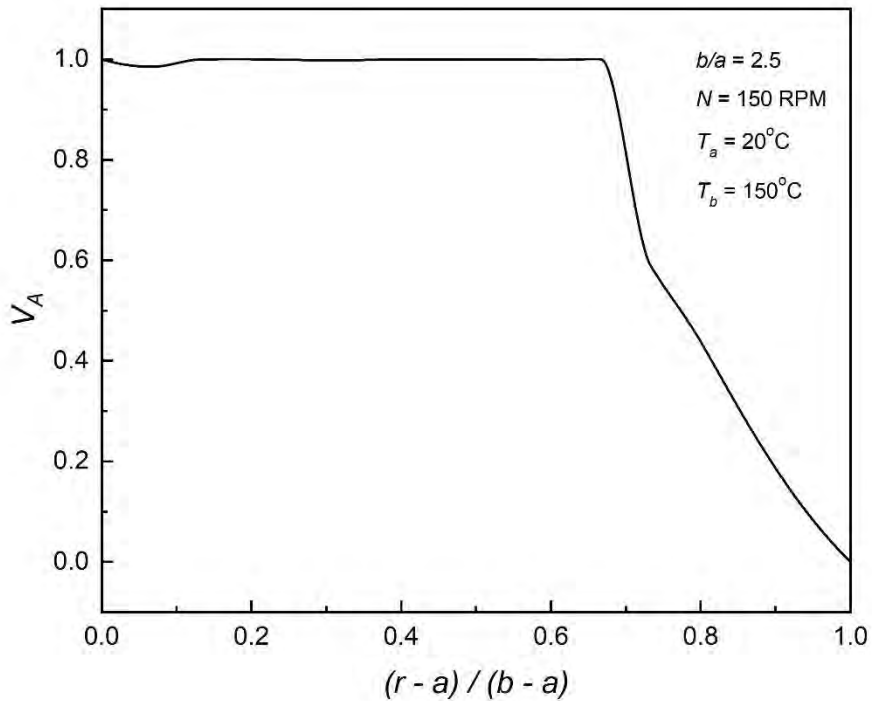


Fig. 5.62: Optimum material distribution in an FGM disk corresponding to the prescribed stress field of **Fig. 5.61**.

The FGM disk, which corresponds to $b/a = 5$, has now been discussed. To begin, the prescribed stress is expected to drop from 70 MPa to 40 MPa from the inner to the outer surface of the FGM disk, corresponding to $b/a = 5$, as shown in Fig. 5.63. The value of ϵ is determined to be 0.06 using the optimization model for the inverse problem, and hence the computed material distribution may predict the prescribed stress. The optimum material distribution is depicted in Fig. 5.64. It is evident from Fig. 5.64 that near the inner surface of the disk, the nature of the optimum material distribution is completely different from the first boundary condition as the second boundary condition is implemented. In addition, the distribution shown in Fig. 5.64 is also totally different from the material distribution profile of Fig. 5.58, even though the same prescribed von Mises stress distribution is realized. The different radial thickness of the disk is responsible for this change.

The prescribed stress profile mentioned in Fig. 5.63 is realized by designing the FGM disk having the material distribution shown in Fig. 5.64.

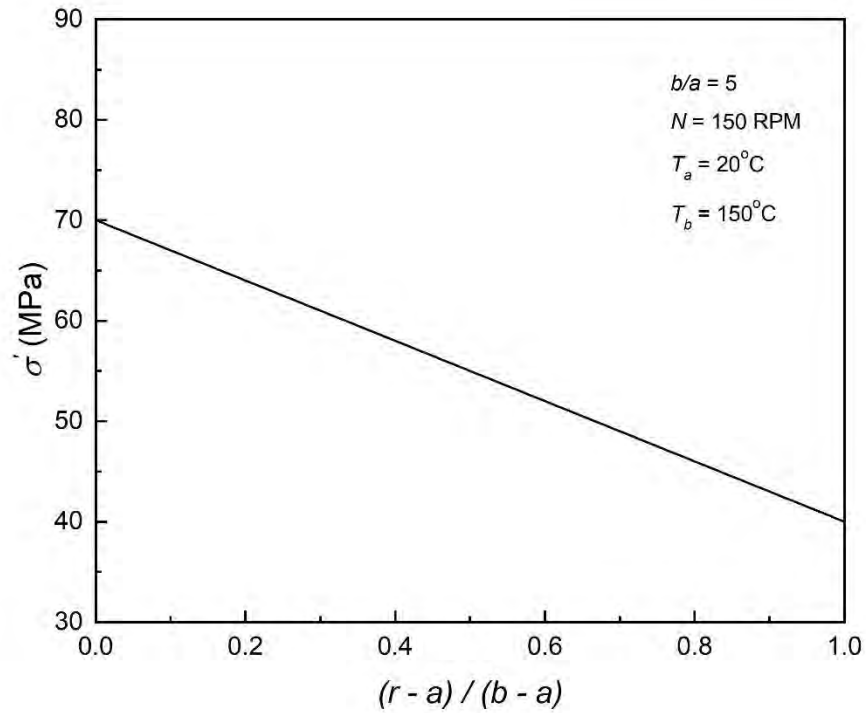


Fig. 5.63: Prescribed stress profile with a decreasing nature in an FGM disk corresponds to $b/a = 5$ under Boundary Condition II.

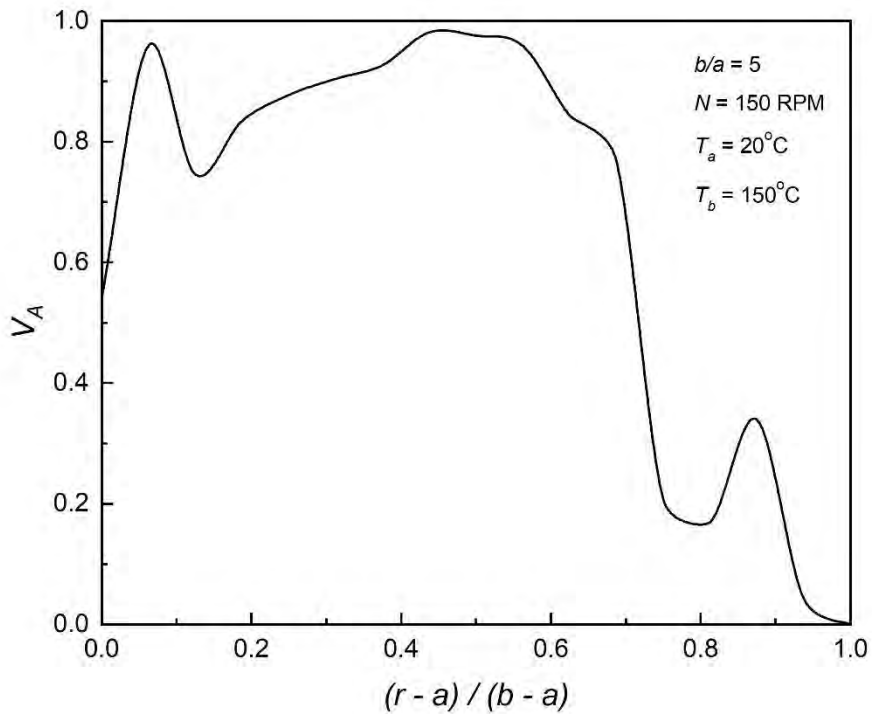


Fig. 5.64: Optimum material distribution in an FGM disk corresponding to the prescribed stress field of **Fig. 5.63**.

Chapter 5: Results and Discussion

Furthermore, as shown in Fig. 5.65, the prescribed stress is projected to rise from 60 MPa to 80 MPa from the inner to the outer surface of the FGM disk, corresponding to $b/a = 5$. Using the optimization model, the value of ϵ is found to be 0.1 in this regard. It is mentioned earlier that the value of ϵ is set to 0.1, and because the material distribution is only meant to be approved if the value of the respective objective function is less than or equal to ϵ , it is apparent that the calculated material distribution for this instance is able to accurately predict the respective prescribed stress. Fig. 5.66 exhibits the corresponding material distribution. In contrast to the first boundary condition, near the inner surface of the disk, the nature of the optimum material distribution is completely different because of the different boundary condition, as shown in Fig. 5.66. Furthermore, the radial thickness of the disk also influences the optimum material distribution significantly.

It is possible to achieve the prescribed stress profile shown in Fig. 5.65 by designing the FGM disk to have the material distribution depicted in Fig. 5.66.

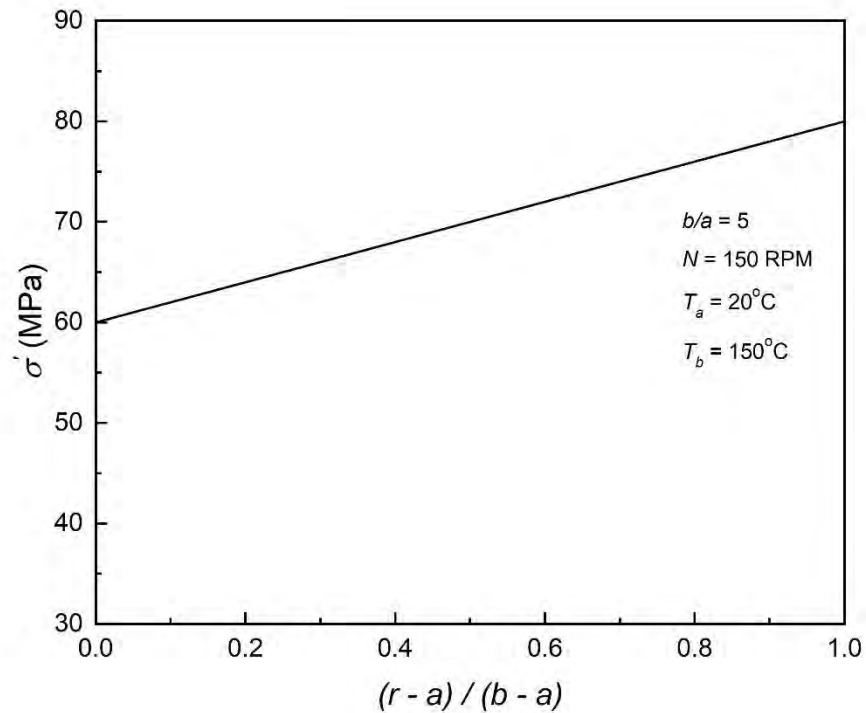


Fig. 5.65: Prescribed stress profile with an increasing nature in an FGM disk corresponds to $b/a = 5$ under Boundary Condition II.

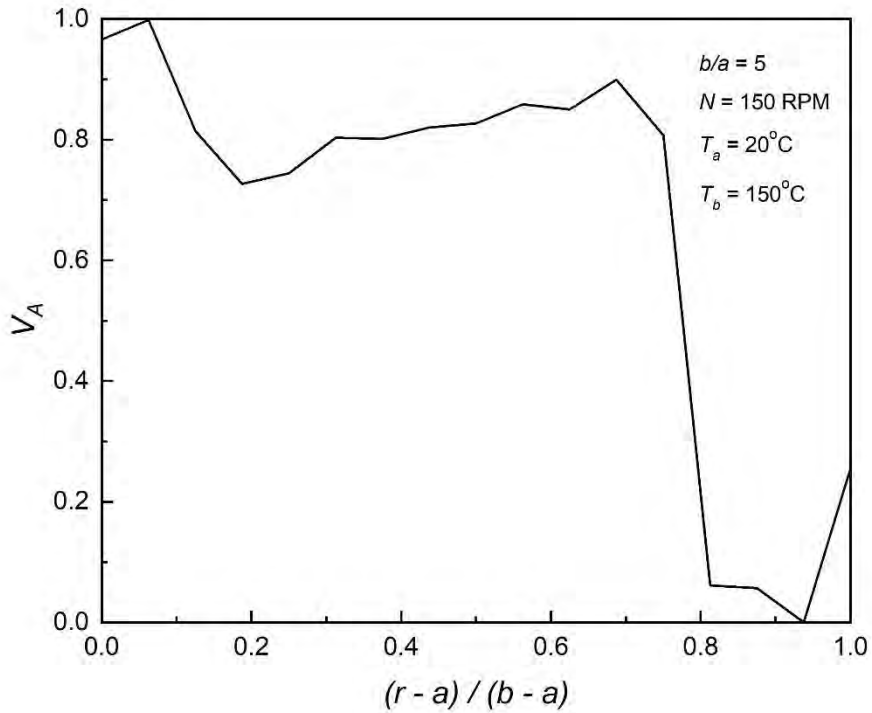


Fig. 5.66: Optimum material distribution in an FGM disk corresponding to the prescribed stress field of **Fig. 5.65**.

Finally, as shown in Fig. 5.67, the specified stress of 70 MPa is assumed to be constant from the inner to the outer surface of the FGM disk, corresponding to $b/a = 5$. Using the inverse problem optimization problem of the current study, ϵ is now calculated as 0.077 for this prescribed stress. As a result, the calculated material distribution may predict the prescribed stress profile within the specified tolerance limit. Fig. 5.68 illustrates the corresponding optimum material distribution.

The prescribed stress profile illustrated in Fig. 5.67 is realized by designing the FGM disk having the material distribution shown in Fig. 5.68.

Section 5.4.2 demonstrates that for the same or similar prescribed stress field, the material distribution is seriously influenced due to the different radial thicknesses of the FGM disk.

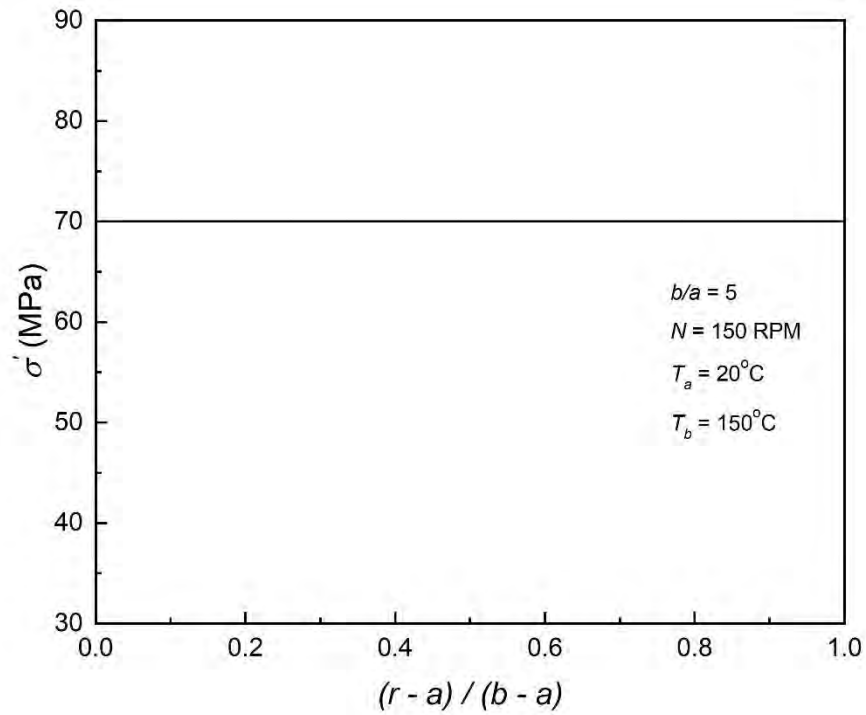


Fig. 5.67: Prescribed stress profile (Constant) in an FGM disk corresponds to $b/a = 5$ under Boundary Condition II.

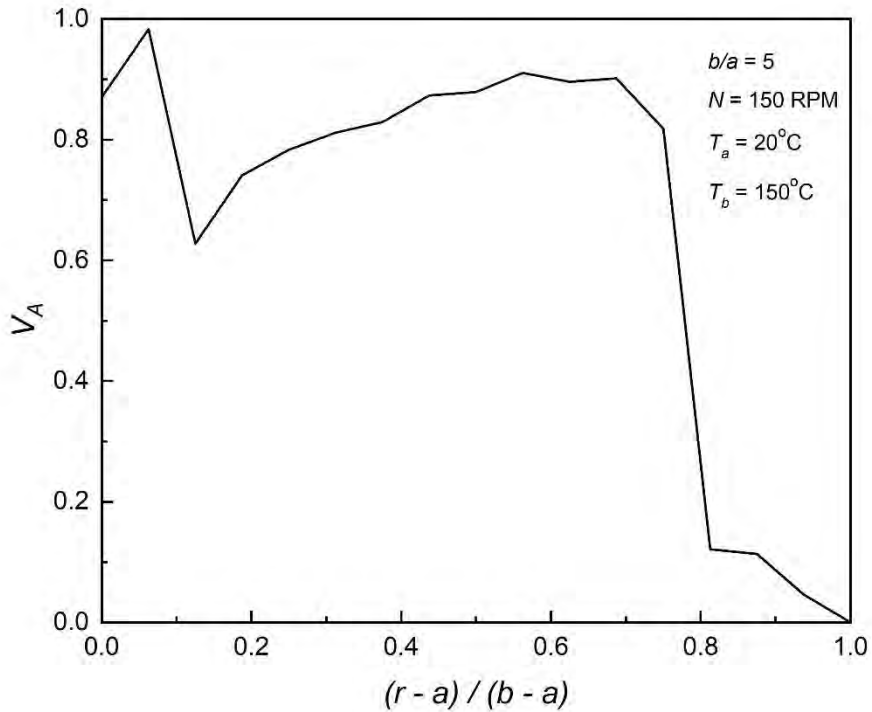


Fig. 5.68: Optimum material distribution in an FGM disk corresponding to the prescribed stress field of Fig. 5.67.

CHAPTER 6

CONCLUSIONS AND RECOMMENDATIONS

6.1 Conclusions

An optimization model is developed to calculate optimum material distribution corresponding to the minimum/prescribed stress profile in a rotating functionally graded material circular disk. To determine stresses for any prescribed material distribution, a mathematical model of direct problem is also developed. The second-order governing differential equation is solved by a standard finite element method in both models. The verification of the models is confirmed by comparing the obtained numerical results with existing works in the literature. Any two materials A and B can be employed in the mathematical models. Numerical results are achieved by demonstrating the models for Al and Al_2O_3 as materials A and B , respectively. The following key points can be noted from the numerical results.

- i. Stress profile, temperature field, angular speed, and radial thickness of the FGM disk all have significant influence on the optimum material distributions
- ii. Stresses developed in an FGM disk is greatly affected by prescribed material distribution and vice versa.
- iii. von Mises stress, radial stress, circumferential stress, and radial displacement all are dependent on the material distribution.

The optimization model can pave the way for evaluating the optimum material distribution in an FGM disk ensuring the minimum stresses in the disk. This can add a new dimension to the process of designing a circular cutter or grinding disk with FGMs having higher efficacy and longevity than the cutters or grinding disks of

Chapter 6: Conclusions and Recommendations

monoclinic materials. In addition, the optimization model of the present work is such a powerful mathematical model that it can accomplish the followings.

- The mathematical model of inverse problem is capable of producing any form of output depending on the objective function. Thus, by setting the appropriate objective function, the optimization model can provide the respective results.
- The model is able to determine the optimum material distribution corresponding to the minimum or prescribed stress field in any FGM disk, which is completely impossible if stresses are determined by considering prescribed material distribution such as exponential function, power function, and sigmoid function, etc.
- Mathematical models of both the inverse and direct problems of the present study can be applied to a rotating functionally graded material (FGM) or a homogeneous circular disk subjected to thermal load.

6.2 Recommendations

Some recommendations for further work are as follows:

- The current investigation has been carried out with the unit thickness of the FGM disk being taken into account. The original shape or geometry of grinding disk cutters may be obtained by taking the thickness of the FGM into consideration. The optimization model of the current study may then be applied for desired output by taking the thickness of the FGM disk into consideration.
- Contact stress is an important factor when designing cutters and grinding disks. Thus, the contact stress may be incorporated into the current mathematical model for further investigation.
- Other sophisticated geometries built of FGM, such as human bone, may be used in this optimization model to provide an output based on biomedical research requirements.

REFERENCES

- [1] Saleh, B., Jiang, J., Ma, A., Song, D., and Yang, D. (2019). Effect of Main Parameters on the Mechanical and Wear Behaviour of Functionally Graded Materials by Centrifugal Casting: A Review. *Metals and Materials International*, 25(6), 1395–1409.
- [2] Fathi, R., Ma, A., Saleh, B., Xu, Q., and Jiang, J. (2020). Investigation on mechanical properties and wear performance of functionally graded AZ91-SiCp composites via centrifugal casting. *Materials Today Communications*, 24, 101169.
- [3] Kassner, M. E., Smith, K. K., and Campbell, C. S. (2015). Low-temperature creep in pure metals and alloys. *Journal of Materials Science*, 50(20), 6539–6551.
- [4] Xu, Q., Ma, A., Li, Y., Saleh, B., Yuan, Y., Jiang, J., and Ni, C. (2019). Enhancement of Mechanical Properties and Rolling Formability in AZ91 Alloy by RD-ECAP Processing. *Materials*, 12(21), 3503.
- [5] Saleh, B., Jiang, J., Xu, Q., Fathi, R., Ma, A., Li, Y., and Wang, L. (2021). Statistical Analysis of Dry Sliding Wear Process Parameters for AZ91 Alloy Processed by RD-ECAP Using Response Surface Methodology. *Metals and Materials International*, 27(8), 2879–2897.
- [6] Xu, Q., Ma, A., Saleh, B., Li, Y., Yuan, Y., Jiang, J., and Ni, C. (2020). Enhancement of strength and ductility of SiCp/AZ91 composites by RD-ECAP processing. *Materials Science and Engineering: A*, 771, 138579.
- [7] El-Galy, I. M., Bassiouny, B. I., and Ahmed, M. H. (2018). Empirical Model for Dry Sliding Wear Behaviour of Centrifugally Cast Functionally Graded Al/SiCp Composite. *Key Engineering Materials*, 786, 276–285.
- [8] Saleh, B., Jiang, J., Ma, A., Song, D., Yang, D., and Xu, Q. (2020). Review on the Influence of Different Reinforcements on the Microstructure and Wear Behavior of Functionally Graded Aluminum Matrix Composites by Centrifugal Casting. *Metals and Materials International*, 26(7), 933–960.

References

- [9] Nohut, S., and Schwentenwein, M. (2022). Vat Photopolymerization Additive Manufacturing of Functionally Graded Materials: A Review. *Journal of Manufacturing and Materials Processing*, 6(1), 17.
- [10] Kawasaki, A., and Watanabe, R. (1997). Concept and P/M fabrication of functionally gradient materials. *Ceramics International*, 23(1), 73–83.
- [11] Mahamood, R., Jen, T. C., Akinlabi, S., Hassan, S., Shatalov, M., Murashkin, E., and Akinlabi, E. T. (2021). Functionally Graded Materials: An Introduction. In *Functionally Graded Materials (FGMs)*. CRC Press.
- [12] Shanmugavel, P., G B, B., Chandrasekaran, Dr. M., Mani, P. S., and Srinivasan, S. P. (2012). An overview of fracture analysis in Functionally Graded Materials. *European Journal of Scientific Research*, 68, 412–439.
- [13] Atai, A. A., Nikranjbar, A., and Kasiri, R. (2012). Buckling and post-buckling behaviour of semicircular functionally graded material arches: A theoretical study. *Proceedings of the Institution of Mechanical Engineers, Part C: Journal of Mechanical Engineering Science*, 226(3), 607–614.
- [14] Koizumi, M., and Niino, M. (1995). Overview of FGM Research in Japan. *MRS Bulletin*, 20(1), 19–21.
- [15] NIINO, M. (1987). Functionally gradient materials as thermal barrier for space plane. *J. Jpn. Composite Mater.*, 13, 257–264.
- [16] Conde, F. M., Coelho, P. G., and Guedes, J. M. (2022). Multi-material and strength-oriented microstructural topology optimization applied to discrete phase and functionally graded materials. *Structural and Multidisciplinary Optimization*, 65(4), 127.
- [17] Zhang, B., Jaiswal, P., Rai, R., and Nelaturi, S. (2018). Additive Manufacturing of Functionally Graded Material Objects: A Review. *Journal of Computing and Information Science in Engineering*, 18(4).
- [18] Chen, Y., and Liou, F. (2018). Additive Manufacturing of Metal Functionally Graded Materials: A Review. *Proceedings of the 29th Annual International Solid Freeform Fabrication Symposium (2018, Austin, TX)*, 1215–1231.

References

- [19] Panchal, Y., and K, P. (2022). Functionally graded materials: A review of computational materials science algorithms, production techniques, and their biomedical applications. *Proceedings of the Institution of Mechanical Engineers, Part C: Journal of Mechanical Engineering Science*, 09544062221109261.
- [20] Mortensen, A., and Suresh, S. (1995). Functionally graded metals and metal-ceramic composites: Part 1 Processing. *International Materials Reviews*, 40(6), 239–265.
- [21] Miyamoto, Y., Kaysser, W. A., Rabin, B. H., Kawasaki, A., and Ford, R. G. (1999). Introduction. In Y. Miyamoto, W. A. Kaysser, B. H. Rabin, A. Kawasaki, and R. G. Ford (Eds.), *Functionally Graded Materials: Design, Processing and Applications* (pp. 1–6). Springer US.
- [22] Pasha, A., and B.m, R. (2022). Functionally graded materials (FGM) fabrication and its potential challenges and applications. *Materials Today: Proceedings*, 52, 413–418.
- [23] Wang, S. S. (1983). Fracture Mechanics for Delamination Problems in Composite Materials. *Journal of Composite Materials*, 17(3), 210–223.
- [24] Mahamood, R. M., and Akinlabi, E. T. (2017). Types of Functionally Graded Materials and Their Areas of Application. In R. M. Mahamood and E. T. Akinlabi (Eds.), *Functionally Graded Materials* (pp. 9–21). Springer International Publishing.
- [25] Mahamood, R. M., and Akinlabi, E. T. (2015). Laser metal deposition of functionally graded Ti6Al4V/TiC. *Materials and Design, Complete*(84), 402–410.
- [26] Dubey, A., Jaiswal, S., and Lahiri, D. (2022). Promises of Functionally Graded Material in Bone Regeneration: Current Trends, Properties, and Challenges. *ACS Biomaterials Science and Engineering*, 8(3), 1001–1027.
- [27] LU, L., Chekroun, M., Abraham, O., Maupin, V., and Villain, G. (2011). Mechanical properties estimation of functionally graded materials using surface waves recorded with a laser interferometer. *NDT and E International*, 44(2), 169–177.

References

- [28] El-Galy, I. M., Saleh, B. I., and Ahmed, M. H. (2019). Functionally graded materials classifications and development trends from industrial point of view. *SN Applied Sciences*, 1(11), 1378.
- [29] Saleh, B., Jiang, J., Fathi, R., Al-hababi, T., Xu, Q., Wang, L., Song, D., and Ma, A. (2020). 30 Years of functionally graded materials: An overview of manufacturing methods, Applications and Future Challenges. *Composites Part B: Engineering*, 201, 108376.
- [30] Lutz, E. H. (1994). Microstructure and Properties of Plasma Ceramics. *Journal of the American Ceramic Society*, 77(5), 1274–1280.
- [31] Sampath, S., Herman, H., Shimoda, N., and Saito, T. (1995). Thermal Spray Processing of FGMs. *MRS Bulletin*, 20(1), 27–31.
- [32] Miyamoto, Y., Kaysser, W. A., Rabin, B. H., Kawasaki, A., and Ford, R. G. (1999). Processing and Fabrication. In Y. Miyamoto, W. A. Kaysser, B. H. Rabin, A. Kawasaki, and R. G. Ford (Eds.), *Functionally Graded Materials: Design, Processing and Applications* (pp. 161–245). Springer US.
- [33] Li, W., Karnati, S., Zhang, Y., and Liou, F. (2018). Investigating and eliminating powder separation in pre-mixed powder supply for laser metal deposition process. *Journal of Materials Processing Technology*, 254, 294–301.
- [34] Liu, Y., Liu, C., Liu, W., Ma, Y., Zhang, C., Cai, Q., and Liu, B. (2018). Microstructure and properties of Ti/Al lightweight graded material by direct laser deposition. *Materials Science and Technology*, 34(8), 945–951.
- [35] Tyagi, S. A., and Manjaiah, M. (2022). Laser Additive Manufacturing of Titanium-Based Functionally Graded Materials: A Review. *Journal of Materials Engineering and Performance*.
- [36] Gasik, M., Kawasaki, A., and Ueda, S. (2000). Design and Powder Metallurgy Processing of Functionally Graded Materials. In *Materials Development and Processing—Bulk Amorphous Materials, Undercooling and Powder Metallurgy* (pp. 258–264). John Wiley and Sons, Ltd.
- [37] Kırmızı, G., Arık, H., and Çinici, H. (2019). Experimental study on mechanical and ballistic behaviours of silicon carbide reinforced functionally graded aluminum foam composites. *Composites Part B: Engineering*, 164, 345–357.

References

- [38] Strojny-Nędza, A., Pietrzak, K., and Węglewski, W. (2016). The Influence of Al₂O₃ Powder Morphology on the Properties of Cu-Al₂O₃ Composites Designed for Functionally Graded Materials (FGM). *Journal of Materials Engineering and Performance*, 25(8), 3173–3184.
- [39] Watanabe, Y., Sato, H., and Miura-Fujiwara, E. (2015). Functionally Graded Metallic Biomaterials. In M. Niinomi, T. Narushima, and M. Nakai (Eds.), *Advances in Metallic Biomaterials: Processing and Applications* (pp. 181–209). Springer.
- [40] Chakraborty, A., Gopalakrishnan, S., and Reddy, J. N. (2003). A new beam finite element for the analysis of functionally graded materials. *International Journal of Mechanical Sciences*, 45(3), 519–539.
- [41] Kiani, Y., Taheri, S., and Eslami, M. R. (2011). Thermal Buckling of Piezoelectric Functionally Graded Material Beams. *Journal of Thermal Stresses*, 34(8), 835–850.
- [42] Ben-Oumrane, S., Abedlouahed, T., Ismail, M., Mohamed, B. B., Mustapha, M., and El Abbas, A. B. (2009). A theoretical analysis of flexional bending of Al/Al₂O₃ S-FGM thick beams. *Computational Materials Science*, 44(4), 1344–1350.
- [43] Şimşek, M. (2016). Buckling of Timoshenko beams composed of two-dimensional functionally graded material (2D-FGM) having different boundary conditions. *Composite Structures*, 149, 304–314.
- [44] Kiani, Y., and Eslami, M. R. (2010). Thermal buckling analysis of functionally graded material beams. *International Journal of Mechanics and Materials in Design*, 6(3), 229–238.
- [45] Jabbari, M., Sohrabpour, S., and Eslami, M. R. (2002). Mechanical and thermal stresses in a functionally graded hollow cylinder due to radially symmetric loads. *International Journal of Pressure Vessels and Piping*, 79(7), 493–497.
- [46] Jabbari, M., Bahtui, A., and Eslami, M. R. (2006). Axisymmetric Mechanical and Thermal Stresses in Thick Long FGM Cylinders. *Journal of Thermal Stresses*, 29(7), 643–663.

References

- [47] Jabbari, M., Bahtui, A., and Eslami, M. R. (2009). Axisymmetric mechanical and thermal stresses in thick short length FGM cylinders. *International Journal of Pressure Vessels and Piping*, 86(5), 296–306.
- [48] Shao, Z. S. (2005). Mechanical and thermal stresses of a functionally graded circular hollow cylinder with finite length. *International Journal of Pressure Vessels and Piping*, 82(3), 155–163.
- [49] Abbas, I. A. (2014). Nonlinear transient thermal stress analysis of thick-walled FGM cylinder with temperature-dependent material properties. *Meccanica*, 49(7), 1697–1708.
- [50] Awaji, H., and Sivakumar, R. (2001). Temperature and Stress Distributions in a Hollow Cylinder of Functionally Graded Material: The Case of Temperature-Independent Material Properties. *Journal of the American Ceramic Society*, 84(5), 1059–1065.
- [51] Bayat, M., Saleem, M., Sahari, B. B., Hamouda, A. M. S., and Mahdi, E. (2008). Analysis of functionally graded rotating disks with variable thickness. *Mechanics Research Communications*, 35(5), 283–309.
- [52] Durodola, J. F., and Attia, O. (2000). Deformation and stresses in functionally graded rotating disks. *Composites Science and Technology*, 60(7), 987–995.
- [53] Zenkour, A. M. (2009). Stress distribution in rotating composite structures of functionally graded solid disks. *Journal of Materials Processing Technology*, 209(7), 3511–3517.
- [54] Nikbakht, S., Kamarian, S., and Shakeri, M. (2019). A review on optimization of composite structures Part II: Functionally graded materials. *Composite Structures*, 214, 83–102.
- [55] Reddy, J. N., and Chin, C. D. (1998). Thermomechanical Analysis of Functionally Graded Cylinders and Plates. *Journal of Thermal Stresses*, 21(6), 593–626.
- [56] Chi, S.-H., and Chung, Y.-L. (2006). Mechanical behavior of functionally graded material plates under transverse load—Part I: Analysis. *International Journal of Solids and Structures*, 43(13), 3657–3674.

References

- [57] Chi, S.-H., and Chung, Y.-L. (2006). Mechanical behavior of functionally graded material plates under transverse load—Part II: Numerical results. *International Journal of Solids and Structures*, 43(13), 3675–3691.
- [58] Tutuncu, N. (2007). Stresses in thick-walled FGM cylinders with exponentially-varying properties. *Engineering Structures*, 29(9), 2032–2035.
- [59] Shao, Z. S., and Ma, G. W. (2008). Thermo-mechanical stresses in functionally graded circular hollow cylinder with linearly increasing boundary temperature. *Composite Structures*, 83(3), 259–265.
- [60] Woo, J., and Meguid, S. A. (2001). Nonlinear analysis of functionally graded plates and shallow shells. *International Journal of Solids and Structures*, 38(42), 7409–7421.
- [61] Bagherizadeh, E., Kiani, Y., and Eslami, M. R. (2011). Mechanical buckling of functionally graded material cylindrical shells surrounded by Pasternak elastic foundation. *Composite Structures*, 93(11), 3063–3071.
- [62] Arshad, S. H., Naeem, M. N., and Sultana, N. (2007). Frequency analysis of functionally graded material cylindrical shells with various volume fraction laws. *Proceedings of the Institution of Mechanical Engineers, Part C: Journal of Mechanical Engineering Science*, 221(12), 1483–1495.
- [63] Dai, J., Liu, Y., Liu, H., Miao, C., and Tong, G. (2019). A parametric study on thermo-mechanical vibration of axially functionally graded material pipe conveying fluid. *International Journal of Mechanics and Materials in Design*, 15(4), 715–726.
- [64] Deng, J., Liu, Y., Zhang, Z., and Liu, W. (2017). Dynamic behaviors of multi-span viscoelastic functionally graded material pipe conveying fluid. *Proceedings of the Institution of Mechanical Engineers, Part C: Journal of Mechanical Engineering Science*, 231(17), 3181–3192.
- [65] Deng, J., Liu, Y., Zhang, Z., and Liu, W. (2017). Stability analysis of multi-span viscoelastic functionally graded material pipes conveying fluid using a hybrid method. *European Journal of Mechanics - A/Solids*, 65, 257–270.
- [66] Kordkheili, S. A. H., and Naghdabadi, R. (2007). Thermoelastic analysis of a functionally graded rotating disk. *Composite Structures*, 79(4), 508–516.

References

- [67] Hosseini, M., Shishesaz, M., Tahan, K. N., and Hadi, A. (2016). Stress analysis of rotating nano-disks of variable thickness made of functionally graded materials. *International Journal of Engineering Science*, 109, 29–53.
- [68] Tutuncu, N., and Temel, B. (2009). A novel approach to stress analysis of pressurized FGM cylinders, disks and spheres. *Composite Structures*, 91(3), 385–390.
- [69] Timoshenko, S. P., and Goodier, J. N. (1970). *Theory of Elasticity* (Third Edition). McGraw Hill.
- [70] Sadd, M. H. (2021). Chapter 12—Thermoelasticity. In M. H. Sadd (Ed.), *Elasticity (Fourth Edition)* (pp. 379–405). Academic Press.
- [71] Madan, R., Bhowmick, S., and Nath Saha, K. (2018). Stress and deformation of functionally graded rotating disk based on modified rule of mixture. *Materials Today: Proceedings*, 5(9, Part 3), 17778–17785.
- [72] Afsar, A. M., and Go, J. (2010). Finite element analysis of thermoelastic field in a rotating FGM circular disk. *Applied Mathematical Modelling*, 34(11), 3309–3320.
- [73] Arnab, B., Islam, S. M. R., Khalak, A. A., and Afsar, A. M. (2014). Finite Difference Solution to Thermoelastic Field in a Thin Circular FGM Disk with a Concentric Hole. *Procedia Engineering*, 90, 193–198.
- [74] Go, J., Afsar, A. M., and Song, J. I. (2010). Analysis of Thermoelastic Characteristics of a Rotating FGM Circular Disk by Finite Element Method. *Advanced Composite Materials*, 19(2), 197–213.
- [75] Afsar, A. M., Go, J., and Song, J. I. (2010). A Mathematical Analysis of Thermoelastic Characteristics of a Rotating Circular Disk with an FGM Coating at the Outer Surface. *Advanced Composite Materials*, 19(3), 269–288.
- [76] Zharfi, H., and Toussi, H. E. (2017). Numerical creep analysis of FGM rotating disc with GDQ method. *Journal of Theoretical and Applied Mechanics*, 55(1), 331–341.
- [77] Sharma, D., and Kaur, R. (2019). Finite element solution for stress and strain in FGM circular disk. *AIP Conference Proceedings*, 2142(1), 110024.

References

- [78] Dai, T., and Dai, H.-L. (2015). Investigation of mechanical behavior for a rotating FGM circular disk with a variable angular speed. *Journal of Mechanical Science and Technology*, 29(9), 3779–3787.
- [79] Yildirim, V. (2019). Thermomechanical Characteristics of a Functionally Graded Mounted Uniform Disc with/without Rigid Casing. *Journal of Aerospace Technology and Management*, 11.
- [80] Go, J. (2021). Thermoelastic Characteristics of Functionally Graded Circular Disk Models under the Loading of Contact Forces. *Mathematical Problems in Engineering*, 2021, e8845028.
- [81] Madan, R., Saha, K., and Bhowmick, S. (2020). Limit speeds and stresses in power law functionally graded rotating disks. *Advances in Materials Research*, 9(2), 115–131.
- [82] Madan, R., Bhowmick, S., and Saha, K. (2019). Limit angular speed of L-FGM rotating disk for both temperature dependent and temperature independent mechanical properties. *Materials Today: Proceedings*, 18, 2366–2373.
- [83] Bakhshi, M., Bagri, A., and Eslami, M. R. (2006). Coupled Thermoelasticity of Functionally Graded Disk. *Mechanics of Advanced Materials and Structures*, 13(3), 219–225.
- [84] Damircheli, M., and Azadi, M. (2011). Temperature and thickness effects on thermal and mechanical stresses of rotating FG-disks. *Journal of Mechanical Science and Technology*, 25(3), 827.
- [85] Madan, R., and Bhowmick, S. (2021). A numerical solution to thermo-mechanical behavior of temperature dependent rotating functionally graded annulus disks. *Aircraft Engineering and Aerospace Technology*, 93(4), 733–744.
- [86] Madan, R., and Bhowmick, S. (2022). Material modelling and limit angular speed analysis of porous trigonometric functionally graded rotating disk. *Advances in Materials and Processing Technologies*, 0(0), 1–13.
- [87] Tutuncu, N., and Temel, B. (2013). An Efficient Unified Method for Thermoelastic Analysis of Functionally Graded Rotating Disks of Variable Thickness. *Mechanics of Advanced Materials and Structures*, 20(1), 38–46.

References

- [88] Rezaei Farimani, M., and Mohadeszadeh, M. (2017). Thermo-elastic bending analysis of FGM rotating plate with axial grading and modified rule of mixture. *Journal of the Brazilian Society of Mechanical Sciences and Engineering*, 39(1), 299–307.
- [89] Moleiro, F., Madeira, J. F. A., Carrera, E., and Reddy, J. N. (2020). Design optimization of functionally graded plates under thermo-mechanical loadings to minimize stress, deformation and mass. *Composite Structures*, 245, 112360.
- [90] Farimani, M. R., and Toussi, H. E. (2013). Plastic limit speed of FGM disc due to the variation of temperature and material composition. *Journal of Reinforced Plastics and Composites*, 32(17), 1257–1267.
- [91] Cho, J. R., and Ha, D. Y. (2002). Volume fraction optimization for minimizing thermal stress in Ni–Al₂O₃ functionally graded materials. *Materials Science and Engineering: A*, 334(1), 147–155.
- [92] Ootao, Y., Tanigawa, Y., and Nakamura, T. (1999). Optimization of material composition of FGM hollow circular cylinder under thermal loading: A neural network approach. *Composites Part B: Engineering*, 30(4), 415–422.
- [93] Khatir, S., Tiachacht, S., Le Thanh, C., Ghandourah, E., Mirjalili, S., and Abdel Wahab, M. (2021). An improved Artificial Neural Network using Arithmetic Optimization Algorithm for damage assessment in FGM composite plates. *Composite Structures*, 273, 114287.
- [94] Yasinsky, A., and Tokova, L. (2017). Inverse problem on the identification of temperature and thermal stresses in an FGM hollow cylinder by the surface displacements. *Journal of Thermal Stresses*.
- [95] Cárdenas-García, J. F., Shabana, Y. M., and Medina, R. A. (2006). Thermal Loading and Material Property Characterization of a Functionally Graded Plate With a Hole Using an Inverse Problem Methodology. *Journal of Thermal Stresses*, 29(1), 1–20.
- [96] Liu, G. R., Han, X., and Lam, K. Y. (2001). Material Characterization of FGM Plates Using Elastic Waves and an Inverse Procedure. *Journal of Composite Materials*, 35(11), 954–971.

References

- [97] Afsar, A. M., and Sekine, H. (2002). Inverse problems of material distributions for prescribed apparent fracture toughness in FGM coatings around a circular hole in infinite elastic media. *Composites Science and Technology*, 62(7), 1063–1077.
- [98] Afsar, A. M., and Sekine, H. (2001). Optimum material distributions for prescribed apparent fracture toughness in thick-walled FGM circular pipes. *International Journal of Pressure Vessels and Piping*, 78(7), 471–484.
- [99] Afsar, A. M., Anisuzzaman, M., and Song, J. I. (2009). Inverse problem of material distribution for desired fracture characteristics in a thick-walled functionally graded material cylinder with two diametrically-opposed edge cracks. *Engineering Fracture Mechanics*, 76(7), 845–855.
- [100] Wakashima, K., and Tsukamoto, H. (1992). An Unified Micromechanical Approach toward Thermomechanical Tailoring of Metal Matrix Composites. *ISIJ International*, 32(8), 883–892.
- [101] C.w, N., R.z, Y., and L.m, Z. (1993). *The Physics Of Metal/Ceramic Functionally Gradient Materials*, *Ceramic Transactions*. 34(0), 75–82.
- [102] Reuss, A. (1929). Berechnung der Fließgrenze von Mischkristallen auf Grund der Plastizitätsbedingung für Einkristalle . *ZAMM - Journal of Applied Mathematics and Mechanics / Zeitschrift Für Angewandte Mathematik Und Mechanik*, 9(1), 49–58.
- [103] Zhang, X. D., Liu, T. Q., and Ge, C. C. (1997). Mathematical Model for Axial-Symmetrical FGM. In I. Shiota and Y. Miyamoto (Eds.), *Functionally Graded Materials 1996* (pp. 35–40). Elsevier Science B.V.
- [104] Mura, T. (1987). General theory of eigenstrains. In T. Mura (Ed.), *Micromechanics of defects in solids* (pp. 1–73). Springer Netherlands.
- [105] Sadd, M. H. (2009). Chapter 4—Material Behavior—Linear Elastic Solids. In M. H. Sadd (Ed.), *Elasticity (Second Edition)* (pp. 77–90). Academic Press.
- [106] Sadd, M. H. (2009). Chapter 7—Two-Dimensional Formulation. In M. H. Sadd (Ed.), *Elasticity (Second Edition)* (pp. 135–150). Academic Press.
- [107] Sadd, M. H. (2009). Chapter 3—Stress and Equilibrium. In M. H. Sadd (Ed.), *Elasticity (Second Edition)* (pp. 55–76). Academic Press.

References

- [108] Wang, Y.-Z., Li, G.-Q., Wang, Y.-B., and Lyu, Y.-F. (2021). Simplified method to identify full von Mises stress-strain curve of structural metals. *Journal of Constructional Steel Research*, 181, 106624.
- [109] Storn, R., and Price, K. (1997). Differential Evolution – A Simple and Efficient Heuristic for global Optimization over Continuous Spaces. *Journal of Global Optimization*, 11(4), 341–359.
- [110] Georgioudakis, M., and Plevris, V. (2020). A Comparative Study of Differential Evolution Variants in Constrained Structural Optimization. *Frontiers in Built Environment*, 6.
- [111] Price, K. V., Storn, R. M., and Lampinen, J. A. (Eds.). (2005). The Differential Evolution Algorithm. In *Differential Evolution: A Practical Approach to Global Optimization* (pp. 37–134). Springer.